Improvement of the lifetime of electric energy storage systems by optimizing the connected modular power converters

Robert Alfie Peña

THESE de DOCTORAT DE
L'UNIVERSITE CLAUDE BERNARD LYON 1

Ecole Doctorale N° 160
Electronique, Electrotechnique, Automatique (EEA)

Discipline :
Génie électrique

Soutenue publiquement le 22/09/2022, par :
Robert Alfie S. PEÑA

Amélioration de la durée de vie des systèmes de stockage d'énergie électrique par optimisation des convertisseurs d'énergie modulaires associés

Devant le jury composé de :

Delphine RIU	Professeure des Universités, Grenoble INP	Présidente
Alain BOUSCAYROL	Professeur des Universités, Université de Lille	Rapporteur
Christophe FORGEZ	Professeur des Universités, Université de Technologie de Compiègne	Rapporteur
Corinne ALONSO	Professeure des Universités, Université Toulouse III – Paul Sabatier	Examinatrice
Ali SARI	Professeur des Universités, Université Claude Bernard Lyon 1	Examinateur
Seïma SHILI	Ingénieure de Concept, SBM Offshore	Examinatrice
Pascal VENET	Professeur des Universités, Université Claude Bernard Lyon 1	Directeur de thèse
Alaa HIJAZI	Maître de Conférences, INSA Lyon	Co-directeur de thèse
Rochdi TRIGUI	Directeur de Recherche, Université Gustave Eiffel	Invité

Résumé

L'hétérogénéité des caractéristiques « constructeur » des dispositifs de stockage d'énergie tels que les supercondensateurs et leurs conditions environnementales affectent leurs performances et entraînent un vieillissement déséquilibré. Les circuits d'équilibrage conventionnels reposent sur l'équilibrage des tensions ou des états de charge (SoC) des cellules. Dans ce travail, nous proposons plutôt d'équilibrer les états de santé (SoH) des cellules pour optimiser la durée de vie du système de stockage d'énergie électrique. Des convertisseurs statiques d'énergie modulaires sont utilisés pour interfacer les supercondensateurs avec le système de charge/décharge et sont commandés de façon à ce que les vieillissements des supercondensateurs soient homogènes. Cela est rendu possible par une méthode d'allocation de commande qui utilise une matrice de pondération basée sur la durée de vie utile restante des supercondensateurs comme indicateur d'état de santé. Pour deux applications, nous avons simulé des équipements complets par utilisation de modèles électrothermiques de supercondensateurs et de modèles des convertisseurs modulaires contrôlés par un module d'allocation de commande. Les simulations ont été validées par des essais expérimentaux. Il est montré que l'utilisation de convertisseurs modulaires associés à une méthode d'allocation de commande optimisant l'état de santé des supercondensateurs prolonge grandement leur durée de vie par rapport à l'utilisation d'un simple convertisseur d'énergie avec circuit d'équilibrage classique.

Abstract

Initial conditions and characteristics affect the operational performance of energy storage devices such as supercapacitors resulting in unbalanced aging. Conventional systems rely on balancing voltages or states of charge (SoC). In this work however, states of health (SoH) are used instead. Modular power converters are employed to interface supercapacitors and are controlled to age them at the same rate. It was made possible by a control allocation method that uses a weighting matrix based on the remaining useful life of supercapacitors as a health or reliability indicator. We modeled and simulated complete systems for two applications composed of the multiphysical model of supercapacitors, the power converters, the control systems, and the control allocation module. Simulation and experimental comparisons with the classical balancing approach show that the modular converter approach optimizes system lifetime and significantly extends it.

Acknowledgments

This work would not have been possible if not for the funding from the CHED-PhilFrance Scholarship, which was jointly provided by the Philippine and French governments through the Commission on Higher Education (CHED) and the Embassy of France to the Philippines. I will forever be thankful for the administrative and organizational support extended to me for my studies in Lyon by CHED's Scholarship for Graduate Studies Abroad and International Relations Team under the K to 12 Transition Program and by Campus France, both in Manila and in Lyon.

My deepest appreciation goes to my supervisor, Prof. Pascal Venet, and my co-supervisor, Dr. Alaa Hijazi. They are excellent role models who helped me steer the direction of this thesis and dig deep into the research work required for my topic. I can only imagine their difficulty in having an international student whose command of the French language is not up to par, but they were very patient. They went out of their way to support my work and were always understanding of my shortcomings. I will forever be grateful to them for bringing me to the finish line. I can only hope to become the excellent researchers that they are.

Aside from the Ampère Laboratory, I also benefited from collaboration with SuperGrid Institute, to which I owe the completion of the necessary experimental work for my topic. My gratitude goes to Dr. Florent Morel, who provided administrative and research support to my stint at the institute. In particular, I sincerely thank Dr. Florian Errigo for collaborating and working with me on a number of subjects related to my topic.

The members of the jury deserve my sincere thanks: Prof. Delphine Riu, who was president, Profs. Alain Bouscayrol, Christophe Forgez, Corinne Alonso, Ali Sari, and Drs. Seïma Shili and Rochdi Trigui. Though tough, I learned much from their questions and examination during the thesis defense. My exchange with them challenged me to explore other related topics and areas I could work on in the future. Let me also take this opportunity to especially thank the reviewers Profs. Bouscayrol and Forgez for their comprehensive review of this thesis, which I found enlightening.

Lastly, I would like to take this opportunity to thank everyone who helped me on this challenging journey: the research, technical, and administrative staff at both the Ampère Laboratory and SuperGrid Institute, members of my thesis monitoring committee, my home department and school back in Ateneo, colleagues, mentors, friends in Lyon and back home in the Philippines, and most especially, my family and loved ones. I would not have reached this point if not for you: *j'aimerais vous exprimer mes remerciements les plus sincères*.

Table of Contents

List of Figures

List of Tables

Nomenclature

List of Symbols

$\mathbf{A}$	System matrix of the state-space averaged model of the nonisolated bidirectional DC-DC converter or of the modular power converter
$\mathbf{B}, \mathbf{B}_u$	Input or control matrix of the state-space averaged model of the nonisolated bidirectional DC-DC converter or of the modular power converter
$\mathbf{C}$	Output matrix of the state-space averaged model of the nonisolated bidirectional DC-DC converter or of the modular power converter
C_{ave}	Average of supercapacitor (group) capacitances
C_C, C	Capacitance of the capacitor of the nonisolated bidirectional DC-DC converter or of the modular power converter
$C_{C,\text{orig}}$	Original capacitance sizing of the capacitor of the nonisolated bidirectional DC-DC converter
C_{dch}	Measured capacitance of the capacitor component of the supercapacitor *RC* model during the discharge phase
$C_{k,j}$	Capacitance of the *j*th supercapacitor (group) at the time step *k*
C_{max}	Maximum supercapacitor (group) capacitance
C_{min}	Minimum supercapacitor (group) capacitance
C_{sc}	Capacitance of the capacitor component of the supercapacitor *RC* model
$C_{\text{sc},0,j}$	Initial capacitance of the *j*th supercapacitor (group)
$C_{\text{sc,meas}}$	Measured capacitance of the capacitor component of the supercapacitor *RC* model
C_{sm}	Capacitance of the modular multilevel converter submodule capacitor
C_{th}	Supercapacitor thermal capacity in the supercapacitor thermal behavior circuit model
d_{ac}	Small AC signal perturbation about the DC value of the modular power converter duty ratio
D_{buck}	Duty ratio of the buck mode of the modular power converter
D_j	Duty ratio of the *j*th modular power converter
E	Energy stored in the capacitor component of the supercapacitor *RC* model
$\mathbf{E}$	Feedforward matrix of the state-space averaged model of the nonisolated bidirectional DC-DC converter or of the modular power converter
$ESR_{0,j}$	Initial equivalent series resistance of the *j*th supercapacitor (group)
ESR_{EOL}	Equivalent series resistance at the end of life

$ESR_{k,j}$	Equivalent series resistance of the jth supercapacitor (group) at the time step k
ESR_{meas}	Measured equivalent series resistance approximated as the resonance frequency impedance
f_s	Switching frequency of the nonisolated bidirectional DC-DC converter or of the modular power converter
$G_{\text{C1}}(s)$	Outer loop proportional-plus-integral (PI) controller
$G_{\text{C2}}(s)$	Inner loop proportional-plus-integral (PI) controller
$G_{i_{\text{in}}d}(s)$	Inner loop control-to-input current transfer function
$G_{v_{\text{out}}d}(s)$	Open-loop control-to-output transfer function
$G_{v_{\text{out}}i_{\text{in}}}(s)$	Outer loop input current-to-output voltage transfer function
H	Parameter homogeneity
I_{in}	Nominal input current of the nonisolated bidirectional DC-DC converter or of the modular power converter
i_{in}	Input current of the nonisolated bidirectional DC-DC converter or of the modular power converter
i_{rms}	Dynamic RMS current of the supercapacitor (group)
$I_{\text{rms,0}}$	Constant relating supercapacitor RMS current to its effect on supercapacitor lifetime
I_{out}	Nominal output current of the nonisolated bidirectional DC-DC converter or of the modular power converters
i_{out}	Output current of the nonisolated bidirectional DC-DC converter or of the modular power converters
$i_{\text{out,max}}$	Output current of the modular power converter system
$i_{\text{sc},j}$	Current of the jth supercapacitor (group)
$i_{\text{sc,max}}$	Maximum (peak) current of the supercapacitor (group)
$i_{\text{sc,min}}$	Minimum current of the supercapacitor (group)
$I_{\text{sc,pp}}$	Peak-to-peak current of the supercapacitor (group)
i_{sto}	Energy storage or output current of the modular power converters in the energy storage of the modular multilevel converter submodule
$I_{\text{ref},j}$	Reference current of the inductor current of the jth modular power converter
j	Index for supercapacitors (groups) or modular power converters
k	Index for iterations
L	Inductance of the inductor of the nonisolated bidirectional DC-DC converter or of the modular power converter

L_{B} Inductance produced through the rolling or folding of the supercapacitor electrodes in the equivalent circuit model of the supercapacitor impedance response

L_{orig} Original inductance sizing of the inductor of the nonisolated bidirectional DC-DC converter

$M_j(D_j)$ Conversion ratio of the *j*th modular power converter

n Total number of cascaded modular power converters

N Number of time steps during the charging period

$n_{\mathrm{cells}}, N_{\mathrm{cells}}$ Number of cells in the string input to the modular power converter

N_{mod} Number of modular power converters per modular multilevel converter submodule

$n_{S,k-1}$ Size of the set *S*, which is the set of all converters predicted to saturate, at the *k*th check

P_j Average power charged to the *j*th supercapacitor (group) during the charging period

P_{max} Power rating (maximum) of the modular power converter system

$P_{\mathrm{sm}}^{\mathrm{max}}$ Power rating (maximum) of the modular multilevel converter submodule

P_{test} Test power of the modular power converter system

Q_1, Q_2 Switches of the nonisolated bidirectional DC-DC converter or of the modular power converter

R_0 Resistance modeling the contacts in the equivalent circuit model of the supercapacitor impedance response that is present in the whole frequency range or the resonance frequency impedance

R_C Resistance (equivalent series resistance) of the capacitor of the nonisolated bidirectional DC-DC converter or of the modular power converter

R_{cond} Supercapacitor thermal conduction resistance modeling heat transfer from the supercapacitor core to its case in the supercapacitor thermal behavior circuit model

R_{conv} Supercapacitor thermal convection resistance modeling heat transfer from the supercapacitor case to the air in the supercapacitor thermal behavior circuit model

R_{dch} Measured resistance (equivalent series resistance) of the resistor component of the supercapacitor *RC* model during the discharge phase

$R_{\mathrm{DS(on)}}$ On resistance of the MOSFET of the nonisolated bidirectional DC-DC converter or of the modular power converter

r_j Reliability indicator of the *j*th supercapacitor (group)

R_L Resistance (equivalent series resistance) of the inductor of the nonisolated bidirectional DC-DC converter or of the modular power converter

r_{max} Maximum among all the reliability indicators

R_{p} Resistance of the parallel resistor in the equivalent circuit model of the supercapacitor impedance response that is generated by the skin effect

r_{sat}	Factor slightly greater than unity serving as security margin
R_{sc}	Resistance (equivalent series resistance) of the resistor component of the supercapacitor *RC* model
$R_{\text{sc,meas}}$	Measured resistance (equivalent series resistance) of the resistor component of the supercapacitor *RC* model
RUL_j	Remaining useful life of the supercapacitor (group)
$\text{SC}_{\text{j,CB-Vave}}$	*j*th Supercapacitor (group) using the classical balancing approach with a switched resistor circuit averaging supercapacitor voltages
$\text{SC}_{j,\text{MC-CA}}$	*j*th Supercapacitor (group) using the modular power converter approach with control allocation
SoC	State of charge of the supercapacitor (group)
SoE_{ave}	Average state of energy of the supercapacitor (group)
SoE_{max}	Maximum average state of energy of the supercapacitor (group)
SoE_{min}	Minimum average state of energy of the supercapacitor (group)
SoH_j	State of health of the supercapacitor (group)
T_{a}	Ambient temperature
T_{s}	Settling time
$\mathbf{u}$	Input or control vector of the state-space averaged model of the nonisolated bidirectional DC-DC converter or of the modular power converter
$\mathbf{u}^*$	Optimal solution based on the pseudoinverse method for control allocation
$\mathbf{u}_{\text{d}}$	Desired control input vector
$\mathbf{u}_{\text{max}}$	Maximum saturation points or physical limits vector of the supercapacitors
$\mathbf{u}_{\text{min}}$	Minimum saturation points or physical limits vector of the supercapacitors
$\mathbf{v}$	Virtual control input vector representing the total constraint of the supercapacitors
V_0	Constant relating supercapacitor voltage to its effect on supercapacitor lifetime
v_{Cc}, v_C	Voltage of the capacitor of the nonisolated bidirectional DC-DC converter or of the modular power converter
$v_{C\text{sc}}$	Voltage of the capacitor component of the supercapacitor *RC* model
$v_{C\text{sm}}^{\text{u,l}}$	Voltage of the modular multilevel converter submodule capacitor
v_{in}	Input voltage of the nonisolated bidirectional DC-DC converter or of the modular power converter
$V_{\text{max,cell}}$	Maximum rated voltage of the supercapacitor cell
$V_{\text{max}}, V_{\text{sc}}^{\text{max}}$	Maximum rated voltage of the supercapacitor (group)

$V_{\text{min}}, V_{\text{sc}}^{\text{min}}$	Minimum voltage of the supercapacitor (group)
v_{oc}	Open-circuit voltage
V_{out}	Nominal output voltage of the nonisolated bidirectional DC-DC converter or of the modular power converter
$v_{\text{out},j}$	Output voltage of the *j*th modular power converter
$v_{\text{out,total}}$	Output voltage of the nonisolated bidirectional DC-DC converter or the total sum of output voltages of the modular power converters
$v_{R\text{sc}}$	Voltage of the resistor component of the supercapacitor *RC* model
$V_{\text{ref},j}$	Reference output voltage of the *j*th modular power converter
$V_{\text{ref,total}}$	Total sum of reference output voltages of the modular power converters or the bus voltage
$v_{\text{sc},j}$	Voltage of the *j*th supercapacitor (group)
$v_{\text{sc,max}}$	Maximum (peak) voltage of the supercapacitor (group)
$v_{\text{sc,min}}$	Minimum voltage of the supercapacitor (group)
$V_{\text{sc,oc}}$	Open-circuit voltage of the supercapacitor (group)
$V_{\text{sc,pp}}$	Peak-to-peak voltage of the supercapacitor (group)
$w_{k,j}$	Weighting factor representing the power of the *j*th modular power converter as a share of the output voltage regulation
$w_{k(\text{base}),j}$	Base weighting factor of the *j*th modular power converter at the *k*th check
$w_{k(\text{th}),j}$	Threshold weighting factor of the *j*th modular converter at the *k*th check
$w_{k(\text{th,c})}$	Threshold weighting factor at the *k*th check during charging
$w_{k(\text{th,d})}$	Threshold weighting factor at the *k*th check during discharging
$\mathbf{W}_u$	Weighting matrix for managing redundant supercapacitors based on their health or reliability
$\mathbf{x}$	State vector of the state-space averaged model of the nonisolated bidirectional DC-DC converter or of the modular power converter
$\dot{\mathbf{x}}$	Derivative of the state vector of the state-space averaged model of the nonisolated bidirectional DC-DC converter or of the modular power converter
$\mathbf{x}_0$	Initial conditions vector of the state-space averaged model of the nonisolated bidirectional DC-DC converter or of the modular power converter
$\mathbf{y}$	Output vector of the state-space averaged model of the nonisolated bidirectional DC-DC converter or of the modular power converter
Z_C	Impedance of the ideal capacitor
Z_{s}	Series impedance of the supercapacitor impedance

Z_{sc}	Impedance of the supercapacitor
Δt	Control strategy time step
η_{boost}	Efficiency of the boost mode of the nonisolated bidirectional DC-DC converter or of the modular power converter
η_{buck}	Efficiency of the buck mode of the nonisolated bidirectional DC-DC converter or of the modular power converter
θ	Dynamic temperature of the supercapacitor
θ_0	Constant relating supercapacitor temperature to its effect on supercapacitor lifetime
θ_{case}	Case temperature of the supercapacitor
θ_{core}	Core temperature of the supercapacitor
λ_j^{bl}	Baseline or nominal aging rate of the *j*th supercapacitor
μ	Mean or average
σ	Standard deviation
τ_0	Theoretical lifetime of the supercapacitor (group) at 0 V and 0 °C
τ_d	Dynamic lifetime of the supercapacitor (group)
Φ	Heat generation from Joule heating in the supercapacitor thermal behavior circuit model

List of Acronyms

AC	Alternating current
AGV	Automated guided vehicle
AMR	Autonomous mobile robot
BMS	Battery management system
CA	Control allocation
CB	Classical balancing
CCCD	Constant-current charge/discharge
COP 21	21st Conference of the Parties to the United Nations Framework Convention on Climate Change
DC	Direct current
DUT	Device under test
EDL	Electrical double layer
EDLC	Electrical double-layer capacitor
EFR	Enhanced frequency response
EIS	Electrochemical impedance spectroscopy
EOL	End of life
ESO	Electricity system operator
ESR	Equivalent series resistance
ESS	Energy storage system
EV	Electric vehicle
FCEV	Fuel cell electric vehicle
FPGA	Field-programmable gate array
GES	Gaz à effet de serre
GHG	Greenhouse gas
GIEC	Groupe d’experts intergouvernemental sur l’évolution du climat
HVDC	High-voltage direct current
IEA	International Energy Agency
IPCC	Intergovernmental Panel on Climate Change
LCOE	Levelized cost of electricity
LT-LEDS	Long-term low greenhouse gas emission development strategies
MC	Modular converter

MMC	Modular multilevel converter
NDC	Nationally determined contribution
OCV	Open-circuit voltage
PSH	Pumped-storage hydropower
PWM	Pulse width modulation
RMS	Root mean square
RUL	Remaining useful life
SLI	Starting, lighting, and ignition
SM	Submodule
SMS	Supercapacitor management system
SC	Supercapacitor
SoC	State of charge
SoE	State of energy
SoH	State of health
SR	Switched resistor
UPS	Uninterruptible power supply
VSC	Voltage source converter
xEV	Battery-powered electric vehicle
ZOH	Zero-order hold

Résumé général

Cette section propose un résumé général en français du contenu du manuscrit.

This section provides a general summary of the contents of the manuscript in French.

Introduction générale

La nécessité évidente de décarboniser les économies du monde entier d'ici le milieu du siècle a stimulé le développement et le déploiement de systèmes d'énergie durables ainsi que la recherche associée. Cette nécessité a été institutionnalisé par les Nations Unies avec son septième objectif de développement durable qui stipule : « garantir l'accès de tous à des services énergétiques fiables, durables et modernes à un coût abordable » [1]. Aujourd'hui, beaucoup d'équipements (systèmes embarqués, autonomes, énergies renouvelables, ...) nécessitent de stocker l'énergie. Le rôle que joue le stockage d'énergie est devenu fondamental dans le fonctionnement de ces systèmes. Au niveau du réseau électrique par exemple, la part des centrales électriques basées sur des sources d'énergie renouvelables telles que le soleil, le vent, la biomasse, la géothermie et l'hydroélectricité a considérablement augmenté au cours des dernières décennies en raison précisément de l'impératif de décarbonisation. D'autre part, l'autre domaine où les systèmes de stockage d'énergie sont incontournables est celui de la mobilité. À partir de ces deux exemples, nous pouvons clairement voir le rôle clé des systèmes de stockage d'énergie.

Les technologies de stockage d'énergie électrique que sont les batteries et les supercondensateurs nécessitent très souvent d'assembler des cellules individuelles en série. Cela nécessite alors un équilibrage de l'état de charge ou de la tension de chaque cellule en raison des caractéristiques hétérogènes du système composé par ces cellules. Deux cellules (que ce soient des éléments d'une batterie lithium-ion ou d'un pack de supercondensateurs) avec des caractéristiques « constructeur » identiques ne sont jamais vraiment uniformes. La tolérance sur les caractéristiques initiales des cellules engendre un déséquilibre initial de la tension aux bornes des éléments qui affecte à son tour le fonctionnement du système de stockage d'énergie. Par ailleurs, le placement physique des cellules dans un pack et l'environnement sont deux autres facteurs qui peuvent introduire des déséquilibres de tension. Un équilibrage de la tension de chaque cellule est donc nécessaire pour les maintenir dans de bonnes conditions de fonctionnement. Le circuit d'équilibrage qui réalise cette fonction peut soit dissiper l'énergie en surplus des cellules surchargées (équilibrage passif), soit redistribuer la charge des cellules surchargées vers les cellules sous-chargées (équilibrage actif). Le circuit d'équilibrage fait partie intégrante du BMS (battery management system) des batteries ou du

SMS (supercapacitor management system) du pack de supercondensateurs. Les travaux de cette thèse évoquent ces problématiques d'équilibrage ainsi que l'interfaçage de ces cellules avec le circuit de charge/décharge. Usuellement les cellules en série sont interfacées avec un bus continu par l'intermédiaire d'un seul convertisseur continu-continu commandable. Ce convertisseur peut être divisé en plusieurs convertisseurs modulaires plus petits interfaçant alors de plus petit assemblage de cellules en série. Cela crée un système modulaire dans lequel chaque convertisseur peut être contrôlé et assumer ainsi une tâche d'équilibrage pour son assemblage en série de cellules par rapport aux assemblages des autres convertisseurs.

Chapitre 1 Motivation et contexte

Le 12 décembre 2015, 196 délégations de pays ont convenu d'un traité juridiquement contraignant sur le changement climatique à la 21ème session de la Conférence des Parties (COP 21) à Paris. Le traité est connu sous le nom d'accord de Paris et est entré en vigueur le 4 novembre 2016. Son principal objectif est de limiter le réchauffement climatique à moins de 2 °C, voire 1,5 °C par rapport aux niveaux préindustriels. L'objectif peut être atteint si les pays atteignent le plus tôt possible le pic mondial d'émissions de gaz à effet de serre (GES), ce qui se traduira par un monde climatiquement neutre d'ici le milieu du siècle. Avec ce traité historique, l'accord de Paris implique de profondes transformations économiques et sociétales [2].

Pour évaluer les trajectoires possibles au cours du siècle, le Groupe d'experts intergouvernemental sur l'évolution du climat (GIEC) a examiné cinq scénarios d'émissions de projections de futurs modèles climatiques. Les cinq scénarios sont : (i) émissions de GES très élevées ; (ii) émissions élevées ; (iii) émissions intermédiaires ; (iv) faibles émissions avec des émissions de CO_2 diminuant jusqu'à zéro après 2050 ; et enfin, (v) faibles émissions avec des émissions de CO_2 diminuant jusqu'à zéro vers 2050. L'effet de toutes les émissions (GES et aérosols) a été pris en compte dans le total [3]. Tous les scénarios entraîneront une augmentation de la température. Seul le scénario à très faibles émissions sera dans l'objectif de l'accord de Paris qui permet de limiter l'augmentation de la température à moins de 2 °C, voire 1,5 °C. Par conséquent, les scénarios d'émissions faibles à très élevées sont tout simplement inenvisageable si nous voulons définitivement atteindre l'objectif de l'accord de Paris. Nous devons donc réduire drastiquement les émissions de GES afin qu'elle soit nulle vers 2050.

Au cœur des systèmes électrifiés se trouve souvent le système de stockage de l'énergie électrique. Ces dernières années ont été marquées par une explosion de la mobilité électrique [4]. Pour atteindre l'objectif de produire près de 2 millions de véhicules électriques et hybrides en France en 2030,

un plan d'investissement en dix points pour le pays a été défini d'ici 2030 ce qui implique donc des investissements majeurs dans le domaine des systèmes de stockage d'énergie. Ceci a entraîné l'annonce récente de Verkor, une société française fondée en 2020 avec le soutien de grands groupes français, européens et d'institutions gouvernementales, qui vient d'annoncer avoir choisi la ville de Dunkerque parmi 40 candidats comme site de sa première Gigafactory pour la production de cellules de batteries. Celle-ci ouvrira en 2025 avec une capacité de production annuelle initiale de 16 GWh [5]. Cela suit la tendance d'autres entreprises mondiales comme le suédois Northvolt, qui a produit sa première cellule en 2021 dans sa Gigafactory [6], le norvégien FREYR qui prévoit de commencer la production en 2022 [7], et bien sûr, Tesla aux États-Unis qui a ouvert pour la première fois une Gigafactory de batteries en 2016. C'est d'ailleurs Tesla qui a utilisé pour la première fois le terme Gigafactory pour une usine de fabrication capable de produire des GWh de batteries [8].

L'analyse du marché concernant les systèmes de stockage d'énergie électrique ne fera que croître dans les prochaines années que ce soit pour les batteries ou les supercondensateurs. Par rapport aux supercondensateurs, pour une masse donnée, les batteries peuvent stocker 30 fois plus d'énergie. D'autre part, pour une masse donnée, les supercondensateurs peuvent fournir plus de puissance que les batteries car la charge est stockée par adsorption sur la surface des électrodes. Les batteries sont donc considérées comme des dispositifs à haute densité d'énergie, tandis que les supercondensateurs sont à haute densité de puissance. Cela se reflète également au niveau du prix, les batteries étant plus chères par kW de puissance et les supercondensateurs plus onéreux par kWh d'énergie.

Cette thèse aborde la thématique de l'extension de la durée de vie des systèmes de stockage d'énergie électrique d'un point de vue du coût du cycle de vie ou du coût actualisé de l'énergie ou LCOE (levelized cost of energy). Ces coûts sont importants car ils prennent en compte les coûts sur la durée de vie totale du système [9]. Les inhomogénéités causées à la fois par la dispersion des caractéristiques initiales et le fonctionnement réel des cellules de stockage d'énergie entraînent des durées de vie inégales entre cellules individuelles. Pour l'ensemble du système de stockage d'énergie, sa durée de fin de vie est généralement considérée comme l'instant où la cellule la plus faible le constituant atteint sa propre fin de vie. La cellule la plus faible dicte ainsi la durée de vie de l'ensemble du système. Il est donc évident que la durée de vie du système n'est pas optimisée puisque les cellules les plus saines n'auront pas atteint leur propre fin de vie au terme de la durée de vie du système. Notre approche dans cette thèse est de réduire et d'essayer d'équilibrer l'écart entre les durées de vie des cellules dans un système de stockage d'énergie. Un algorithme de gestion d'énergie sera appliqué afin que les contraintes électriques sur les cellules les plus faibles soient réduites et que l'énergie qui leur a été retirée soit supportée par les cellules les plus saines. Il est ainsi montré dans les discussions du chapitre 4 que l'extension de la durée de vie du système de stockage est réalisée en équilibrant la durée de vie des cellules.

Chapitre 2 Equilibrage des tensions de supercondensateurs

La tension nominale limitée des supercondensateurs nécessite d'en connecter plusieurs en série dans la plupart des applications. Ainsi pour répondre aux applications, les systèmes de stockage sont souvent une association en série et parallèle de cellules [10]. Étant donné que les paramètres des supercondensateurs ne sont jamais totalement uniformes, cela engendre des déséquilibres de tension entre les cellules en série. Ce déséquilibre initial s'aggrave ensuite en cours d'exploitation du fait du vieillissement irrégulier des cellules [11]–[13]. Ainsi, un circuit d'équilibrage des tensions des cellules est nécessaire pour assurer un fonctionnement sûr et une durée de vie acceptable des supercondensateurs [10], [11], [14]. Cela nécessite donc une surveillance continue des tensions. Avec la surveillance des courants et des températures, le système de management peut donc assurer un fonctionnement sûr du système de stockage en s'interfaçant avec les autres convertisseurs [10], [15].

Il existe deux types de circuits d'équilibrage : les passifs (ou dissipatifs) et les actifs (ou redistributifs). Dans l'équilibrage passif, l'excès de charge dans les cellules est dissipé par des résistances. C'est la stratégie la plus simple et la moins chère à mettre en place. L'équilibrage actif redistribue lui l'énergie des cellules surchargées vers les cellules sous-chargées, ce qui est plus efficace mais plus coûteux. En effet, cette stratégie est plus onéreuse à mettre en œuvre en raison des composants supplémentaires et des systèmes de contrôle plus compliqués [13], [16]–[18]. Récemment, une troisième approche de l'équilibrage a émergé. Elle est basée sur les convertisseurs d'énergie modulaires qui interfacent les dispositifs de stockage d'énergie avec le reste du système. L'équilibrage des cellules est alors actif et s'il y a un convertisseur modulaire par cellule, il n'y a pas besoin de circuits d'équilibrage séparés. La gestion de l'équilibrage peut être intégrée dans les mêmes algorithmes qui contrôlent les tensions de sortie des convertisseurs modulaires. La régulation et l'équilibrage de la tension du bus continu, sans circuit supplémentaire ni redistribution de charge, sont ainsi possibles de manière efficace et modulaire [19]–[26].

Pour les convertisseurs modulaires, une architecture continu-continu bidirectionnelle en courant en demi-pont a été choisie. Deux applications tirées de deux études antérieures précédentes ont été considérées : l'applications Hybus de récupération d'énergie de freinage d'un trolleybus et l'application SuperGrid pour stabiliser la fréquence des réseaux [27]–[29]. Pour la première application, l'architecture modulaire permet une nouvelle flexibilité en termes de régulation bénéfique pour la gestion des déséquilibres électrothermiques [27]. La deuxième application porte sur l'intégration de supercondensateurs dans des convertisseurs multiniveaux modulaires (MMC), composés de centaines de sous-modules (SM) [28].

Un grand nombre de stratégies différentes d'équilibrage de l'état de charge ou de la tension, existent principalement pour les batteries [13], [16]–[18], [20], [21], [24], [30]. Bien qu'elles puissent également être utilisées pour les supercondensateurs, elles sont souvent lentes et les équilibrages peuvent prendre de quelques minutes à quelques dizaines de minutes. En ce qui concerne les convertisseurs modulaires, aucune étude n'a encore abordé le problème de la saturation de la commande des convertisseurs qui résulte de leur architecture et des caractéristiques des supercondensateurs. Nous proposons donc dans ce chapitre une méthode d'équilibrage des tensions des supercondensateurs qui s'effectue, dans la mesure du possible, lors d'une seule période de charge grâce à la commande des convertisseurs modulaires.

La stratégie d'équilibrage est de charger les supercondensateurs jusqu'à ce qu'ils atteignent leur tension nominale maximale et d'atteindre cette pleine charge en même temps. Les équations nécessaires pour contrôler les convertisseurs d'énergie modulaires et équilibrer les tensions des supercondensateurs ont été développées. S'il n'y a pas de problème de saturation de la commande des convertisseurs modulaires, une stratégie classique peut être utilisée. Il faut alors qu'il y ait suffisamment de marge entre la plage de tension en entrée et celle en sortie des convertisseurs. Cependant, dans ce cas un rapport de conversion élevé est nécessaire, ce dont le rendement souffre. Par ailleurs l'emploi de la plage complète d'état d'énergie des supercondensateurs signifie une utilisation presque complète de la plage des rapports cycliques des convertisseurs entraînant dans certains cas la nécessité d'un faible rapport de conversion. La saturation de commande est donc presque inévitable pour atteindre le double objectif de charge et d'équilibrage des supercondensateurs.

Il est possible de modifier la stratégie d'équilibrage de tension pour tenir compte de la saturation de la commande. Si nous savons qu'un convertisseur saturera à n'importe quel moment de la période de charge, nous pouvons le saturer volontairement dès le départ. Cela est effectué pour corriger et augmenter la quantité d'énergie des supercondensateurs connectés aux convertisseurs qui ne saturent pas. Ainsi, les supercondensateurs reliés aux convertisseurs qui finissent par saturer se chargent avec leur juste part d'énergie. Le défi dans la mise en œuvre de cette méthode est que nous devons savoir quels convertisseurs finiront par saturer. Un facteur de pondération a été spécialement défini pour être constant tout au long de la période de charge des supercondensateurs en considérant les énergies individuelles et totales nécessaires pour les charger. Les convertisseurs doivent avoir des tensions de sortie constantes. Le facteur de pondération est utilisé pour savoir quels convertisseurs finiront par saturer. Adapter la stratégie classique consiste donc essentiellement à prévoir quels convertisseurs satureront. Ceux-ci sont alors délibérément saturés au début pour diminuer leur part d'énergie globale et réaliser à terme un équilibrage de tension. Cette stratégie proposée avec prédiction des convertisseurs qui finiront par saturer est une nouvelle contribution concernant les stratégies d'équilibrage de tension.

Nous avons simulé le système et la stratégie décrite. Pour démontrer le bon fonctionnement de cette dernière, nous avons modélisé le système de récupération d'énergie de 50 kW de l'application Hybus et avons simulé l'ensemble. Le dimensionnement des convertisseurs modulaires découle de l'application Hybus qui utilise un seul convertisseur de 50 kW pour interfacer 120 cellules de supercondensateurs de 3 000 F pour récupérer l'énergie de freinage et assister l'alimentation du trolleybus lors des microcoupures électriques [27]. La température auxquels sont soumis les supercondensateurs est un facteur important puisqu'elle influe l'évolution de leur capacité et de leur résistance équivalente série (ESR). Or il est difficile d'assurer l'homogénéité thermique d'un empilement de supercondensateurs [31]. Les cellules ont donc été regroupées en fonction de leur température pour assurer un déséquilibre de tension entre cellules minimal. Ainsi, nous avons décidé de regrouper les supercondensateurs dans 10 assemblages de 12 cellules et simulé le comportement de 10 convertisseurs modulaires. Les simulations ont été exécutées pour trois cas d'étude avec des tensions initiales différentes.

La stratégie a également été mise en œuvre expérimentalement sur un prototype à échelle réduite de 30 W avec trois convertisseurs modulaires bidirectionnels en courant [32]. Ces derniers étaient contrôlés par une machine cible en temps réel Speedgoat qui interagissait avec l'interface utilisateur de son poste de travail via Simulink Real-Time Explorer. Le système de contrôle a été programmé dans la machine cible à l'aide de MATLAB et Simulink.

Comme pour l'étude en simulation, celle expérimentale a validé la stratégie prenant en compte la saturation de la commande des convertisseurs modulaires. Celle-ci est rapide et fonctionne lors des périodes de charge et de décharge.

Chapitre 3 Caractérisation en ligne des supercondensateurs

Parmi les différentes solutions de stockage d'énergie électrique, les supercondensateurs sont l'une des technologies les plus efficaces avec les durées de vie les plus longues. Ils sont capables d'effectuer entre des centaines de milliers et un million de cycles de charge-décharge puisque théoriquement aucune réaction chimique n'a lieu au niveau de leurs électrodes [10]. Leur vieillissement est fonction de leur température et de leur niveau de tension en considérant les effets du cyclage comme négligeable [11], [33]. L'effet du cyclage peut être aussi pris en compte pour quantifier leur vieillissement [12], [34].

Il existe une tolérance sur les caractéristiques des supercondensateurs compte tenu de leurs constituants et des procédés de fabrication qui ne peuvent être rigoureusement identiques [11], [14].

C'est également le cas pour d'autres dispositifs de stockage d'énergie électrique comme pour les batteries [10]. Le déséquilibre initial est souvent exacerbé pendant leur fonctionnement compte tenu de leur environnement et de leur vieillissement. Par exemple, une différence de température de 10 °C entre cellules peut engendrer des disparités de durée de vie d'un facteur deux [11]. La surveillance de l'état de santé des cellules peut donc se justifier puisqu'un vieillissement non uniforme entraîne une durée de vie plus courte du système de stockage cette dernière étant généralement considérée comme égale à celle de la cellule la plus faible. Une cause principale à l'origine du vieillissement des supercondensateurs est liée aux impuretés dans les électrodes. Les surtensions, les températures excessives et le cyclage accélèrent le vieillissement [35].

La capacité et l'ESR d'une cellule sont des signatures de son état de santé Ces deux paramètres peuvent être déduits de mesures de courant et de tension lors de cycles de charge et de décharge [36]. Un supercondensateur peut être considéré comme étant en fin de vie une fois si sa capacité est réduite de 20 % ou si son ESR a doublé.

Un supercondensateur peut être caractérisé par sa réponse en courant à une tension alternative (ou vice-versa). Ainsi une mesure d'impédance à l'aide d'une tension ou d'un courant alternatif à une fréquence définie est l'une des méthodes de caractérisation standard habituellement employées pour les dispositifs électrochimiques comme les supercondensateurs [14], [37], [38]. Cette méthode, usuellement appelée spectroscopie d'impédance électrochimique (EIS), permet de déduire l'impédance en fonction de la fréquence. L'utilisation de petits signaux de tension et de courant permet de supposer des caractéristiques linéaires. Un balayage en fréquence permet de déterminer la réponse d'un supercondensateur sur une grande échelle de temps allant, par exemple, de la microseconde à l'heure. Les résultats sont généralement présentés soit sur un diagramme de Bode pour montrer l'impédance et l'angle de phase en fonction de la fréquence ou soit sur un diagramme de Nyquist pour montrer l'impédance dans un plan complexe [37].

Il est cependant très difficile, voire impossible, de caractériser un supercondensateur en cours d'utilisation dans une application par cette méthode. Une méthode de caractérisation en ligne populaire consiste à utiliser les observateurs. Ceux-ci utilisent des algorithmes qui tirent parti de la connaissance du système, du mécanisme de conversion d'énergie et du capteur lui-même en plus des signaux mesurés pour le contrôle du système [39]. Il est également possible de mesurer l'ESR par l'intermédiaire du circuit d'équilibrage. Par exemple, lors d'un équilibrage passif, en commandant les interrupteurs interfaçant les résistances dissipant l'énergie des cellules en surcharge par un signal à une fréquence proche de celle de résonance de la cellule, l'ESR peut être déduit [40].

Une autre méthode de caractérisation en ligne utilise le contrôle du convertisseur d'énergie relié au dispositif de stockage. Cette méthode a déjà été utilisée dans la mesure en ligne de l'impédance de batteries [41], [42]. Nous proposons d'utiliser cette même méthode pour les supercondensateurs par le contrôle des convertisseurs d'énergie modulaires. Il est alors nécessaire d'exciter le supercondensateur avec un petit signal alternatif à une certaine fréquence sans interférer son fonctionnement mais afin de solliciter une réponse. Cela a été effectué dans notre cas grâce à l'ajout d'un petit signal dans le contrôle des convertisseurs d'énergie modulaires via le rapport cyclique.

Cette méthode de caractérisation en ligne a été mise en œuvre expérimentalement sur le prototype à échelle réduite de 30 W comportant trois convertisseurs modulaires. La perturbation du rapport cyclique a été effectuée sur le système de contrôle grâce à la programmation de la machine cible à l'aide de MATLAB et Simulink. Nous avons ainsi pu effectuer des mesures d'ESR par la méthode de caractérisation en ligne avec une erreur de mesure de 8,9 %. Cela a permis de valider la méthode qui a été considérée comme suffisamment précise pour notre besoin. Cette méthode de caractérisation en ligne est utilisée dans le chapitre suivant pour diagnostiquer l'état de santé des supercondensateurs.

Chapitre 4 Optimisation de la durée de vie de système des supercondensateurs

Une distribution de température irrégulière dans un pack de supercondensateurs conduit à un vieillissement précoce des cellules le constituant. Comme déjà mentionné, chaque augmentation de température de 10 °C peut réduire de moitié la durée de vie d'un supercondensateur [11]. Ainsi les cellules les plus chaudes d'un pack de supercondensateurs peuvent atteindre leur critère de fin de vie avant celui des plus froides. Par conséquent, cela conduit à une durée de vie plus courte du système de stockage. Nous proposons donc dans ce chapitre de minimiser les déséquilibres entre les vieillissements des cellules en gérant d'une manière intelligente les supercondensateurs en fonction de leur état de santé (SoH).

Le système du projet Hybus sert d'exemple d'application pour ce chapitre. Ce système permet, grâce à la récupération de l'énergie de freinage d'un trolleybus, d'alimenter un système de stockage à base de supercondensateurs pour alimenter les auxiliaires du véhicule [31], [43], [44]. Dans le cadre du projet Hybus, 120 supercondensateurs d'une tension totale variant de 120 à 300 V étaient connectés en série à un convertisseur continu-continu bidirectionnel en courant dont la sortie était régulée à 350 V. Afin de pouvoir appliquer notre méthode d'allocation de la commande qui concerne les convertisseurs modulaires pour ce projet, nous avons opter pour la partition du convertisseur DC-DC en plus petits convertisseurs. Ainsi, les 120 supercondensateurs sont regroupés par 10 et les assemblages de 12 cellules

sont chacun connectés à un des 10 convertisseurs modulaires dont les sorties sont connectées en série. Diviser le convertisseur DC-DC unique en dix convertisseurs modulaires permet d'améliorer la fiabilité ainsi que d'optimiser la durée de vie des supercondensateurs en les homogénéisant. Puisque les sorties des convertisseurs modulaires sont connectées en série, elles sont parcourues par le même courant de sortie. Ainsi le contrôle de la quantité d'énergie qui charge et décharge les assemblages de supercondensateurs peut être effectué via les tensions de sortie des convertisseurs.

Un autre avantage que la modularité apporte au système multi-convertisseurs réside dans la redondance. Ainsi, lorsqu'il y a un défaut dans l'un des convertisseurs, les autres peuvent encore fonctionner et supporter la charge. Contrôler un tel système avec les objectifs explicites de tolérance aux pannes et de fiabilité est une tâche difficile. L'allocation de commande est une méthode qui peut être utilisée pour de tels systèmes où la matrice de pondération est utilisée pour attribuer l'entrée de commande aux différents actionneurs. Des solutions d'optimisation peuvent être utilisées pour résoudre le problème d'allocation de commande. Elles visent à rechercher la solution optimale, la meilleure s'il y a plusieurs solutions, ou la plus faisable s'il n'existe pas de solution exacte. La nature analytique de la solution optimale par la méthode pseudo-inverse facilite son application dans de nombreux systèmes. Bien qu'il n'y ait aucune garantie que la solution n'engendre pas de saturation de la commande parce que la contrainte n'a pas été prise en compte, il existe des méthodes. Dans la méthode pseudo-inverse redistribuée, par exemple, les actionneurs saturés sont retirés du problème d'optimisation. La formule pseudo-inverse est alors juste résolue pour les actionneurs non saturés restants [45], [46]. Pour atteindre nos objectifs, nous utilisons un module d'allocation de commande qui permet de générer des trajectoires de références pour les boucles internes d'asservissement. Sa mise en œuvre est facile avec la formule de la solution optimale. Cependant, pour utiliser cette méthode pour obtenir les tensions de référence nécessaires au contrôle des convertisseurs modulaires, un indicateur de fiabilité de la matrice de pondération basée sur le modèle de durée de vie des supercondensateurs doit être conçu.

Dans le système général, le taux de vieillissement d'un actionneur sert d'indicateur de fiabilité pour l'allocation de commande. Il existe de nombreuses définitions du taux de vieillissement et les définitions spécifiques dépendent fortement des composants, des systèmes et des conditions d'étude [45], [46]. Le taux de défaillance est connu comme la fréquence de défaillance d'un composant ou d'un système et s'exprime en nombre de défaillances par unité de temps. Dans le système que nous considérons, nous avons considéré comme taux de vieillissement l'inverse de la durée de vie restante des supercondensateurs. La formule, lorsqu'elle est appliquée au scénario actuel, aboutit à ce que la différence de l'indicateur de fiabilité et donc de durée de vie utile restante diminue avec le temps.

Concernant la simulation, le modèle d'un supercondensateur a été implémenté à l'aide de Simscape, un environnement au sein de Simulink pour la modélisation et la simulation physiques multi-domaines. Une résistance variable pour l'ESR et un condensateur variable pour la capacité représentent le modèle adopté du supercondensateur. Pour déterminer les critères de fin de vie d'un supercondensateur, nous utilisons le modèle de durée de vie dynamique développé au laboratoire [12]. Le critère de fin de vie correspond à un doublement de l'ESR sachant que la valeur de l'ESR est mise à jour à chaque itération. Le même principe est utilisé pour la capacité, mais en tenant compte comme critère de fin de vie d'une décroissance de la capacité de 20 %. Nous avons exprimé le SoH du supercondensateur en considérant les variations de l'ESR. Un paramètre important influençant le vieillissement des supercondensateurs est la température. Pour le comportement thermique d'un supercondensateur, un modèle de type circuit électrique équivalent est utilisé et présenté [31], [47]. La température au cœur du supercondensateur (en °C) est introduite dans le modèle de durée de vie dynamique. Pour compléter les paramètres du modèle de durée de vie, des capteurs de tension et de courant ont été utilisés dans le modèle Simscape pour la prise en compte de ces mesures.

Nous avons simulé ici un système plus petit de trois convertisseurs modulaires. Le module d'allocation de commande fournit les tensions de référence des convertisseurs. Les caractéristiques électriques des trois assemblages de supercondensateurs, chacun relié à un convertisseur modulaire, sont considérées comme identiques à l'exception de leur capacité initiale, de l'ESR initiale et de la résistance thermique de convection. La variation des capacités a été réglée pour simuler les conditions réelles et induire une différence dans les tensions des assemblages de supercondensateurs à la fin d'un cycle de décharge-charge. Une comparaison des résultats avec ceux pour un équilibrage classique sera ainsi étudiée. La variation des capacités est également accompagnée d'une variation de l'ESR initiale. La variation de la résistance thermique de convection a été réalisée pour simuler les différentes positions des assemblages de supercondensateurs dans le pack de 120 cellules. La stratégie d'équilibrage de durée de vie dans le cadre de l'utilisation des convertisseurs modulaires est comparée avec celle lors d'un équilibrage classique. Pour cette dernière un circuit dissipatif avec résistances commutées est utilisé. Les tensions des supercondensateurs sont mesurées à chaque période et si un assemblage possède une tension supérieure à 1 % du minimum de celle de tous les autres groupes, cet assemblage est shunté sur la résistance. La comparaison des résultats de simulation montre que l'utilisation de convertisseurs modulaires commandés avec une stratégie d'équilibrage de durée de vie peut prolonger la durée de vie du système de 42 %. Les états de santé des supercondensateurs sont beaucoup plus proches les uns des autres alors qu'ils sont plus dispersés lors d'un équilibrage classique. La durée de vie du système est prolongée, car l'assemblage de supercondensateurs le plus fiable est plus sollicité électriquement que les deux autres, qui sont donc eux libérer des contraintes électriques les plus sévères.

L'effet des convertisseurs modulaires sur les températures des supercondensateurs est également positif. Avec des circuits d'équilibrage classiques, il y avait initialement une différence d'environ 3 °C entre les assemblages, celle-ci ayant augmenté jusqu'à une dizaine de degrés Celsius à la fin de vie des supercondensateurs. Avec les convertisseurs modulaires, la stratégie a réussi à maintenir les températures proches les unes des autres sans dépasser une différence de 1 à 2 ° C pendant la majeure partie de la durée de vie du système.

Nous nous sommes aussi intéressés à une autre application où nous avons utilisé la même approche d'optimisation de la durée de vie. Celle-ci concerne le stockage d'énergie électrique utilisé pour fournir des services au réseau électrique. L'énergie peut être stockée pendant les heures creuses, lorsque le prix est au plus bas et réutilisée aux heures de pointe où le prix est plus élevé. Les systèmes de stockage d'énergie peuvent aussi être utilisés en complément des sources d'énergie renouvelables [48].

Le courant continu à haute tension (HVDC) est apparu comme une solution au transport de l'électricité sur de longues distances, rendant possible l'échange d'énergie électrique intra et intercontinental et permettant de surmonter certains obstacles géographiques. Les sources d'énergie renouvelable ne sont pas nécessairement abondantes à l'endroit où le besoin en énergie est le plus important, c'est-à-dire dans les centres industriels et urbains. Dans ce contexte, le transport de l'électricité en courant continu à haute tension peut être une solution optimale. Les convertisseurs de tension (VSC) capables de convertir la tension AC en une tension DC sont au cœur de la transmission HVDC (VSC-HVDC). Les systèmes VSC-HVDC sont idéaux pour un transport robuste et efficace de l'énergie électrique à partir de sources distantes. Ils constituent les éléments principaux des futurs super-réseaux qui permettront aux pays d'échanger de gros volumes d'énergie en fournissant l'électricité là où elle est nécessaire [49].

Un système VSC-HVDC peut être contrôlé dans sa plage de fonctionnement, permettant une exportation ou une importation complète de puissance active. Cela introduit une flexibilité supplémentaire pour maintenir la qualité de l'alimentation des réseaux AC connectés. Les convertisseurs multiniveaux modulaires (MMC) constituent une topologie de choix dans les systèmes VSC-HVDC. L'énergie provenant des sources renouvelables étant intermittente, elle peut être stockée dans les réserves tournantes ou des systèmes de stockage électrochimique [49]. Dans le cadre des MMC, des supercondensateurs ont récemment été intégrés dans des sous-modules MMC [29], [32], [50]. Au lieu d'un seul système de stockage d'énergie connecté à un bus continu commun, plusieurs supercondensateurs peuvent être répartis dans les sous-modules MMC. La commande de cette

configuration permet d'atténuer les fluctuations basse fréquence du sous-module MMC du côté des supercondensateurs et d'équilibrer leur état de charge (SoC) [32], [50].

Le profil de charge lié à cette application réseau est donc très différent de celui du projet Hybus qui est caractérisé par un fort cyclage. Dans le cas de l'application réseau de SuperGrid, le vieillissement est principalement calendaire même s'il y a parfois quelques appels de courant. L'indicateur de fiabilité précédemment présenté ne fonctionne alors plus dans ce cas de vieillissement calendaire indépendant donc de la sollicitation en courant. Pour résoudre ce problème, nous avons considéré l'inverse de l'indicateur de fiabilité défini plus haut. La stratégie de durée de vie avec ce nouvel indicateur de fiabilité a été implémenté dans MATLAB et Simulink. Les convertisseurs MMC sont très volumineux et occupent des installations entières. Dans notre cas, ils sont constitués de 2 400 sous-modules. Puisque les MMC ont 6 demi-bras, chaque demi-bras comporte 400 sous-modules. Il n'est pas nécessaire de simuler tous les sous-modules mais il suffit d'en simuler qu'un seul pour démontrer le bon fonctionnement de notre approche.

Pour la simulation, il a été supposé que les harmoniques présents dans les supercondensateurs avaient été éliminés par le contrôle des convertisseurs modulaires. Il est en effet essentiel qu'ils soient filtrés pour éviter de surdimensionner le système et pour prolonger la durée de vie des supercondensateurs [32], [50]. La simulation a donc été réalisée purement en courant continu. Comme dans l'application du projet Hybus, l'état d'énergie (SoE) opérationnel a été limité de 25 % à 100 %. Le point médian de cette fourchette est de 62,5 %. Une nouvelle formulation pour le SoE de tous les supercondensateurs a été considérée sans nécessairement maintenir les tensions des cellules individuelles des supercondensateurs à 62,5 % de SoE.

Les résultats de simulation montrent que l'assemblage de supercondensateurs le plus fiable supporte la plus grande sollicitation électrique traduite par la tension la plus élevée. L'assemblage de supercondensateurs avec le moins bon état de santé reçoit de son côté la tension la plus faible. Ainsi la durée de vie de l'ensemble des supercondensateurs est optimisée. L'évolution de l'ESR et du SoH montre que la méthode d'optimisation de la durée de vie du système a pour effet d'équilibrer les durées de vie des assemblages. Pour cette application réseau, cet équilibrage est assez long puisque les convergences d'ESR et de SoH sont arrivées au bout de la septième année.

Par rapport à un équilibrage classique, la méthode d'optimisation de durée de vie a permis une prolongation de cette dernière de 13% (ou 10,5 mois). Pour l'application réseau, cette amélioration (13%) est donc moins importante que celle de l'application dans le cadre du projet Hybus (42%). Cela s'explique par la nature des profils de charge. Dans le cas du projet Hybus, les niveaux de courant dans les supercondensateurs sont élevés alors qu'ils sont nuls la plupart du temps dans l'application réseau.

Dans ce dernier cas, la méthode d'optimisation de la durée de vie n'a donc pas la possibilité de contrôler la contribution en courant lors du vieillissement.

La méthode d'optimisation de la durée de vie des supercondensateurs dans le cadre de leur utilisation dans un convertisseur MMC a été implémentée sur un prototype expérimental d'un sous-module à échelle réduite de 30 W conçu par SuperGrid Institute [32], [50]. Ce banc de test est composé de trois convertisseurs d'énergie modulaires, de l'instrumentation en courant, tension et température, d'une machine cible temps réel Speedgoat et d'une alimentation Toellner TOE 7621-40 à quatre quadrants programmée pour simuler un sous-module MMC,

Trois cartes filles contenant les supercondensateurs testés ont été placées à l'intérieur d'un four Memmert UFP 500. Cet environnement à haute température permet d'accélérer le vieillissement des cellules. Les deux premiers assemblages de supercondensateurs se trouvent directement dans l'environnement du four qui a été réglé à 80 °C. Le dernier assemblage a lui été recouvert d'une boîte et placé proche du passage de câble du four. Celui-ci était donc à une température plus froide proche de 68 °C. Il a été constaté très tôt au cours des tests que la variation des valeurs d'ESR avec le vieillissement était beaucoup plus lente que celle de la capacité. Pour cette raison, il a été décidé que la capacité équivalente des assemblages de supercondensateurs serait également mesurée en ligne par une simple méthode de charge à courant constant.

Nous avons montré expérimentalement de nouveau que l'optimisation de la durée de vie des supercondensateurs passe par l'équilibrage de leur durée de vie individuelle. En effet, cela se traduit par l'équilibrage des capacités des assemblages de supercondensateurs.

Conclusion générale

Les travaux présentés dans cette thèse étudient l'amélioration de la durée de vie des supercondensateurs par l'utilisation de convertisseurs d'énergie modulaires. Pour atteindre cet objectif, deux cas d'étude ont été considérés : l'alimentation des auxiliaires de trolleybus à base de supercondensateurs dans le cadre du projet Hybus et l'intégration de supercondensateurs dans un convertisseur MMC pour une application réseau (SuperGrid).

Les trois contributions apportées constituent les chapitres principaux :

1. Développement d'une stratégie d'équilibrage de tension des supercondensateurs basée sur l'énergie et adaptée à la saturation de commande des convertisseurs modulaires.
2. Développement de méthodes de caractérisation en ligne de supercondensateurs pouvant fournir des mesures de capacité et d'ESR au fil du temps.

3. Développement d'une méthode d'optimisation de la durée de vie des supercondensateurs par utilisation de convertisseurs modulaires.

Les deux premières contributions font partie intégrante de l'objectif principal de cette thèse, qui est la troisième contribution.

Il reste des problèmes techniques qui doivent être résolus par des futurs travaux sur ce sujet, la plupart ayant été répertoriés. Cette thèse a montré que la méthode proposée peut apporter des résultats prometteurs mais qu'ils sont dépendants de l'application considérée. La méthode proposée dans le cadre de cette thèse permet d'optimiser la durée de vie des systèmes de stockage d'énergie.

General Introduction

The clear need to decarbonize economies around the world by the middle of the century has spurred research, development, and deployment of sustainable energy systems. In fact, this imperative has been institutionalized by the United Nations as its seventh sustainable development goal: “ensure access to affordable, reliable, sustainable and modern energy for all.”

What underlies the seventh goal is the concept of energy security, which is defined by the International Energy Agency (IEA) as “the uninterrupted availability of energy sources at an affordable price.” In modern energy systems, the assurance of security almost often needs some form of energy storage. Indeed, the role energy storage plays has become an integral requirement in the operation of many systems. At the level of the electric grid for example, the share of power plants based on renewable energy sources such as the sun, wind, biomass, geothermal, and hydropower has grown tremendously in the past decades precisely because of the imperative of decarbonization. While the electricity from the latter three sources can be dispatched on demand much like traditional fossil fuel-based plants, the same is not true for intermittent renewable energy sources like the sun and the wind. This is where energy storage comes into the picture. At times of generous electricity production, the excess can be stored and later dispatched when needed. Thus, the unprecedented growth in solar and wind power plants has been accompanied by a similar growth in the requisite energy storage. At the level of individual consumers, another area where energy storage is the key enabling technology is in mobility. The increased demand for electric vehicles (EVs) has necessitated construction of battery Gigafactories able to supply the needs of the industry. Electricity is stored in the EV battery energy storage system, which is later supplied to the powertrain as needed to move the EV forward. From the two examples, we can clearly see the key role of energy storage in modern energy and power systems.

Electrochemical energy storage technologies like batteries and supercapacitors come in the form of individual cells. This configuration necessitates balancing because of all the sources of variance in characteristics possible in a system composed of many cells. One well-known fact for any modern process is quality control by means of tolerance. A product or a service’s uniformity can be assured to a certain extent with a tight tolerance. The flip side, however, is that even with the most modern manufacturing technologies, any two of the same product or service is not really uniform. This goes as well for battery and supercapacitor cells. The tolerance in the initial characteristics accounts for an initial imbalance that in turn affects the energy storage system’s operation and this is just one among many. The physical placement and the environment are two other factors that can introduce variance. As already said, batteries and supercapacitors come in cells that need to be stacked together to be usable in

many applications. They are also devices that produce heat when used. An individual cell's placement relative to other cells then has an effect on its temperature as the core of the stack heats up more compared to the margins. A cell placed in the core of a stack is expected to have a much higher operational temperature compared to others. This goes to show that the current characteristics of individual electrochemical cells are influenced by many imbalances. Balancing is required in order to maintain an electrochemical energy storage system within operating conditions.

The preceding discussion illustrated the need for balancing when electrochemical energy storage cells are used in an application. It can be implemented in circuits that can either dissipate extra charge in overcharged cells (passive) or redistribute charge from overcharged to undercharged cells (active). Balancing control is commonly integrated in a management system that was designed for the electrochemical energy system. Aside from balancing, the management system takes charge of cell monitoring, protection, estimation, and optimization, and interfacing with other devices or systems. This thesis takes advantage of this whole integrated system interfacing electrochemical cells with balancing and management systems. A whole stack of batteries and supercapacitors are generally interfaced by means of a single controllable static converter. The converter can be partitioned into smaller converter modules capable of interfacing smaller cell groups of the stack. This creates a modular system where each modular converter can be controlled to also take on the task of balancing. It will be shown in the next chapters that the system works for both classical balancing (balancing cell voltages) and a newly proposed lifetime balancing (balancing reliabilities).

The thesis is organized in four chapters. Chapter 1 starts with a global overview of the imperative to decarbonize energy systems. It also situates energy storage in the context of the larger energy and transportation systems providing the latest directions for its markets. The chapter also gives a brief overview of the need to take into account cell lifetimes in supercapacitor energy storage systems. Chapter 2 starts with an exposition on the literature on energy storage balancing. It then proceeds to describe the systems involved in a modular converter system, which is fundamental to all succeeding chapters. As its main point, however, the chapter explains the problem of control saturation in such a system for supercapacitors and how a voltage-balancing strategy can be adapted to deal with the problem. The result is essentially a proposal for a new voltage-balancing strategy, which was then tested in both simulation and experiments. Chapter 3 deals with supercapacitor characterization. It provides a comprehensive discussion of time- and frequency-domain characterization. The chapter ends with a new proposal for an online characterization method that can be used alongside system life optimization. The last chapter, Chapter 4, forms the heart of this thesis. The modular converter system for supercapacitors is demonstrated to work on two different applications: as an auxiliary supply in a trolleybus and as an integrated energy storage in a modular multilevel converter for grid frequency response. Simulation

results are shown for both applications and experimental for grid frequency response application. At the end, a general conclusion was written to tie up all the four chapters and provide a coherent overview of the contribution of this thesis. It also gives possible directions for future endeavors in this subject.

Chapter 1

Motivation and Context

The world celebrated on 12 December 2015 when 196 parties in the 21st session of the Conference of Parties (COP 21) in Paris agreed to a legally binding treaty on climate change. The treaty came to be known as the Paris Agreement and it came into force on 4 November 2016. Its main objective is to limit global warming to below 2 °C if not 1.5 °C compared to pre-industrial levels. The goal can be achieved if countries reach peak global greenhouse gas (GHG) emissions as soon as possible resulting in a climate-neutral world by the middle of the century. While a landmark treaty, the Paris Agreement entails wholesale economic and societal transformations. Each country has nationally determined contributions (NDCs) towards the goal of reducing its emissions. Though not mandatory, each country could also submit long-term low GHG emission development strategies (LT-LEDS) that could better frame the attainment of NDCs in the context of its own long-term development plans. In addition, the agreement also provided for a framework for financial, technical, and capacity building support to those countries who need it [2].

Despite the challenging politics and partisan divide surrounding the issue of climate change in some parts of the world, consensus is clear in the scientific community. It is unequivocal that human activities caused the warming of the planet, as said in the 2021 Working Group I contribution to the Sixth Assessment Report of the Intergovernmental Panel on Climate Change (IPCC). The IPCC is the United Nations body assessing the science of climate change. Human activities have increased observed GHG since around 1750 and this has resulted in global warming. Just the global surface temperature of the first two decades of the 21st century is 0.99 °C hotter than in 1850–1900. The report continues that the warming has resulted in extensive and rapid changes in the atmosphere, ocean, cryosphere, and biosphere. Precipitation has increased since 1950. Glaciers have been in retreat since the 1990s and the Arctic sea ice area has been decreasing since the 1980s. The upper global ocean has been warming since the 1970s. The increase in the global mean sea level has been accelerating since 1901. Land biospheres

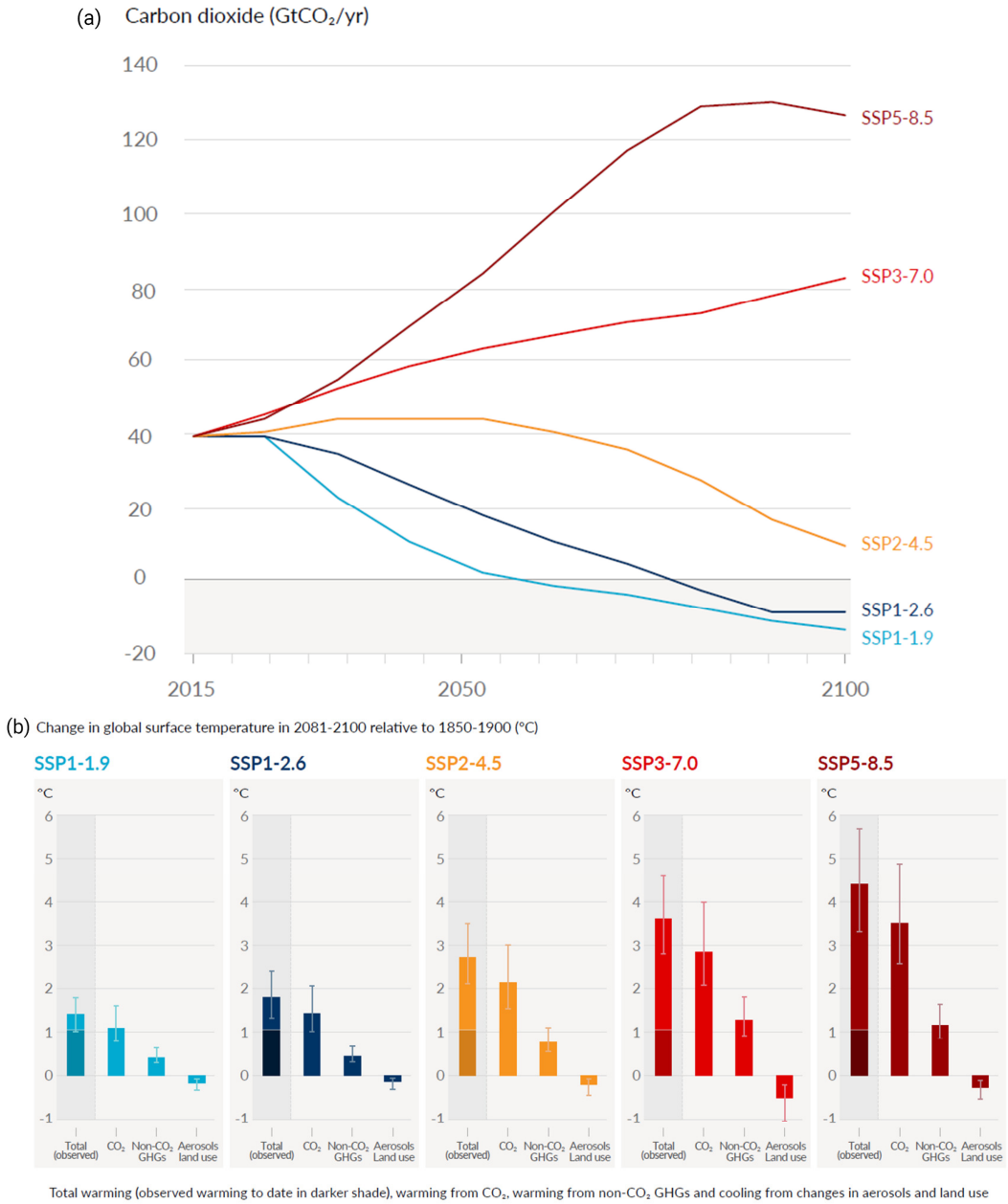

Fig. 1.1. (a) Future annual emmissions of CO_2 for five illustrative scenarios and (b) Contribution to global surface temperature increase from different emissions for the five scenarios [3]

have been changing since 1970. There is no question that climate change is human-induced and it is already affecting the weather and climate systems resulting in extremes such as heatwaves, heavy precipitation, droughts, and tropical cyclones [3].

To chart the possible courses through the century, the IPCC looked at five emissions scenarios, which were used to drive climate models and obtain projections for future climate systems. The five scenarios are: (i) SSP5-8.5 for very high GHG emissions where CO_2 emissions double from 2015 levels by 2050; (ii) SSP3-7.0 for high emissions where CO_2 emissions double from 2015 levels by 2100; (iii)

SSP2-4.5 for intermediate emissions where CO_2 emissions remain around 2015 levels by mid-century; (iv) SSP1-2.6 for low emissions where CO_2 emissions decline to net zero after 2050; and lastly, (v) SSP1-1.9 for very low emissions where CO_2 emissions decline to net zero around 2050. Projections of CO_2 emissions are shown in Fig. 1.1(a) for the five scenarios. On the other hand, Fig. 1.1(b) gives us the warming contribution of each scenario to the global surface temperature in 2081–2100 relative to 1850–1900. The effect of all emissions (GHG and aerosols) was considered in the total [3]. We can see right away that all scenarios will result in a temperature increase. Only the very low emissions scenario SSP1-1.9 will result in a range totally within the Paris Agreement goal of limiting temperature increase to within 2 °C, if not 1.5 °C. While the median of low emissions scenario SSP1-2.6 is within 2 °C, the range is not. This means that we have a very small margin to work with. The low (SSP1-2.6) to very high (SSP5-8.5) emissions scenarios are just out of the question if we are to definitively achieve the Paris Agreement objective. We must drastically reduce GHG emissions and target to be net zero around 2050.

How then do we go about drastically reducing GHG emissions? As the Paris Agreement itself recognizes through each country's LT-LEDS, economic development and climate change mitigation and adaptation are intertwined. To illustrate this, the 2022 working group III contribution to the sixth assessment report of the IPCC says that the course that each country takes with regard to its economy will invariably affect not only its GHG emissions but also the mitigation challenges and opportunities. Costs of low-emission technologies have continuously decreased since 2010 thanks to innovation policies that supported technology adoption. In just under two decades from 2010 to 2019, solar energy costs decreased by 85%, wind energy by 55%, and lithium-ion batteries by 85%. Deployments have also seen large gains with more than ten times for solar and more than a hundred times for electric vehicles. In some cases, maintaining emission-intensive systems may be more expensive than transitioning to low-emission systems. Electricity systems based predominantly on renewable energy sources are progressively being adopted. Operational, technological, economic, regulatory, and social challenges remain, but a number of solutions have also emerged. These include integrating systems, coupling sectors, energy storage, smart grids, demand-side management, and sustainable biofuels among others [51].

On top of the basic energy generation technologies, digital technologies in the form of sensors, Internet of Things, robotics, artificial intelligence, etc. can improve energy management and increase efficiency. This should further promote low-emission technology adoption while opening economic opportunities. All these recent advances have led to a more decentralized approach to decarbonization. It has been observed that the cost reductions and performance improvements have been more significant for modular small-scale technologies compared to large-scale ones. This more granular approach seems

to be the way to accelerated low-carbon transformation as it has been observed to lead to faster technology adoption, lower investment risk, and generally higher social returns. Broad-based participatory policies and good governance are key to support this approach in the transformation towards the goal of decarbonization [51].

In France, the president of the republic unveiled in October 2021 the 30-billion-euro "France 2030," a ten-point investment plan for the country to accomplish by 2030. The fourth objective calls on the country to "produce nearly 2 million electric and hybrid vehicles" and follows the third objective, which calls to "decarbonize our industry." These objectives are just two among six that has sustainability as the underlying concern out of the total ten objectives [52]. Related to the fourth goal and as part of the COVID-19 pandemic recovery plan for the automobile industry, France has been offering generous subsidies of up to EUR 7,000 for individuals and up to EUR 5,000 for corporations when they acquire electric or hybrid cars [53], [54]. Other subsidies have been announced and are already in the pipeline. The goal of course, is to incentivize consumers and facilitate societal transition to low-carbon transportation. In this regard, France is not alone. Other countries like the United Kingdom and Germany among others have similar programs, though France's subsidies remain among the more generous ones [55].

At the heart of electric and hybrid vehicles and of electrified mobility in general is energy storage. The past several years have seen an explosion in consumer-level electrified mobility and we have the development of power-dense energy storage as the enabling technology to thank for that [4]. Achieving France's fourth goal of producing nearly 2 million electric and hybrid vehicles in France 2030 thus entails investments in energy storage. We can see this in the recent announcement by Verkor, a French company founded in 2020 with the backing of major French and European business groups and governmental institutions. Verkor just announced that it has chosen the northern port city of Dunkirk in Hauts-de-France out of 40 candidates as the site of its first Gigafactory for the production of low-carbon battery cells. It will open in 2025 with an initial annual manufacturing capacity of 16 GWh [5]. This follows the trend in the steps of other companies like Sweden's Northvolt, which produced its first cell in 2021 in its Northvolt Ett Gigafactory. It has plans for another Gigafactory in Sweden to open in 2024 and a third one in Germany to open in 2025 [6]. Another company with plans to open a battery Gigafactory is Norway's FREYR, which plans to commence production in 2022 [7]. Globally, it was Tesla on its Nevada site in the United States that first opened a battery Gigafactory in 2016. It was also Tesla that first used the term for a manufacturing plant capable of GWh of battery production [8]. The term has since been adopted by other companies to describe similar facilities.

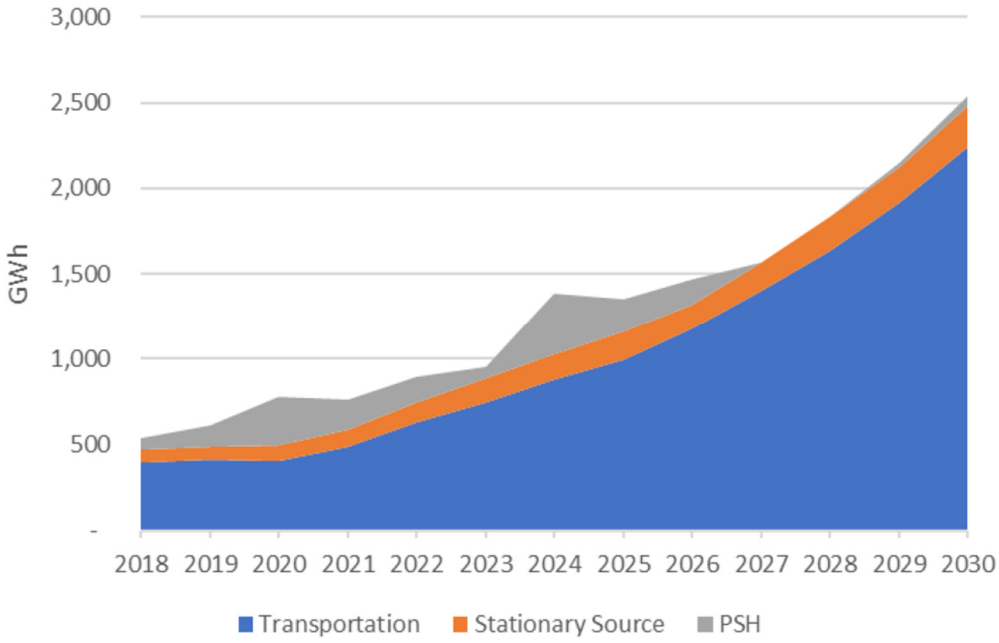

Fig. 1.2. The global energy storage market with projections up to 2030 (PSH stands for pumped-storage hydropower) [56]

Energy storage used to be called the bottleneck or the missing link in transitioning the power grid into renewable energy sources. However, recent advances and trends in the many different storage devices available have opened energy storage as a genuine source of opportunity. It has become a matter of looking for the technology that will be most cost-effective for a specific application. The global market for energy storage in GWh according to data compiled by the US Department of Energy is shown in Fig. 1.2. The total is disaggregated into three sectors: transportation, stationary, and pumped-storage hydropower (PSH). Under transportation can be found two further application subsectors for energy storage: (i) electric vehicles both in the form of battery-powered electric vehicles (xEVs) and fuel cell electric vehicles (FCEVs) and (ii) starting, lighting, and ignition (SLI). On the other hand, the stationary energy storage sector is mostly grid balancing services and industrial or commercial product or service resilience [56]. Current 2022 demand is projected to grow more than threefold by 2030. As is obvious from the figure, this growth will be driven by the transportation sector, specifically the adoption of electric vehicles. In fact, energy storage deployments for transportation use are up to ten times larger than both stationary and PSH.

A breakdown of energy storage deployments for the transportation sector can be seen in Fig. 1.3(a). The chart has also been further categorized into the two subsectors mentioned earlier: on-board mobility and SLI. The latter dominates from the early years between 2018 up to 2022. This is due to the fact that internal combustion engines use energy storage for SLI applications. Lead-acid batteries

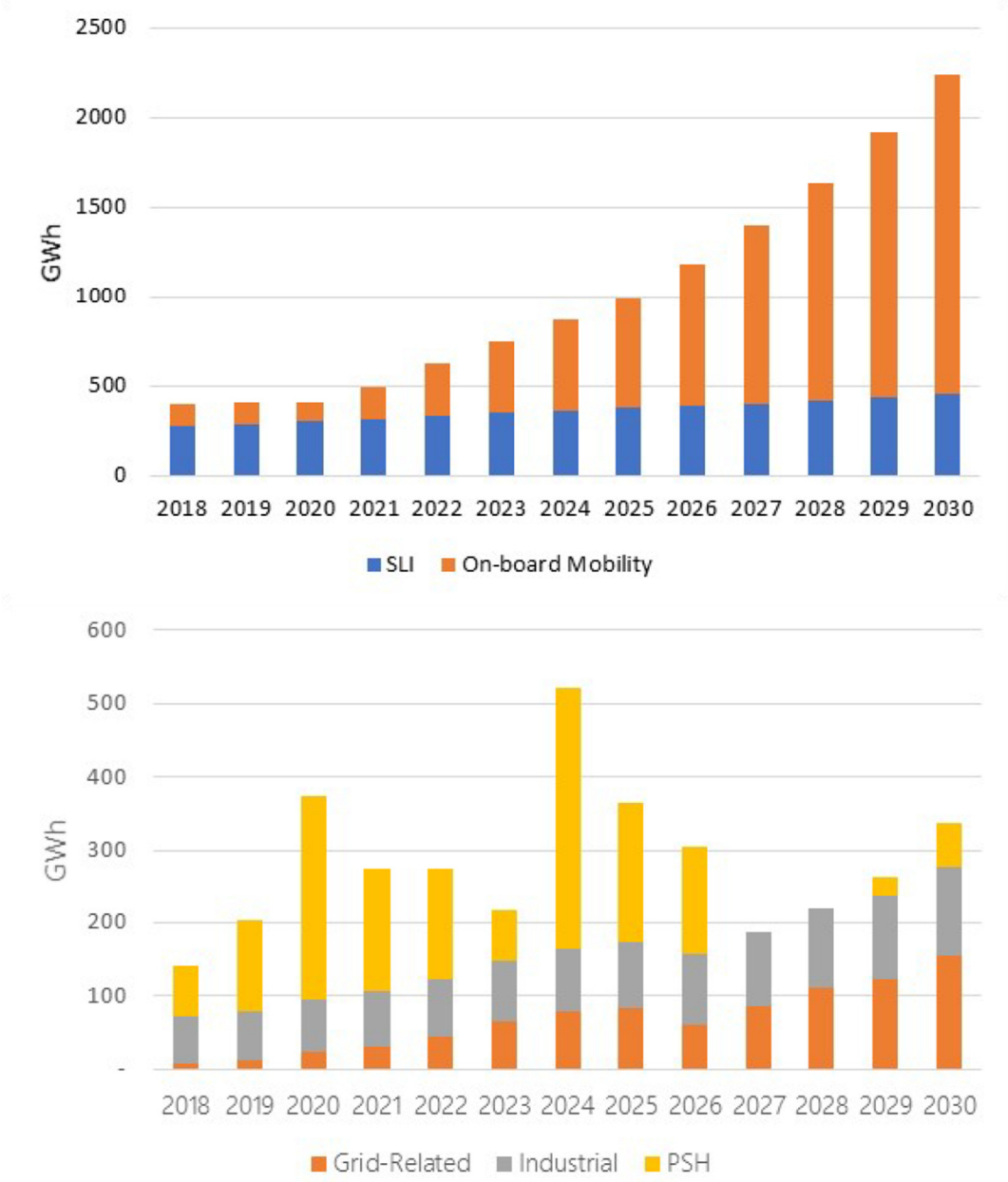

Fig. 1.3. Global annual energy storage deployment projections for: (a) Transportation and (b) Stationary sectors [56]

dominate this market. However, little growth is expected in this subsector up to 2030. Starting in 2022, on-board mobility where energy storage powers up vehicle propulsion as in xEVs and FCEVs, is expected to pick up and grow at an exponential rate. Batteries in xEVs are dominated by lithium-ion batteries though other chemistries are possible for hybrid vehicles, while FCEVs are powered by hydrogen stored in a tank and combined with a storage system for high power demands. The market for this subsector is projected to exceed that of the SLI subsector from 2023 onwards [56].

We then have in Fig. 1.3(b) the projections for the stationary market where figures for further subsectors are also shown. What is most striking is that the projected totals do not follow a pattern. The reason is that PSH, which generally are large single projects has long lead times. The total figure for PSH could thus have large variations year-to-year, which affect the totals for the whole of the stationary market. To see patterns, we have to turn our attention to the two other subsectors. Industrial energy storage applications currently dominate grid-related applications. The former includes energy storage for off-road motive applications (such as in forklifts) followed by uninterruptible power supply (UPS) and telecommunications applications. However, grid-related energy storage applications are expected to grow through the years and exceed industrial applications by 2030 [56].

It is clear from the preceding discussion and from Fig. 1.2 and Fig. 1.3 that both the energy storage demands for on-board mobility and grid-related services are sources of growth for the related energy storage technologies. For instance in 2019, the global lithium-ion battery market stood at USD 40 billion and is projected to grow 15.4% year-over-year from 2020 to 2026. The clear driver of this growth is the surge in demand for xEVs, though the COVID-19 pandemic is expected to have a dampening effect [57]. Another electrochemical energy storage device that is currently occupying a more niche market position is the supercapacitor. It has a smaller market of USD 2 billion in 2020, though its growth is projected to be almost as robust as lithium-ion battery's at 15% year-over-year from 2021 to 2027. For supercapacitors, deployments of industrial robots and automation in manufacturing are expected to steer the market towards expansion. In particular, supercapacitors, which have fast charging and longer lifetimes are used for example in industrial robots and in automated guided vehicles (AGVs) or autonomous mobile robots (AMRs). AGVs or AMRs are used for a similar purpose as the off-road motive applications previously mentioned with regard to industrial energy storage. Supercapacitors are also usually found as integral components of backup power supplies, which together with industrial applications covers 65% of the total market. The automotive and transportation sectors account for the remaining 35%. Supercapacitors find application in these sectors in increased adoption of regenerative breaking. Besides these two market segments, supercapacitors are also poised for growth in consumer electronics and in renewable power generation, which need fast charging and high energy storage capacity [58].

Analysis and comparison between batteries and supercapacitors are usually made to decide which one to use in a storage application. Compared to supercapacitors, batteries can store 30 times more charge per unit mass. On the other hand, supercapacitors can deliver hundreds of times more power per unit mass relative to batteries because charge is stored by surface adsorption on the electrode material. Batteries are thus considered energy-dense devices, while supercapacitors are power-dense. This is also reflected in terms of prices where batteries are up to seven times more expensive per kW of

power and supercapacitors are up to four times more expensive per kWh of energy. This means that the choice between batteries and supercapacitors is usually dictated by whether the application is energy- or power-heavy. The charge mechanism of supercapacitors allows them to be cycled several hundred times more than batteries, which have volumes that change with the redox reactions limiting the possible number of cycles. Hybrid devices that combine the best features of batteries and supercapacitors are an active area of research [59]. In addition, hybrid systems that have batteries and supercapacitors as discrete components interfaced by power electronics already exist in various applications although they remain to be a fruitful domain of research inquiry [60].

Cost effectiveness as a concept can be seen through different points of view. For example, techno-economic assessments will look at a technology's performance from different metrics: capital cost, life cycle cost, and levelized cost of energy (LCOE). Life cycle cost and LCOE are interesting measures because they consider costs over a technology's lifetime from cradle to grave [9]. This means that the longer a technology is usable, the lower the LCOE. From the point of view of investors, life cycle cost and LCOE are important metrics when comparing different energy storage technologies [35]. Indeed, improving energy storage reliability and prolonging lifetime has become a hot area of research besides being needed in lowering the investment risks for technology providers and adopters in the form of product/service warranties and insurance premiums [51]. Research and development here cover the whole of an energy storage technology's vertical product structure from the bottom at the materials to device levels up to the top at the integrated systems, product, and service levels [35].

As life cycle costs and LCOE are considered over the whole life of a technology, the importance of lifetime cannot be underscored enough. Great engineering research effort is currently focused on improving reliability and prolonging lifetime. In the case of energy storage technologies, recent projects have tried to understand and quantify the root causes for loss of reliability. This has led to the development of aging models that can be used to simulate the operation of energy storage systems over their whole lifetimes. This is useful not only in delving deeper into understanding aging mechanisms, but more so in doing simulation experiments that would otherwise be impossible to complete within reasonable time if done in real life. Time in simulation experiments is accelerated compared to real time making possible simulation over the duration of an energy storage system lifetime. Real-life experiments can thus be optimized with help from simulation experiments. For example, such simulation experiments help in finding system and control configurations that can extend energy storage lifetime. Results can then be used to optimize real-life experiments. This has become a modus operandi in engineering research and the effort to prolong lifetime has certainly benefited. Research projects now include aging experiments and models to extend the energy storage system life by reducing the effect of various stressors [35].

This thesis approaches the problem of extending energy storage lifetime from a system perspective. Inhomogeneities caused both by the initial characteristics and the actual operation of energy storage cells result in unequal individual cell lifetimes. For the whole system of energy storage cells though, the system end of life is commonly considered as the time when the weakest cell fails or reaches its own end of life. The weakest cell thus dictates the lifetime of the whole system. It is obvious that the system lifetime is not optimized because healthier cells will not have gotten to their own end of life by the time the system lifetime is over. Our approach in this thesis is similar to previous studies in the sense that the effect of aging stressors will also be reduced. However, novel control methods will be applied such that the aging stress on the weakest cells will be reduced and whatever load was removed from them will be shouldered by healthier cells. It will be shown in the discussions in Chapter 4 that extending the system lifetime this way has the effect of balancing the cells' lifetimes and extending the lifetime of the whole system.

The thesis approaches the problem of energy storage system life optimization or extension through the application of novel balancing strategies especially designed for interfacing modular power converters. The partition of the common single interfacing converter into many modular ones opened the possibility of designing and applying a system health optimization strategy that takes into account the reliability or health of individual energy storage cells in the assignment of load. As already mentioned, this results in balancing cells according to their individual reliability or health. In essence, the energy storage system life optimization is practically the same as balancing energy storage state of health (SoH). This is a significant contribution in this domain where the standard is still balancing energy storage state of charge (SoC). It should have an effect on the important commercial metrics like life cycle costs and LCOE where cost effectiveness over the whole system life is considered. As the novel lifetime optimization method works in tandem with SoC balancing to achieve a balanced system SoH, the next chapter, Chapter 2, will present a new SoC-balancing strategy for supercapacitors that can provide for control saturation in the interfacing modular converter system.

Chapter 2

Balancing Supercapacitor Voltages

2.1 Introduction

Even though supercapacitors have high power densities, their low operating voltages are limited for use in most applications. Thus, cells are connected in series, in parallel, and/or in combination to reach application requirements [10]. Since supercapacitor parameters are never fully uniform even with today's advanced manufacturing processes, the choice of connection limits the electrical behavior of the cells. For example, cells connected in series share the same current and cells in parallel have the same voltage. The initial imbalance then exacerbates during operation because of the uneven aging of the cells [11]–[13]. Thus, there is a need for a system that balances the cell voltages to ensure safe operation and a prolonged lifetime for the supercapacitors [10], [11], [14]. This requires energy storage management systems that also monitor voltages, currents, and temperatures, and that interface with other devices [10], [15].

In the literature, there are two types of balancing circuits: passive (or dissipative) and active (or redistributive). In passive balancing, the excess charge in the cells is dissipated through resistors. It is the simplest and cheapest strategy to implement. On the other hand, active balancing redistributes charge from overcharged to undercharged cells, which is more efficient. Although costs depend a lot on the chosen architecture, this strategy is commonly expensive to implement because of additional components and more complicated control systems [13], [16]–[18]. Recently, a third approach in balancing emerged. It capitalizes on the energy management systems of modular DC-DC power converters that interface the energy storage devices with the rest of the system. Like active balancing, it is nondissipative, but unlike the first two types, there is no need for separate balancing circuits connected in parallel because, if there is one modular converter per cell, balancing can be integrated in the same algorithms that control the output voltages of the connected converters. DC bus voltage regulation and

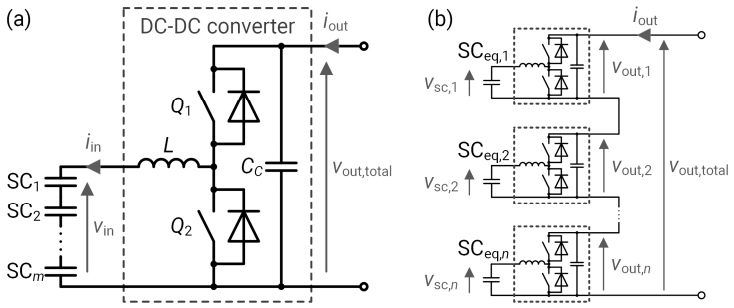

Fig. 2.1. Supercapacitors power conversion systems: (a) A single nonisolated bidirectional DC-DC converter interfacing a supercapacitor stack at the low side ($v_{\text{out,total}} \geq v_{\text{in}}$) and (b) Modular power converters interfacing supercapacitor groupings

balancing without the extra circuitry or charge redistribution are thus possible in an efficient, modular way [19]–[26].

The nonisolated bidirectional DC-DC converter in Fig. 2.1(a), whose output voltage $v_{\text{out,total}} \geq v_{\text{in}}$ (its input voltage), is commonly used to interface supercapacitors with different applications [30], [61]–[64]. It is in boost mode when the supercapacitors are discharging and in buck mode when the supercapacitors are charging. In case of a relatively high-voltage bus, low-voltage supercapacitor cells are placed in series at the low side of the converter, while the high side is directly connected to the DC bus [30]. Cascading these converters as in Fig. 2.1(b) has recently been employed to meet the DC bus voltage requirements.

The half-bridge modular architecture of Fig. 2.1(b) was chosen in consideration of two related previous studies: the Hybus and SuperGrid applications [27]–[29]. In the first study, the new modular architecture in Fig. 2.1(b) allows a new degree of flexibility in terms of control that is beneficial for managing electrothermal imbalances [27]. On the other hand, the second study is about the integration of supercapacitors into modular multilevel converters (MMC), which is composed of hundreds of submodules [28]. The architecture in Fig. 2.1(b) is proposed as an interface between supercapacitors and the submodule capacitors of the MMC [29]. The architecture offers modularity that provides increased overall reliability and flexibility to the system [65].

When charging unbalanced supercapacitors to reach the same voltage (balancing) using the circuit of Fig. 2.1(b), the unique problem of saturation in the control of a modular converter j through the duty ratio $D_j = v_{\text{sc},j}/v_{\text{out},j}$ (in buck mode or $D_j = 1 - v_{\text{sc},j}/v_{\text{out},j}$ in boost mode) can nonetheless arise on account of the possible overlap of the voltage ranges between the supercapacitor side and the high side of the converters. This occurs because a low conversion ratio $M_j(D_j) = D_j$ for the modular

converters in buck mode (or a high $M_j(D_j) = \frac{1}{1-D_j}$ in boost mode) in Fig. 2.1(b) is impractical, which would otherwise have provided the voltage margin necessary to skirt the problem [66]. This will be shown in Subsection 2.4.2 to be due to the D_j range limiting the acceptable converter efficiency. In essence, control saturation happens during charging when the balancing goal cannot be reached because one (or more) of the modular converter duty ratios has reached the limits of the possible range. It will be explained in detail in Section 2.3. Supercapacitor characteristics itself is another factor in the problem. Unlike batteries, which have voltage curves with a region comparatively flat relative to the state of charge (SoC), supercapacitor voltage varies from 0 to $V_{\max}$ relative to its state of energy. This adds to the probability of overlap because the voltage affects the conversion ratio by the formula definition.

A survey of the literature shows a great number of different SoC- or voltage-balancing strategies, mostly for batteries [13], [16]–[18], [20], [21], [24], [30]. While they can also be used for supercapacitors, unfortunately, they are slow and could take anywhere from a couple to hundreds of minutes to achieve equalization. Considering fast balancing, no study has yet tackled the previously described problem of control saturation that result from the converter architecture and the supercapacitor characteristics. We address this inadequacy in the literature through a method of balancing supercapacitor voltages in modular power electronic converter circuits within, if possible, a single charging period. We propose to use the strategy here in applications where supercapacitors are needed as power buffer like in electric vehicles or in grid-integrated energy storage systems [27], [30], [61]–[64]. Only occasional voltage balancing would then be needed and the strategy will keep the balanced voltages once reached. This is possible because voltage imbalances would be minimal if cell characteristics were ensured to be reasonably uniform from the start [67].

The chapter is organized in six sections. The systems involved will be described in the next section (2.2). The voltage-balancing strategy, the problem of saturation in the control of modular power converters, and the control saturation-adapted strategy will be explicated in Section 2.3. Then, the system setup and the case studies that demonstrate the operation of the strategy will be discussed in Sections 2.4 and 2.5. The last section (2.6) concludes the paper. Major parts of this chapter have been reorganized, transformed and published as a journal article [68].

2.2 Systems Description

In this section, we first describe in detail the circuits, the control systems, and the models involved before presenting the problem of saturation of the control of modular power converters connected to supercapacitors in the next section.

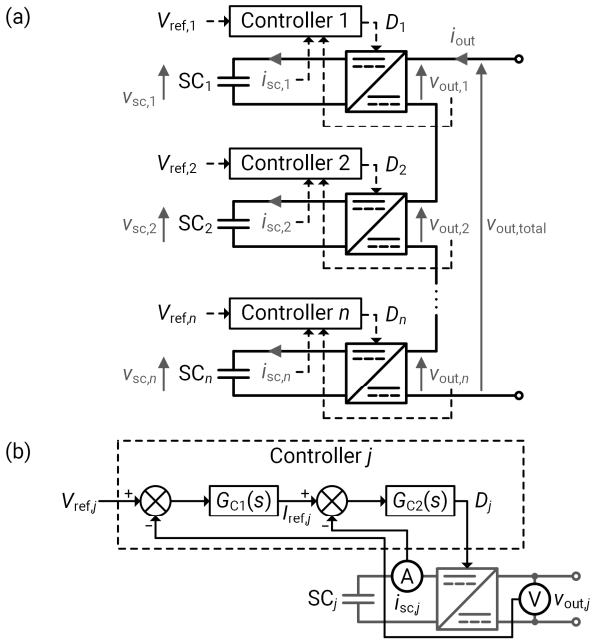

Fig. 2.2. The control system to charge/discharge supercapacitors using modular power converters: (a) System-level control and (b) Module-level control

2.2.1 Control Systems

Fig. 2.2(a) shows the control architecture at the system level. Modular power converters are cascaded such that the total converter output voltage $\sum_{j=1}^{n} v_{\text{out},j} = v_{\text{out,total}}$ is regulated, where $j \in (1,2,\dots,n)$ is the index and n is the total number of modular converters. Each converter has its own controller that has $V_{\text{ref},j}$ as reference voltage and $v_{\text{out},j}$ as the output controlled by a pulse-width modulated (PWM) control signal with duty ratio $D_j \in [0,1]$.

The architecture of one controller is shown in detail in Fig. 2.2(b). It is a conventional two-loop control system that responds to disturbances and corrects nonlinearities better than a single-loop system. The slower outer loop in Fig. 2.2(b) with a settling time $T_{\text{s}} = 5$ ms is for controlling the converter output voltage $v_{\text{out},j}$, (which can be considered to be the C_C capacitor voltage in the single converter of Fig. 2.1(a)), while the faster inner loop in Fig. 2.2(b) with a settling time $T_{\text{s}} = 1$ ms is for controlling the supercapacitor current $i_{\text{sc},j}$, which can be considered to be the inductor current (also the converter input current i_{in}) in Fig. 2.1(a). In the outer loop, the error between $V_{\text{ref},j}$ and the measured feedback $v_{\text{out},j}$ feeds into the first proportional-plus-integral (PI) controller $G_{\text{C1}}(s)$, which outputs the reference value for the inductor current $I_{\text{ref},j}$. In the inner loop, the error between this $I_{\text{ref},j}$ and the measured

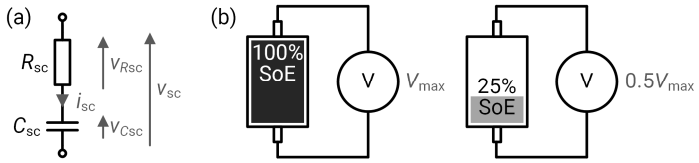

Fig. 2.3. Balancing the voltages of three supercapacitors to reach V_{max}; SC_1 must be charged with the energy ΔE_1

supercapacitor current feedback $i_{sc,j}$ feeds into the second PI controller $G_{C2}(s)$, which then outputs the duty ratio of the PWM control signal to the converter.

If the supercapacitor voltages $v_{sc,j}$ are balanced, $V_{ref,j} = V_{ref,total}/n$, where $V_{ref,total}$ is the sum of all reference voltages and can be considered as the bus voltage. Otherwise, a difference between the reference voltages can be used to control the system in order to balance the supercapacitor voltages. A strategy exactly doing this will be presented in the next section.

2.2.2 Supercapacitors

Supercapacitors can be modeled in several ways. The simplest is the *RC* model shown in Fig. 2.3(a), which is composed of a constant capacitance C_{sc} that serves as the energy storage element in series with a resistance R_{sc} that represents the equivalent series resistance (ESR) of supercapacitors. More complex accurate models build on this one. In this work, however, we are mainly concerned with the steady state behavior of supercapacitors. Thus, a macroscopic model such as the *RC* model suffices [69]–[71].

As mentioned, energy is stored in the capacitor component of the supercapacitor *RC* model. As such, it is given by:

$$E = \frac{1}{2} C_{sc} v_{sc}^2 \tag{2.1}$$

where E is the energy (J) and v_{sc} is the supercapacitor voltage. Strictly speaking, the latter should be the open-circuit voltage. However, throughout this chapter, we can just approximate it to be just the supercapacitor voltage because $|v_{Rsc}| \ll |v_{Csc}|$, where v_{Rsc} is the voltage across R_{sc} and v_{Csc} is the voltage across C_{sc} in Fig. 2.3(a). The state of energy (SoE) then, relative to a supercapacitor maximum rated voltage V_{max}, is [72], [73]:

$$SoE = \left(\frac{v_{sc}}{V_{max}}\right)^2 \times 100 \tag{2.2}$$

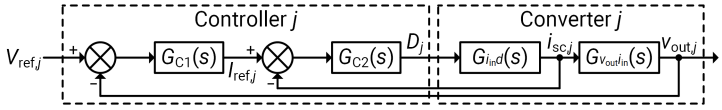

Fig. 2.4. Two-loop control system with the modular converter represented by its transfer functions

Eq. (2.2) shows that the SoE range from 0% to 100% is a square function of the supercapacitor voltage range from 0 V up to $V_{\max}$. The operational SoE range, shown in Fig. 2.3(b), is usually limited from 25% to 100% to have a usable voltage range between half the rated voltage ($V_{\max}/2$) up to $V_{\max}$. This allows use of 75% of stored energy [74].

2.2.3 Modular Power Converters

In order to use the two-loop control system described in subsection 2.2.1, the open-loop control-to-output transfer function $G_{v_{\text{out}}d}(s)$ representing the converter must be decomposed into two transfer functions: the control-to-input current transfer function $G_{i_{\text{in}}d}(s)$ and the input current-to-output voltage transfer function $G_{v_{\text{out}}i_{\text{in}}}(s)$, as shown in Fig. 2.4. To accomplish this, we start with the modeling of the bidirectional DC-DC converter in Fig. 2.1(a). The state-space averaged model unified for both the buck and boost modes of the converter was derived considering the conduction losses in the form of the parasitic resistances (ESR) of the components and the synchronous or complementary control of switches Q_1 and Q_2. The first state ($Q_1 = 1$ and $Q_2 = 0$) is on during the first Dt_s interval within the switching period t_s (with D the duty ratio), while the second state ($Q_1 = 0$ and $Q_2 = 1$) is on for the remaining $(1 - D)t_s$ interval. Given an initial conditions vector $\mathbf{x}_0$, the converter is then represented by the state-space averaged model for $t \geq t_0$ as:

$$\begin{aligned} \dot{\mathbf{x}} &= \mathbf{A}\mathbf{x} + \mathbf{B}\mathbf{u} \\ \mathbf{y} &= \mathbf{C}\mathbf{x} + \mathbf{E}\mathbf{u} \end{aligned} \tag{2.3}$$

where

$$\begin{aligned} \mathbf{x} &= \begin{bmatrix} i_{\text{in}} \\ v_{Cc} \end{bmatrix}, \quad \dot{\mathbf{x}} = \begin{bmatrix} \dfrac{\mathrm{d}i_{\text{in}}}{\mathrm{d}t} \\ \dfrac{\mathrm{d}v_{Cc}}{\mathrm{d}t} \end{bmatrix} \\ \mathbf{y} &= \begin{bmatrix} i_{\text{in}} \\ v_{\text{in}} \\ v_{\text{out}} \end{bmatrix}, \quad \mathbf{u} = \begin{bmatrix} v_{C\text{sc}} \\ i_{\text{out}} \end{bmatrix} \end{aligned} \tag{2.4}$$

and

Table 2.1. Modular power converter specifications of the simulation setup

Parameter	Variable	Value	Unit
Switching frequency	f_s	10	kHz
System output current	$i_{\text{out,max}}$	±143	A
Test system output current	i_{out}	±50	A
Converter nominal output voltage	v_{out}	35	V
Converter input voltage range	v_{in}	16.2–32.4	V
Converter inductance	L	16	µH
Converter inductor ESR	R_L	0.65	mΩ
Converter capacitance	C_C	16	mF
Converter capacitor ESR	R_C	10	mΩ
MOSFET on resistance	$R_{\text{DS(on)}}$	3.9	mΩ
Control strategy time step	Δt	0.2	s

$$
\begin{aligned}
\mathbf{A} &= \begin{bmatrix} -\dfrac{R_{\text{sc}} + R_L + R_{\text{DS(on)}} + R_C D}{L} & \dfrac{D}{L} \\ -\dfrac{D}{C_C} & 0 \end{bmatrix} \\
\mathbf{B} &= \begin{bmatrix} -\dfrac{1}{L} & \dfrac{R_C D}{L} \\ 0 & \dfrac{1}{C_C} \end{bmatrix} \\
\mathbf{C} &= \begin{bmatrix} 1 & 0 \\ R_{\text{sc}} & 0 \\ R_C D & 1 \end{bmatrix} \\
\mathbf{E} &= \begin{bmatrix} 0 & 0 \\ 1 & 0 \\ 0 & -R_C \end{bmatrix}
\end{aligned}
\tag{2.5}
$$

Vectors **x**, $\dot{\mathbf{x}}$, **y**, and **u** are the state, derivative of the state, output, and input vectors, respectively, while matrices **A**, **B**, **C**, and **E** are the system, input, output, and feedforward matrices, respectively, averaged over the switching period. System and component parameter values relevant in the model follow from that and can be seen in Table 2.1. In addition, v_{Cc} is the voltage of the converter capacitance. The sizing of the Hybus application was adopted throughout this chapter. More details on the modeling steps can be found in Appendix A.

We can obtain the desired transfer functions by next deriving the linearized small-signal model of the state-space averaged model in (2.3). In such an analysis, we assume that each quantity has a nominal value and a small time-varying perturbation about that value. The derivative of the state vector then becomes $\dot{\mathbf{x}} = \dot{\mathbf{X}} + \hat{\dot{\mathbf{x}}}$, the state vector $\mathbf{x} = \mathbf{X} + \hat{\mathbf{x}}$, the output vector $\mathbf{y} = \mathbf{Y} + \hat{\mathbf{y}}$, the input vector $\mathbf{u} = \mathbf{U} + \hat{\mathbf{u}}$, and the duty ratio $d = D + \hat{d}$, with the uppercase variables representing the nominal values and the lowercase variables with the hat representing the small time-varying perturbations. It is basically a

method of linearizing an otherwise nonlinear system (i.e., the state-space averaged model) [75]. Without going into the details of the derivation, the small-signal model based on the averaged model of the converter is:

$$\begin{aligned}\dot{\hat{\mathbf{x}}} &= \mathbf{A}\hat{\mathbf{x}} + \mathbf{B}\hat{\mathbf{u}} + [(\mathbf{A}_1 - \mathbf{A}_2)\mathbf{X} + (\mathbf{B}_1 - \mathbf{B}_2)\mathbf{U}]\hat{d} \\ \mathbf{y} &= \mathbf{C}\hat{\mathbf{x}} + \mathbf{E}\hat{\mathbf{u}} + [(\mathbf{C}_1 - \mathbf{C}_2)\mathbf{X} + (\mathbf{E}_1 - \mathbf{E}_2)\mathbf{U}]\hat{d}\end{aligned} \tag{2.6}$$

where the subscripts of the system, input, output, and feedforward matrices refer to the state (e.g., $\mathbf{A}_1$ is the system matrix of the first state). Now linear, the small-signal model can be expressed in the Laplace form as:

$$\begin{aligned}\frac{\hat{\mathbf{x}}(s)}{\hat{d}(s)} &= (s\mathbf{I} - \mathbf{A})^{-1}[(\mathbf{A}_1 - \mathbf{A}_2)\mathbf{X} + (\mathbf{B}_1 - \mathbf{B}_2)\mathbf{U}] \\ \frac{\hat{\mathbf{y}}(s)}{\hat{d}(s)} &= \mathbf{C}(s\mathbf{I} - \mathbf{A})^{-1}[(\mathbf{A}_1 - \mathbf{A}_2)\mathbf{X} + (\mathbf{B}_1 - \mathbf{B}_2)\mathbf{U}] + [(\mathbf{C}_1 - \mathbf{C}_2)\mathbf{X} + (\mathbf{E}_1 - \mathbf{E}_2)\mathbf{U}]\end{aligned} \tag{2.7}$$

The resulting vector $\hat{\mathbf{y}}(s)/\hat{d}(s)$ already contains as its first element the control-to-input current transfer function $G_{i_{\text{in}}d}(s)$. To obtain the input current-to-output voltage transfer function $G_{v_{\text{out}}i_{\text{in}}}(s)$, the control-to-output transfer function $G_{v_{\text{out}}d}(s)$, which is the third element of $\hat{\mathbf{y}}(s)/\hat{d}(s)$, can be multiplied with the inverse of $G_{i_{\text{in}}d}(s)$. The desired transfer functions then are:

$$\begin{aligned}G_{i_{\text{in}}d}(s) &= \frac{\widehat{i_{\text{in}}}(s)}{\hat{d}(s)} = \frac{C_C V_{\text{out}} s - I_{\text{out}}}{LC_C s^2 + D^2} \\ G_{v_{\text{out}}i_{\text{in}}}(s) &= \frac{\widehat{v_{\text{out}}}(s)}{\widehat{i_{\text{in}}}(s)} = \frac{I_{\text{in}} L s + D V_{\text{out}}}{-V_{\text{out}} C_C s + D I_{\text{in}}}\end{aligned} \tag{2.8}$$

Note that the lossless converter model was used in the derivation of (2.8) to simplify the design of controllers $G_{\text{C2}}(s)$ and $G_{\text{C1}}(s)$ following the mentioned outer and inner loop settling times of 5 and 1 ms, respectively. In addition, I_{in}, I_{out}, and V_{out} are the nominal values of the corresponding variables. More details on the modeling steps can be found in Appendix A.

Steady-state converter characteristics can also be obtained from the unified state-space averaged model in (2.3). For example, the supercapacitor current at steady state can be represented as [76]:

$$i_{\text{in}} = \frac{i_{\text{out}}}{D} \tag{2.9}$$

On the other hand, the steady-state converter output voltage can be formulated as:

$$v_{\text{out}} = \frac{v_{\text{in}}}{D} + i_{\text{out}}\left[\frac{R_L + R_{\text{DS(on)}} + R_C D(1 - D)}{D^2}\right] \tag{2.10}$$

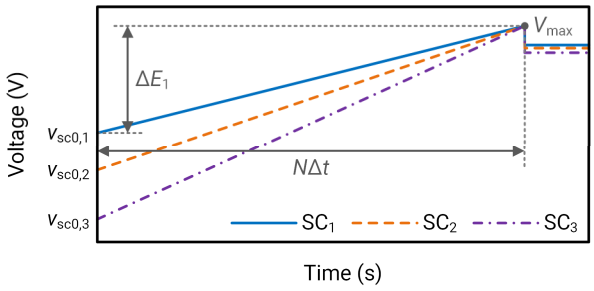

Fig. 2.5. Balancing the voltages of three supercapacitors to reach V_{max}; SC_1 must be charged with the energy ΔE_1 [68] © 2022 IEEE

This last expression shows the effects of the parasitic resistances. In the ideal scenario (lossless) without them, v_{out} can be reduced into just the first term of (2.10). Thus, given values for v_{in} and v_{out}, the duty cycle can be approximated as:

$$D \approx \frac{v_{in}}{v_{out}} \tag{2.11}$$

2.3 Voltage-Balancing and Control Saturation

In this section, we will first develop, for the modular power converters (cf. Fig. 2.2(a)), an energy-based strategy for balancing supercapacitor voltages and then proceed to describe how the problem of control saturation arises out of the system architecture and supercapacitor characteristics. Finally, we will advance modifications to the strategy in order to adapt it to the problem.

2.3.1 Voltage-Balancing Strategy

The important goals for the balancing strategy are (i) to charge the supercapacitors until they reach the maximum rated voltage V_{max}, and (ii) to reach this full charge at the same time. These are illustrated in Fig. 2.5, where there are three supercapacitor voltages that need to be balanced. For a supercapacitor j to reach V_{max} at the end, it must be charged with the amount of energy:

$$\Delta E_j(t) = \frac{1}{2} C_{sc,j}\left[V_{max}^2 - v_{sc,j}^2(t)\right] \tag{2.12}$$

The average power of supercapacitor SC_j during the charging period $N\Delta t$, where N is the number of time steps, is:

$$P_j = \frac{\Delta E_j}{N\Delta t} \tag{2.13}$$

Bearing in mind the second objective for the balancing strategies, $N\Delta t$ should be the same for all supercapacitors. We can thus solve for $N\Delta t$ in (2.13) and the resulting ratio of energy and power should be the same for all n supercapacitors:

$$\frac{\Delta E_j}{P_j} = \frac{\Delta E_{j+1}}{P_{j+1}} = \cdots = \frac{\Delta E_n}{P_n} \tag{2.14}$$

In Fig. 2.2(a), we can see that the converters have the same output current i_{out}. We assume ideal converters, which means that the ratio of energy and output voltage should also be the same for all supercapacitors:

$$\frac{\Delta E_j}{v_{\text{out},j}} = \frac{\Delta E_{j+1}}{v_{\text{out},j+1}} = \cdots = \frac{\Delta E_n}{v_{\text{out},n}} \tag{2.15}$$

We would like the strategy to have the form where the power of converter j is shown as a share of the voltage regulation at the output. To do this, we define and generalize a weighting factor w_j as the ratio of $\Delta E_j(t)$ and the total charging energy:

$$w_j(t) = \frac{\Delta E_j(t)}{\sum_{m=1}^{n} \Delta E_m(t)} \tag{2.16}$$

Multiplying (2.15) by the reciprocal of the total charging energy, we obtain:

$$\frac{w_j}{v_{\text{out},j}} = \frac{w_{j+1}}{v_{\text{out},j+1}} = \cdots = \frac{w_n}{v_{\text{out},n}} \tag{2.17}$$

To express $v_{\text{out},j}$ in terms of the weighting factor and the total output voltage $v_{\text{out,total}} = \sum_{j=1}^{n} v_{\text{out},j}$, by definition, we note that:

$$v_{\text{out,total}} = \frac{\sum_{j=1}^{n} v_{\text{out},j}}{\sum_{j=1}^{n} w_j} \tag{2.18}$$

where the denominator is just equal to unity. We can solve for $v_{\text{out},j+1}$, $v_{\text{out},j+2}$, …, $v_{\text{out},n}$ in terms of $v_{\text{out},j}$ in (2.17) and substitute them into (2.18). Doing that, rearranging, and considering that $V_{\text{ref},j} = v_{\text{out},j}$ at steady state:

$$V_{\text{ref},j}(t) = V_{\text{ref,total}} w_j(t) \tag{2.19}$$

With (2.12), (2.16), and (2.19), we have the equations needed to control the modular power converters and balance supercapacitor voltages. We refer to their use as the normal mode because they have not been adapted yet to the problem of control saturation, which will be done in the next subsection. The steps in the flowchart in Fig. 2.6 are used in applying the equations:

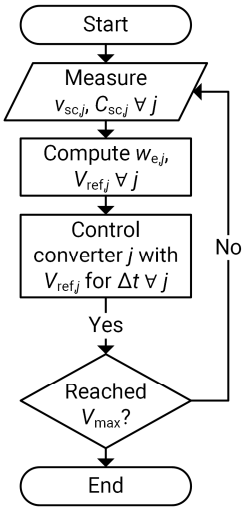

Fig. 2.6. Flowchart of the voltage-balancing strategy algorithm (normal mode)

1. At the beginning of the time step Δt, measure the voltage of each supercapacitor. If the application is for long-term use, then there is also a need for online estimation of the capacitance of each supercapacitor [40].

2. Compute the weighting factor for each of the supercapacitors using (2.12) and (2.16).

3. Compute the reference voltage for each of the converters using (2.19). Control the converters using the reference voltages for the remainder of Δt.

4. Repeat steps 1–3 for the next time steps until the supercapacitors reach V_{max}.

To illustrate the strategy, we have in Fig. 2.7 an idealized example. Following the algorithm in Fig. 2.6, we obtain values of converter output voltages that total $V_{ref,total}$. Because SC_1 has the highest initial voltage, its converter should receive the lowest power share through the lowest converter output voltage based on the strategy. On the other hand, the converse is true for SC_3, which has the lowest initial voltage and thus the highest power share.

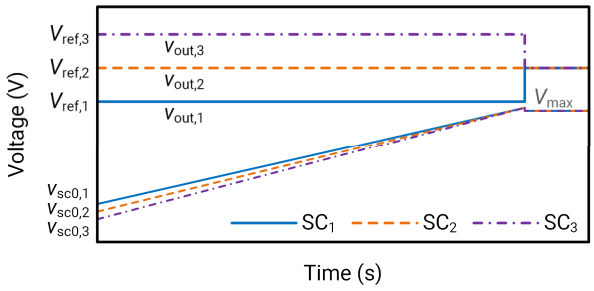

Fig. 2.7. The converter output voltage $v_{\text{out},j}$ must correspond to the initial supercapacitor voltage $v_{\text{sc},j}$ based on ΔE_j to provide balancing (to scale)

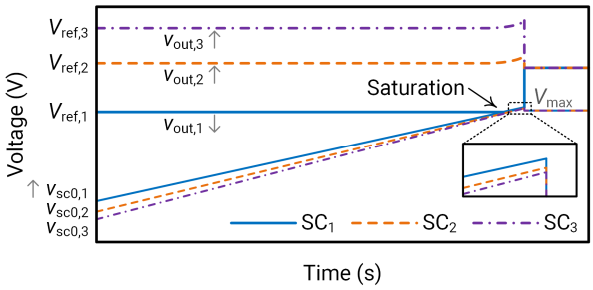

Fig. 2.8. A small increase in $v_{\text{sc0,1}}$ results in saturation in the control of converter 1 before reaching V_{max} (to scale)

2.3.2 Control Saturation

The control of a modular power converter in Fig. 2.2 is said to be saturated when the duty ratio limits are already reached, but the voltage-balancing strategy still demands a value even beyond them. Fig. 2.7 illustrates the idealized application of the strategy. As the voltages for converter 1 show, the modular converter system is especially vulnerable to control saturation during balancing. Say that $v_{\text{sc0,1}}$ is higher than in the figure. Because $-v_{\text{sc},j}^2$ is proportional to ΔE_j based on (2.12), while $v_{\text{out},j}$ is proportional to ΔE_j based on (2.15), $v_{\text{out,1}}$ would have to be even lower than in the figure, increasing the chances of the case $v_{\text{out,1}} = v_{\text{sc,1}}$ happening before $v_{\text{sc,1}}$ reaches V_{max} much more likely. In general, this means that the worse the supercapacitor voltage imbalance is, the greater the probability of control saturation.

As previously mentioned, control saturation would not be a problem if there is enough voltage margin in the system, i.e., the voltage ranges of the input and output sides do not coincide. However, the architecture constrains the system because (i) the converter structure discounts a low conversion ratio $M_j(D_j)$ in buck mode because efficiency suffers with low $M_j(D_j)$ (or a low-efficiency high $M_j(D_j)$

in the boost mode), as will be shown in Subsection 2.4.2; (ii) using the full SoE range means an almost full use of the D_j range, again underscoring the need for a high $M_j(D_j)$ in the buck mode or low $M_j(D_j)$ in the boost mode; and (iii) worse imbalance entails further deviation from the nominal power share $V_{\text{ref,total}}/n$. Control saturation is thus almost inevitable in achieving the twin goals of charging and balancing supercapacitors.

So what happens when the control of a converter is saturated? Fig. 2.8 illustrates the same case as in Fig. 2.7, but with a slightly higher value of $v_{\text{sc0,1}}$. We can observe that due to this, the reference voltage for converter 1 is lower resulting in control saturation for converter 1 and in higher reference voltages for the remaining two converters. In the zoomed inset, we can also see that by the time they reach V_{max}, the supercapacitor voltages are not yet balanced. This second case demonstrates that the current strategy is prone to control saturation. Once saturated, it can no longer achieve the stated twin goals of charging and balancing.

2.3.3 Adapting the Strategy

We saw in the previous subsection that the problem of control saturation in modular converter circuits is basically due to the overlap between the ranges of the low-side and high-side voltages when charging while at the same time balancing. In such a scenario, the converters are in buck mode and control saturation is approached as $D_j \to 1^-$ and occurs when $v_{\text{out},j} = v_{\text{sc},j}$.

It is possible to modify the normal mode of the voltage-balancing strategy to consider control saturation. If we know that a converter will saturate at any point within the charging period, then we can saturate it on purpose from the start. We do this to correct and increase the amount of energy the supercapacitors connected to the converters that we know will never saturate get. Seen from this angle, the supercapacitor connected to a converter that eventually saturates gets more than its fair share of energy, as is the case in Fig. 2.8. The modified strategy will deduct the energy at the beginning. The challenge in implementing this method is that we must know which converters will eventually saturate.

If the supercapacitor state of charge (SoC) were instead used in the strategy, control saturation cannot be accounted for in balancing supercapacitor voltages. The reason for this is that in considering the SoE in (2.2), the total energy needed to arrive at the rated voltage (when charging) is known and prediction of control saturation is possible. It thus becomes possible to adjust the power share of the converters that will saturate to achieve voltage equalization goals. In supercapacitors, the SoE is also a more useful metric because measuring voltage allows one to readily calculate the SoE. On the other hand, current is the important parameter for batteries that allows calculation of the SoC [73].

2.3.4 Proposed Scheme

The weighting factor in (2.16) was specially defined to be constant throughout the charging period by considering the individual and total energies needed to charge the supercapacitors. The converters should thus have constant output voltages. We can then use the weighting factor to know which converters will eventually saturate.

Let us again consider the system in Fig. 2.2. How do we predict which converters will saturate? Remember that control saturation occurs when $v_{\text{out},j} = v_{\text{sc},j}$. Therefore, if supercapacitor j charges fully to $V_{\max}$ at the end of the charging period and control saturation is reached, $v_{\text{out},j} = V_{\max}$ at that point. In fact, $V_{\max}$ serves as a boundary separating saturated converters $\left(v_{\text{out},j} \leq V_{\max}\right)$ from those that are not $\left(v_{\text{out},j} > V_{\max}\right)$. Since the reference converter output voltages and the weighting factors of the strategy are constant, they must have the same value even at the beginning of the charging period. First, we define a base weighting factor $w_{1(\text{base}),j}$ computed from (2.16) considering all converters in the summation in the denominator (without regard for control saturation). The "1(base)" in $w_{1(\text{base}),j}$ was added in the suffix as an additional qualifier to denote that we are currently in the first check and that it is the base weighting factor for the current check, i.e., the weighting factor before the check. The concept of checks will be developed in the next paragraphs. Based on (2.19), where $w_j = V_{\text{ref},j}/V_{\text{ref,total}}$, we can also define a base threshold weight $w_{1(\text{th})}$, where the "th" in the suffix is for threshold, that we can use to predict whether a converter will eventually saturate or not:

$$w_{1(\text{th})} = \frac{V_{\max}}{V_{\text{ref,total}}} \tag{2.20}$$

As just discussed, if the inequality $v_{\text{out},j} \leq V_{\max}$ is true for converter j, we know that this converter will eventually saturate. We can express this inequality in terms of weighting factors using (2.19) again: as a first check, if $w_{1(\text{base}),j} \leq w_{1(\text{th})}$, then converter j will saturate; otherwise, it will not. We could then deliberately saturate the converters that satisfied the condition. For these converters, the reference voltage becomes: $V_{\text{ref},j} = r_{\text{sat}} v_{\text{sc},j}$, where r_{sat} is a factor slightly greater than unity serving as a security margin. They are also included in the set S, which is the set of all converters that we just predicted will saturate and whose size is $n_{S,1}$. If converter j will saturate, then $j \in S$. The converters contained in S are also removed from the application of the strategy to the remaining converters that will not saturate. For the latter, the reference voltage becomes:

$$V_{\text{ref},j} = \left(V_{\text{ref,total}} - \sum_{m \in S} V_{\text{ref},m}\right) w_{1,j} \tag{2.21}$$

where $j \notin S$ and $w_{1,j}$ is the weighting factor computed by not including the $n_{S,1}$ converters in S from the summation in the denominator of (2.16).

Consider how the energy needed to charge a supercapacitor is calculated in (2.12). ΔE_j tends to decrease as $v_{\text{sc},j} \to V_{\max}$ during a charge. For deliberately saturated converters contained in set S, the rate of decrease of ΔE_j is less than the rate of decrease of the remaining converters that are not saturated. This has an effect on how the weighting factors behave as defined in (2.16). Remember that when we add all of the weighting factors, the sum must always be 100%. If that is the case, then the weighting factor $w_{1(\text{base}),j}$ of deliberately saturated converters would just increase because of the smaller rate of decrease of ΔE_j during the charge. On the other hand, the $w_{1(\text{base}),j}$ of the remaining converters would decrease. We can use this fact and we then stop deliberately saturating until all converters reach $w_{1(\text{base}),j} > w_{1(\text{th})}$.

In other words, deliberately saturated converters increase their power share (expressed as $w_{1(\text{base}),j}$) during the charge. On the other hand, the remaining converters that are not saturated decrease theirs. This attribute of the strategy opens to a possible problem. What if the converters that in the beginning will not saturate suddenly have $w_{1(\text{base}),j} \leq w_{1(\text{th})}$ because of their decreasing power share? How do we predict from the start that they will also undergo control saturation even though $w_{1(\text{base}),j} > w_{1(\text{th})}$ originally? Here, we define the next threshold weight $w_{2(\text{th})}$ to do it:

$$w_{2(\text{th})} = \frac{V_{\max}}{V_{\text{ref,total}} - n_{S,1} V_{\max}} \tag{2.22}$$

where $n_{S,1}$ is the number of converters that will saturate based on the first check and the "2" in the suffix denotes second check. For this check, we verify if the condition $w_{2(\text{base}),j} \leq w_{2(\text{th})}$, where $j \notin S$, is true. The base weighting factor for the second check $w_{2(\text{base}),j}$ considers only those converters that will not saturate based on the first check. The $n_{S,1}$ converters are thus excluded from the new computation of (2.16). Like in the previous step, we also deliberately saturate converters based on the condition through the reference voltage: $V_{\text{ref},j} = r_{\text{sat}} v_{\text{sc},j}$. For the remaining converters that will not saturate, the reference voltage is:

$$V_{\text{ref},j} = \left(V_{\text{ref,total}} - \sum_{m \in S} V_{\text{ref},m} \right) w_{2,j} \tag{2.23}$$

where S now includes converters from the second check and $w_{2,j}$ is the weighting factor computed by removing all converters in S from the summation in the denominator of (2.16).

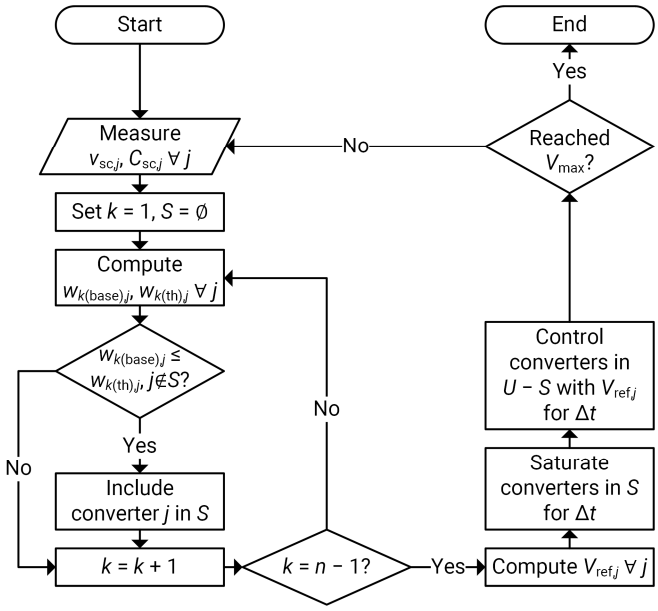

Fig. 2.9. Flowchart of the the control saturation-adapted voltage-balancing strategy algorithm

In general, we can continue the process for the third, fourth checks, and so on until the last possible $(n-1)^{\text{th}}$ check. To summarize, the steps of the control saturation-adapted voltage-balancing strategy are:

1. For the time step Δt, perform $(n-1)$ checks. At each k^{th} check, where $k \in \{1,2,\dots,n-1\}$, compute $w_{k(\text{base}),j}(t)$ first:

$$w_{k(\text{base}),j}(t) = \frac{\Delta E_j(t)}{\sum_{m \in U-S} \Delta E_m(t)} \tag{2.24}$$

   where U is the set of all converters and S is the set of all converters within U that will surely saturate $(S \subseteq U)$. Note that $S = \emptyset$ when $k = 1$.

2. Within the same k^{th} check, compute $w_{k(\text{th})}(t)$ as well:

$$w_{k(\text{th}),j}(t) = \frac{V_{\max}}{V_{\text{ref,total}} - n_{S,k-1} V_{\max}} \tag{2.25}$$

3. Verify that $w_{k(\text{base}),j}(t) \leq w_{k(\text{th})}(t)$ for $j \notin S$ for the k^{th} check. If true, update set S to include converter j. Then, proceed to the next check.

4. After the $(n-1)$ checks, deliberately saturate the converters in S according to $V_{\text{ref},j}(t) = r_{\text{sat}} v_{\text{sc},j}(t)$, where r_{sat} is slightly greater than unity. The remaining converters in the set $U - S$ are then controlled according to:

$$V_{\text{ref},j}(t) = \left[V_{\text{ref,total}} - \sum_{m \in S} V_{\text{ref},m}(t) \right] w_{n-1,j}(t) \tag{2.26}$$

5. Repeat steps 1–4 for the next time steps until the supercapacitors reach $V_{\max}$.

Fig. 2.9 represents the steps above for the control saturation-adapted energy-based strategy as a flowchart. Adapting the basic strategy in Fig. 2.6 basically entailed predicting which converters will saturate. These converters are then deliberately saturated at the beginning to decrease their overall energy share and achieve voltage equalization at the end. The proposed strategy with its prediction of all converters that will eventually saturate by exhausting through threshold checks is a unique take on this unique problem. It is a novel contribution to voltage-balancing strategies.

2.4 Simulation

We simulated the system and the strategy as described in the previous two sections. To demonstrate the operation of the strategy, we modeled the 50 kW system of the Hybus application and tested it in simulation.

2.4.1 Simulation Setup

We modeled and simulated the modular power converter system as represented in Fig. 2.2(a). The sizing of the modular converters follows from the Hybus application that used a single 50 kW converter to interface 120 supercapacitor cells of 3 kF in recovering the breaking energy and in supplementing power during electrical microcuts in a trolleybus [27]. Temperature is important in the evolution of cell capacitance and ESR, but it is difficult to ensure thermal homogeneity in a supercapacitor stack [31]. Cells were thus grouped according to their thermal behavior to ensure that voltage imbalance within a group is kept minimal. Following this, we decided to group the supercapacitors by 12. SC_j in Fig. 2.2(a) can thus be treated as the equivalent supercapacitor of 12 cells connected in series. The grouping of the cells was much the same as in Fig. 2.1 where a single supercapacitor stack in Fig. 2.1(a) was divided into n groups in Fig. 2.1(b). For simplicity, only three converters ($n = 3$) were considered (i.e., $n_{cells} \times n = 36$ cells) for the first two case studies, while the third one has the full sizing ($n = 10$) (i.e., $n_{cells} \times n = 120$ cells) considered.

Table 2.2. Simulation supercapacitor (SC) group parameters

Parameter	Variable	Value	Unit
Case studies 1–3 (simulation)			
Cell max. voltage	$V_{\text{max,cell}}$	2.7	V
No. of cells in string	n_{cells}	12	–
Group max. voltage	V_{max}	32.4 $(= V_{\text{max,cell}} \times n_{\text{cells}})$	V
Group min. voltage	V_{min}	16.2 $\left(= \frac{V_{\text{max,cell}}}{2} \times n_{\text{cells}}\right)$	V

Table 2.3. Simulation supercapacitor (SC) cell parameters

Supercapacitor group	Capacitance (F)	ESR (mΩ)
Variable	C_{sc}	R_{sc}
Nominal	250 $(= 3{,}000/n_{\text{cells}})$	3.48 $(= 0.29 \times n_{\text{cells}})$
Case studies 1–2 (simulation)		
SC_1	262.5	3.31
SC_2	250	3.48
SC_3	237.5	3.65
Case study 3 (simulation)		
SC_1	258.67	3.39
SC_2	249.67	3.23
SC_3	249.42	3.15
SC_4	236.7	4.21
SC_5	266.98	3.96
SC_6	247.78	3.57
SC_7	238.09	3.11
SC_8	272.53	3.23
SC_9	246.25	3.43
SC_{10}	240.18	3.71

The characteristics of the supercapacitors within a group were considered uniform. Table 2.2 gives the group operating voltage range of the 3-kF supercapacitors used in the simulation of the test cases. Each supercapacitor cell is limited in use within the usual 1.35–2.7 V range. On the other hand, Table 2.3 provides the different values of group *RC* model parameters to replicate the tolerance in nominal values of real supercapacitors. For cast studies 1 and 2, values for SC_1 and SC_3 were set to be ±5% of the values for SC_2 cells. For case study 3 however, normally distributed random values were generated based on a tolerance of ±20% for the cell capacitance (mean $\mu = 3$ kF, i.e., nominally 250 F for 12 cells in series; standard deviation $\sigma = 0.2\mu/3$ F) and ±25% for the cell ESR ($\mu = 0.29$ mΩ, i.e., nominally 3.48 mΩ for 12 cells in series; $\sigma = 0.25\mu/3$ mΩ).

Following still the partitioning of the original 50 kW system, the specifications of the modular converters are detailed in Table 2.4. Each converter nominally has 35 V at the output, so the regulation

Table 2.4. System specifications of the simulation setup

Parameter	Variable	Value	Unit
Case study 3 (simulation)			
System power rating	P_{max}	50	kW
Test system power	P_{test}	17.5	kW
System bus voltage	$V_{\text{ref,total}}$	350	V
No. of cascaded converters	n	10	–

of the bus voltage $V_{\text{ref,total}}$was set at 105 V for case studies 1 and 2 and at 350 V for case study 3, while the charging current was set at i_{out} = 50 A. The three converters in case studies 1 and 2 processed 5.25 kW of power in total (or 1.75 kW per converter), while the ten converters in case study 3 processed 17.5 kW in total (still 1.75 kW per converter). The voltage-balancing strategy was applied to the system with a time step of Δt = 0.2 s.

2.4.2 Use of the Strategy and Efficiency

Simulation of the system was done in Simscape, an environment within MATLAB and Simulink for multidomain physical modeling and simulation. Based on the steady-state behavior of the converter in (2.9) and (2.10), the expression for the buck mode efficiency η_{buck} considering only conduction losses can also be obtained:

$$\eta_{\text{buck}} = \frac{P_{\text{in}}}{P_{\text{out}}} = 1 - \frac{i_{\text{out}}}{v_{\text{out}}}\left[\frac{R_L + R_{\text{DS(on)}} + R_C D(1-D)}{D^2}\right] \tag{2.27}$$

To see the effects of loading and the duty cycle on the efficiency, the plot of (2.27) in different conditions is shown in Fig. 2.10. Curves for the boost mode efficiency η_{boost} are also shown.

Considering first the full-rated load in buck mode where i_{out} = 143 A (= $P_{\text{max}}/V_{\text{ref,total}}$), the duty cycle should be $D_{\text{buck}} \geq 0.54$ to achieve at least 90% efficiency. The range of duty cycle values that is at least 90% efficient increases as i_{out} decreases because of the inverse relationship between the current and the load. This means that a lower i_{out} is preferred when using the voltage-balancing strategy to charge supercapacitors. In applications however, charging time should be balanced against the choice of a lower charging current and a higher efficiency.

For the case study-rated load of i_{out} = 50 A (= $P_{\text{test}}/V_{\text{ref,total}}$) in Fig. 2.10, $D_{\text{buck}} \geq 0.31$ for at least 90% efficiency and $D_{\text{buck}} \geq 0.45$ for at least 95%. Assuming a nominal output voltage v_{out} = 35 V, these correspond to an $SoE \approx 11.2\%$ (v_{sc} = 0.9 V per cell) and an $SoE \approx 23.6\%$ (v_{sc} = 1.3 V per cell), respectively, following the formula in (2.2). This means that the SoE could be as low as 11% at the

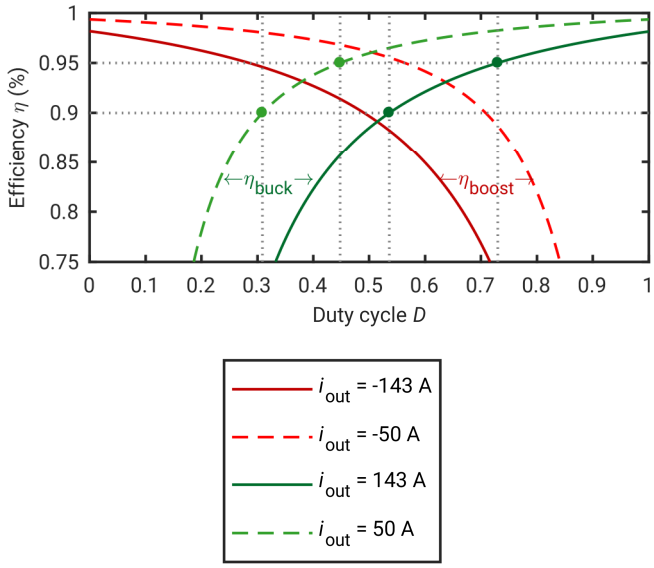

Fig. 2.10. Bidirectional converter efficiency as a function of duty cycle and load: green represents charging supercapacitors (buck mode) and red represents discharging (boost mode) [68] © 2022 IEEE

beginning of the charging period and the efficiency would still be at least 90%. As the supercapacitors charge, v_{in} will only increase and further improve the efficiency according to (2.11) and (2.27). Recall that the voltage v_{in} is the general input voltage to a converter. It becomes v_{sc} when supercapacitors are considered. Note however that the preceding analysis has underestimated values because other sources of losses such as switching and magnetic losses among others were not considered.

2.4.3 Simulation results

The simulations were run based on three test cases. In their case studies, supercapacitors have different initial voltages given in Table 2.5. Values for case studies 1 and 2 were chosen to demonstrate the operation of the control saturation-adapted strategy, while cell values for case study 3 were normally distributed random numbers (for each cell $\mu =$ 2.13 V, i.e., 25.61 V for 12 cells; $\sigma =$ 0.1 V).

2.4.3.1 Case Study 1

In this first case study (cf. Table 2.2–Table 2.5), a converter is expected to enter control saturation during charging. We have seen how the strategy cannot deal with such a condition in subsection 2.3.2 without the adaptation in section 2.3. The results of the new strategy are shown in Fig. 2.11. We can see in Fig. 2.11(a) that the control saturation-adapted strategy was effective in balancing voltages at 29 s. Doing the two checks, the strategy decided that two converters had to be deliberately saturated: 1 and 2, as can be seen in Fig. 2.11(e) indicating the saturation command.

Table 2.5. Supercapacitor (SC) initial conditions for the simulation case studies

Supercapacitor group	Initial voltage (V)
Case study 1 (simulation)	
SC_1	26.4
SC_2	25.8
SC_3	23.4
Case study 2 (simulation)	
SC_1	26.4
SC_2	24
SC_3	21
Case study 3 (simulation)	
SC_1	24.46
SC_2	23.36
SC_3	26.13
SC_4	23.14
SC_5	23.7
SC_6	27.96
SC_7	24.81
SC_8	25.31
SC_9	27.18
SC_{10}	25.02

In Fig. 2.11(c), the threshold weight of the first check during charging is represented as $w_{1(\text{th,c})}$. There are upper and lower limits (delineated in the figure by the region in light green) to the threshold because of the addition of a hysteresis control, which was done to prevent chattering. Thus, the condition $w_{1(\text{base}),j} \leq w_{1(\text{th,c})}$ is false once $w_{1(\text{base}),j}$ equals the upper limit of the threshold and only changes to true once $w_{1(\text{base}),j}$ equals the lower limit. Since both converters 1 and 2 initially come from below the upper threshold limit, $w_{1(\text{base}),j} \leq w_{1(\text{th,c})}$, is true at the start, thus the need for saturating them. At 2.4 s, converter 2 clears the first check because $w_{1(\text{base}),2}$ touches the upper limit of the threshold.

Converter 2 will not be released from saturation until after 3 s (as seen in Fig. 2.11(e)) because the second check still showed in Fig. 2.11(d)–(e) that $w_{1(\text{base}),2} \leq w_{2(\text{th,c})}$ with hysteresis control. There was still a need to deliberately saturate it. The upper and lower threshold limits for the hysteresis control are not obvious because of the increased scale of the vertical axis, but $w_{2(\text{base}),2}$ touches the upper threshold limit at 3 s. Another thing to observe in the second check in Fig. 2.11(d) is the dependence on the first check. For example, $w_{2(\text{base}),j} = 0$ for converters to be deliberately saturated based on the previous check and $w_{2(\text{th,c})}$ changes value depending on their number.

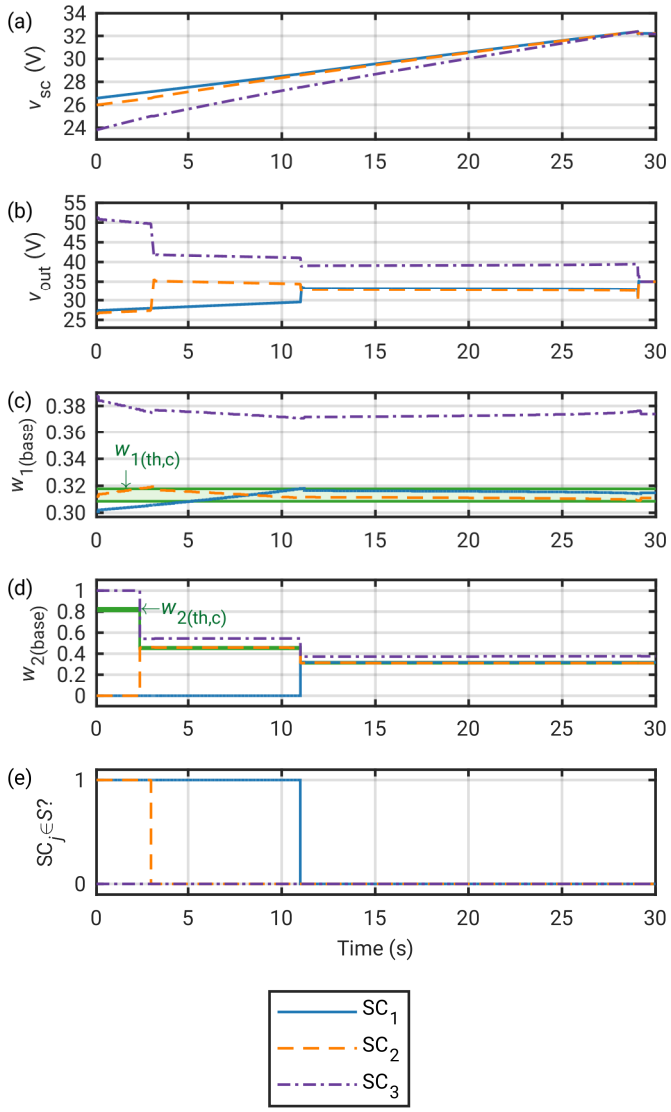

Fig. 2.11. Case study 1 (simulation): (a) Supercapacitor voltages; (b) Output voltages of the converters; (c) Weighting factors for the first check; (d) Weighting factors for the second check; and (e) Result of the two checks on whether to saturate converter j [68] © 2022 IEEE

Beyond 3 s, only converter 1 needed to be deliberately saturated. At 11 s, all three weighting factors ($w_{1\,(\text{base}),j}$) clear the two checks. Thereafter, the normal mode of the control saturation-adapted strategy operated to charge the supercapacitors until $V_{\max}$.

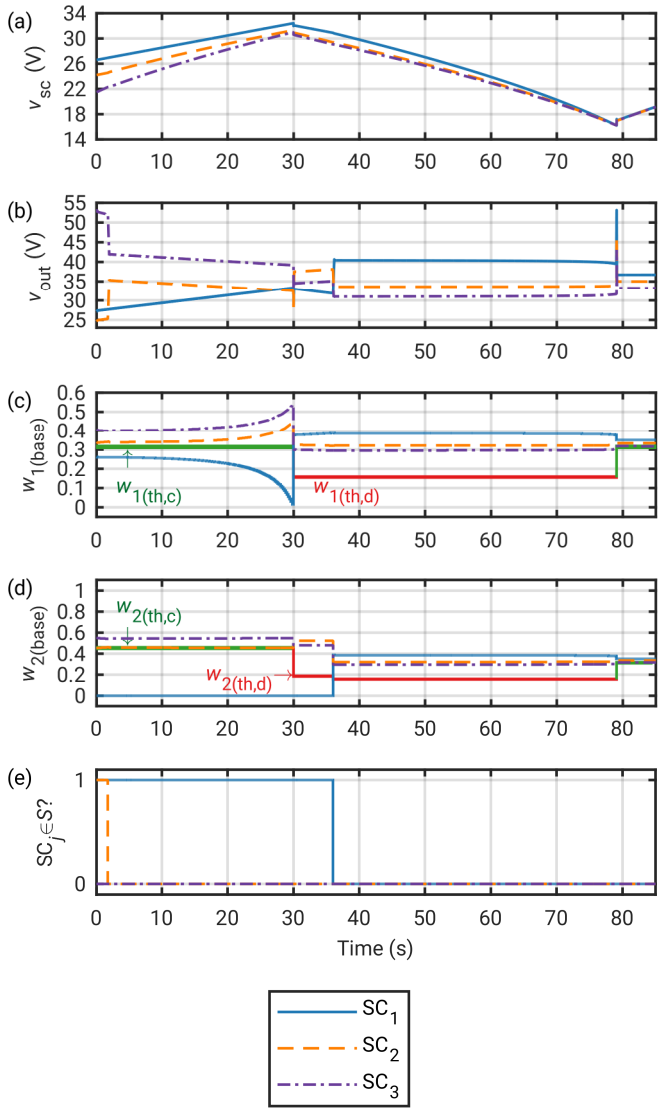

Fig. 2.12. Case study 2 (simulation): (a) Supercapacitor voltages; (b) Output voltages of the converters; (c) Weighting factors for the first check; (d) Weighting factors for the second check; and (e) Result of the two checks on whether to saturate converter j

2.4.3.2 Case Study 2

The second case study (cf. Table 2.2–Table 2.5) demonstrates a limitation of the control saturation-adapted strategy. The results for this test case are shown in Fig. 2.12. It is obvious from Fig. 2.12(a) that while SC_1 already reached V_{max}, the two other supercapacitors have not. Converter 1 was deliberately saturated during the whole of the charging period, as can be seen in Fig. 2.12(c)–(e). The initial voltages of the supercapacitors produced a combination of weighting factors for which the strategy's adaptation to control saturation cannot work. This can be seen in $w_{1\,(\mathrm{base}),1}$ that decreases during the charging period despite deliberate saturation of converter 1. In such a case, it is still possible

to balance the voltages. However, it will have to take more time than the current charging period. The plan is to apply the strategy even during discharge. To do this, ΔE_j in (2.12) must be modified to:

$$\Delta E_j(t) = \frac{1}{2} C_{\mathrm{sc},j}\left[v_{\mathrm{sc},j}^2(t) - V_{\min}^2\right] \tag{2.28}$$

for the discharge period. $V_{\min}$ refers to the rated minimum operating voltage of the supercapacitor. Usually, its value is half of $V_{\max}$. Accordingly, the threshold in (2.25) must be modified to reflect discharging during this period:

$$w_{k(\mathrm{th,d}),j}(t) = \frac{V_{\min}}{V_{\mathrm{ref,total}} - n_{S,k-1} V_{\min}} \tag{2.29}$$

Like in the first case study, hysteresis control of the checks was used for the thresholds to decide the deliberate saturation of the converters. We can see in Fig. 2.12(a) that the supercapacitor voltages are balanced by the time they reached $V_{\min}$ at 79.1 s. Based on Fig. 2.12(c)-(d), there was no need to saturate any converter during the discharge period. It is clear that the thresholds are significantly lower, which means less probable deliberate need for converter saturation of the converters and more flexibility. However, if the resulting $V_{\mathrm{ref},j} \leq v_{\mathrm{sc},j}$ but $w_{k(\mathrm{base}),j} < w_{k(\mathrm{th,d}),j}$ (which is possible during discharge), then deliberate saturation of converter j must still be done. This additional verification is an added step during discharge.

Case study 2 shows that the proposed control saturation-adapted strategy can be used as a general fast voltage-balancing strategy for both charging and discharging periods.

2.4.3.3 Case Study 3

The last case study (cf. Table 2.2–Table 2.5) illustrates the use of the strategy on a ten-converter system (n = 10) with full sizing. Supercapacitor capacitance and ESR parameters were randomly generated from a normal distribution, as were the initial voltages. As in the previous two case studies, hysteresis control of the condition used in the checks was implemented to prevent chattering. The results are shown in Fig. 2.13. Because the system requires nine checks, the weighting factors are excluded from the figure.

It is clear from Fig. 2.13(a) that the strategy could not balance the supercapacitors before SC_6 reached $V_{\max}$ at 20.7 s. From this point forward, no converter needed to be deliberately saturated, much like in the previous case study. The strategy nevertheless needed the time during discharge for all supercapacitors to reach $V_{\min}$ at 64.9 s. Beyond that, the normal mode of the strategy worked to keep the supercapacitors balanced.

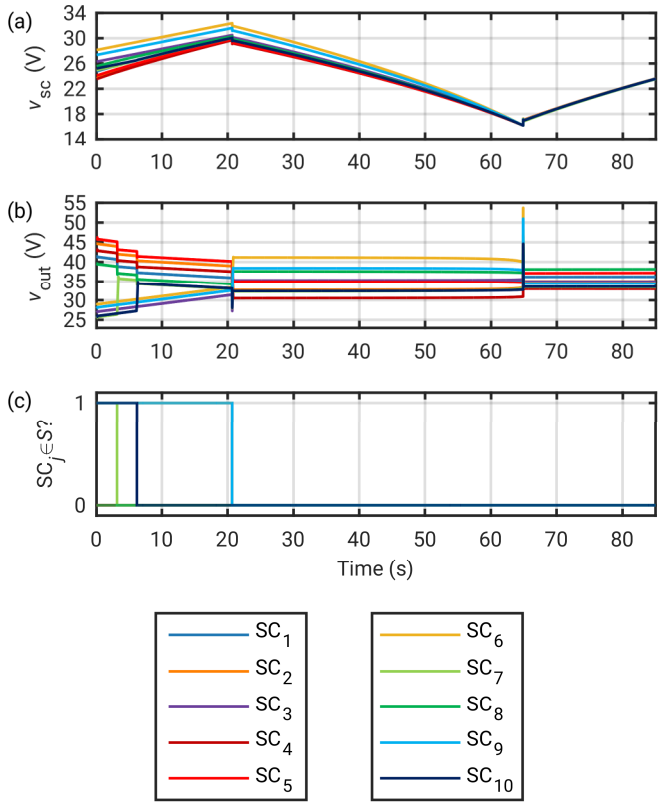

Fig. 2.13. Case study 3 (simulation): (a) Supercapacitor voltages; (b) Output voltages of the converters; and (c) Result of the nine checks on whether to saturate converter j [68] © 2022 IEEE

We can see in Fig. 2.13(b)–(c) that five converters were deliberately saturated at the very start. They were converters 3, 6, 7, 9, and 10. The supercapacitors connected to them required lower energy shares in order for the strategy to balance the system. One by one, the deliberately saturated converters are released from saturation based on the nine checks: converter 7 at 3.2 s; converter 10 at 6.2 s; and the other three (converters 3, 6, and 9) at the point where SC_6 reached V_{max} at 20.7 s. This case study shows that the strategy works for larger systems.

2.5 Experimental Results

The strategy was also experimentally implemented on a small-scale 30 W system with three modular converters. We look at the experimental case study in detail in this section.

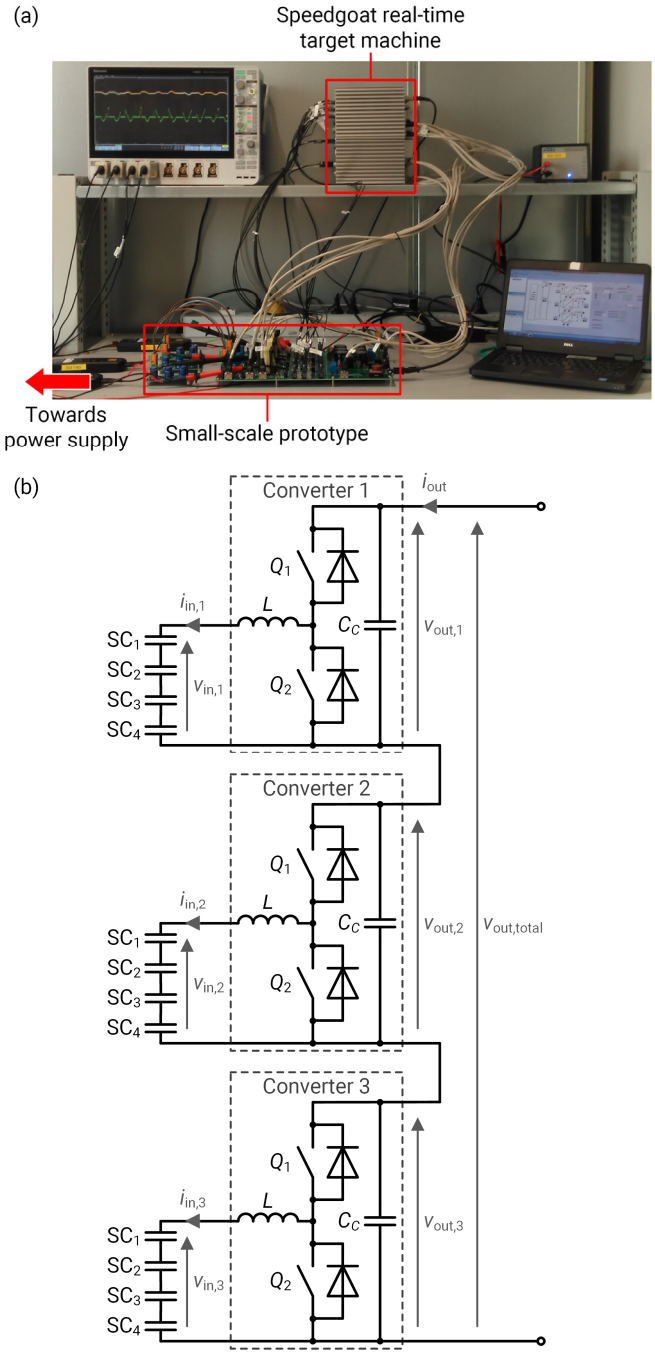

Fig. 2.14. (a) Photo of the experimental setup of a small-scale prototype composed of three modular converters with connected supercapacitors [68] © 2022 IEEE and (b) Schematic diagram of the setup

2.5.1 Experimental setup

A small-scale 30W prototype of a bidirectional modular converter system with supercapacitor energy storage represents the system in Fig. 2.2(a) and serves as a test bench for the experimental

Table 2.6. Experimental supercapacitor (SC) group parameters

Parameter	Variable	Value	Unit
Case studies 4–6 (experimental)			
Cell max. voltage	$V_{\text{max,cell}}$	2.5	V
No. of cells in string	n_{cells}	4	–
Group max. voltage	V_{max}	10 $(= V_{\text{max,cell}} \times n_{\text{cells}})$	V
Group min. voltage	V_{min}	6.2 $\left(= \frac{1.24 V_{\text{max,cell}}}{2} \times n_{\text{cells}}\right)$	V

Table 2.7. Experimental supercapacitor (SC) cell parameters

Supercapacitor group	Capacitance (F)	ESR (mΩ)
Nominal	6.25 $(= 250/n_{\text{cells}})$	64 $(= 16 \times n_{\text{cells}})$
Case studies 4–6 (experimental)		
SC_1	6.25	64
SC_2	6.25	64
SC_3	6.25	64

Table 2.8. Modular converter and system specifications of the experimental setup

Parameter	Variable	Value	Unit
Switching frequency	f_s	50	kHz
System output current	$i_{\text{out,max}}$	±857	mA
Test system output current	i_{out}	±400	mA
Converter nominal output voltage	v_{out}	11.67	V
Converter input voltage range	v_{in}	5.4–10.8	V
Converter inductor	L	1.3	mH
Converter capacitor	C_C	30	µF
Control strategy time step	Δt	0.2	s
Case studies 4–6 (experimental)			
System power rating	P_{max}	30	W
Test system power	P	14	W
System bus voltage	$V_{\text{ref,total}}$	35	V
No. of cascaded converters	n	3	–

implementation of the voltage-balancing strategy [32]. The modular converters were controlled by a Speedgoat real-time target machine that interacted with its workstation user interface through Simulink Real-Time Explorer. The control system in Fig. 2.2(b) was programmed into the target machine using MATLAB and Simulink. Fig. 2.14(a) shows a photo of the experimental setup. It is composed of three modular converters on a motherboard connected to supercapacitor groups on daughterboards. Meanwhile, Fig. 2.14(b) gives us the schematic diagram of one of the modular converters.

Connected to each modular converter in the prototype is a supercapacitor group composed of a string of four 25 F cells on one daughterboard, as illustrated in the circuit diagram of Fig. 2.14(b). Table

Table 2.9. Supercapacitor (SC) initial conditions for the experimental case studies

Supercapacitor group	Initial voltage (V)
Case study 4 (experimental)	
SC_1	6.32
SC_2	6.18
SC_3	6.04
Case study 5 (experimental)	
SC_1	7.3
SC_2	7.23
SC_3	6.01
Case study 6 (experimental)	
SC_1	7.47
SC_2	7.24
SC_3	6.01

2.6 shows the group operating voltage range while Table 2.7 provides the *RC* model parameters of the supercapacitors. Three modular converters comprise the prototype and each converter has a nominal output voltage of 11.67 V. Regulation of $V_{\text{ref,total}}$ was set at 35 V, while charging current was set at i_{out} = 400 mA. Specifications of the modular power converters and of the experimental setup are detailed in Table 2.8.

2.5.2 Experimental results

Like in the simulation case studies, three cases were experimentally tested. The initial voltages of the supercapacitors for the three cases were set at different values to demonstrate the operation of the control saturation-adapted voltage-balancing strategy. These initial voltages are shown in Table 2.9.

2.5.2.1 Case Study 4

The first experimental test case (cf. Table 2.6–Table 2.9) shows the normal mode of the strategy without the need to deliberately saturate any converter, much like the ideal example in Fig. 2.7. Fig. 2.15 shows the experimental results. With a small initial voltage difference+/- 0.14 V between the supercapacitors, balancing worked for the supercapacitor voltages to simultaneously reach 10 V at 45 s, as shown in Fig. 2.15(a). In order to see the small values, the maximum difference among supercapacitor voltages $v_{\text{d,max}} = v_{\text{sc,max}} - v_{\text{sc,min}}$ was plotted in Fig. 2.15(b). The maximum value among supercapacitor voltages is $v_{\text{sc,max}}$, while $v_{\text{sc,min}}$ is the minimum.

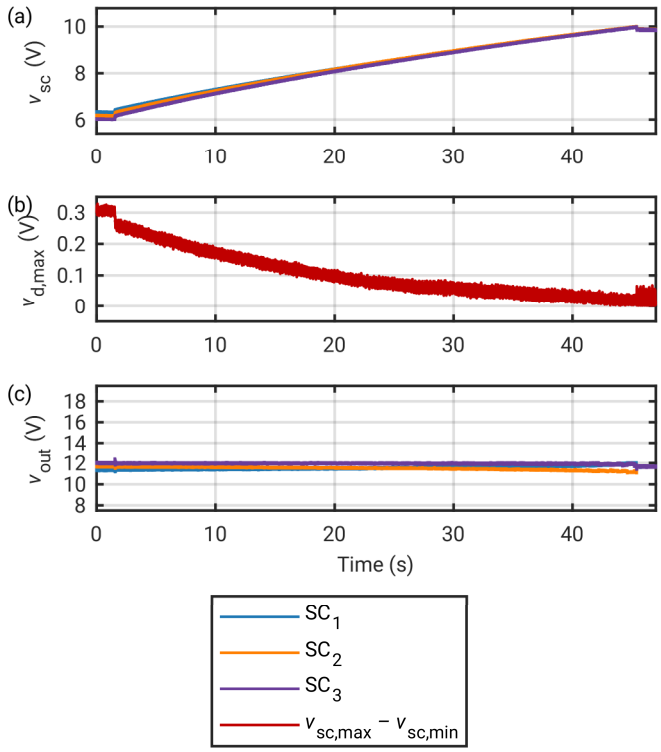

Fig. 2.15. Case study 4 (experimental, r_{sat} = 1.14): (a) Supercapacitor voltages and (b) Output voltages of the converters

Unlike in the case of Fig. 2.7 and the simulation case studies in normal mode, the output voltages in this experimental case are not constant. This is most obvious for $v_{out,2}$ in Fig. 2.15(b), which went from having a value between $v_{out,1}$ and $v_{out,3}$ at the beginning, to being the lowest at 45 s. This behavior is explained by the assumption in (2.12) that $C_{sc,j}$ is constant throughout the operation of a supercapacitor. In reality, the capacitance depends on supercapacitor voltage, but the *RC* model assumes that it is a constant [77]. Thus, at around 25 s, when $v_{sc,2}$ started to overtake the two other supercapacitors, the strategy corrected this by lowering the power that went into SC_2 through a lower $v_{out,2}$.

The preceding discussion demonstrates that despite the nonconstant converter output voltages, the strategy still works. A more detailed explanation of this reason for this will be presented in the next case study.

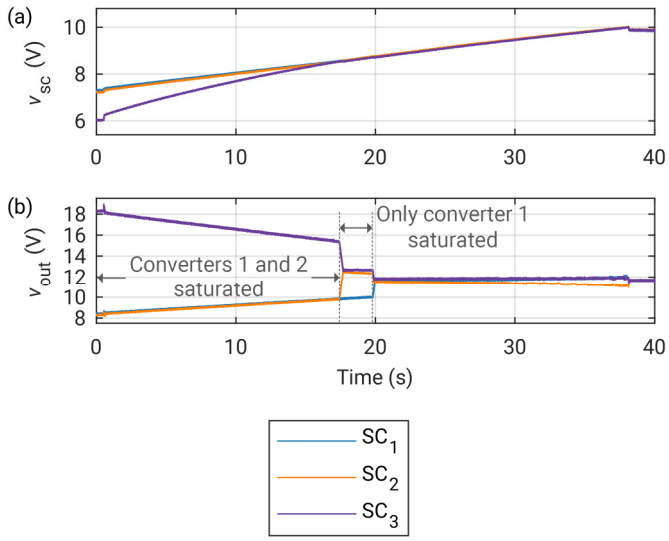

Fig. 2.16. Case study 5 (experimental, r_{sat} = 1.14): (a) Supercapacitor voltages and (b) Output voltages of the converters

2.5.2.2 Case Study 5

In this test case (cf. Table 2.6–Table 2.9), the initial supercapacitor voltages were chosen to demonstrate voltage balancing by deliberately saturating modular converters. Fig. 2.16 shows the experimental results. This test case corresponds to simulation case study 1 in Fig. 2.11 in terms of the actions taken by the strategy to arrive at balanced supercapacitor voltages.

As seen in Fig. 2.16(a), initial $v_{sc,1}$ was just slightly above $v_{sc,2}$, which itself was greater than $v_{sc,3}$ by a relatively huge value of 1.22 V. Because of the latter, the strategy had to minimize the power shares of SC_1 and SC_2 by deliberately saturating them. As can be seen in Fig. 2.16(b), SC_2 was saturated until 17 s, while SC_1 was saturated until 20 s. From then on, the normal mode of the strategy worked to balance the voltages until they reach 10 V at 38 s.

Not unlike the previous test case, the converter output voltages are nonconstant. A higher r_{sat} compared to the simulation case studies serves not only to secure the mock-up during transients, but also to account for the nonconstant output voltages during times of no saturation (normal mode). A higher r_{sat} means a larger V_{max} and $v_{out,j}$. Going back to this and to the previous case study, even if $v_{out,2}$ were to go lower during the normal mode, there would still be enough voltage difference between it and $v_{sc,2}$ thus ensuring that the supercapacitor voltages were balanced.

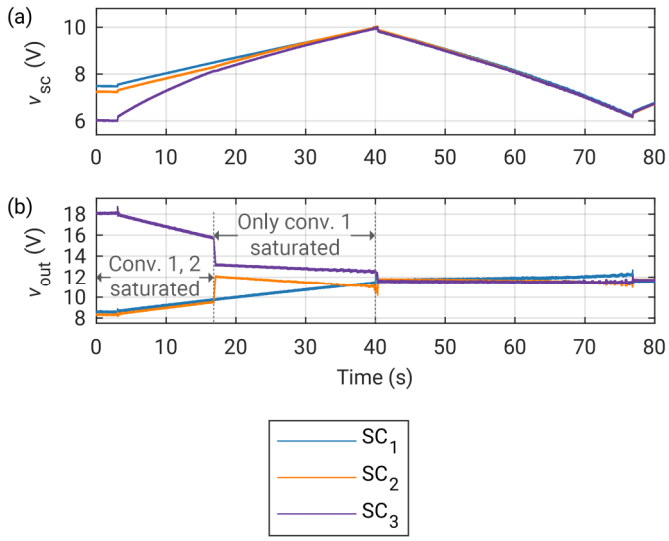

Fig. 2.17. Case study 6 (experimental): (a) Supercapacitor voltages and (b) Output voltages of the converters

2.5.2.3 Case Study 6

This last experimental test case (cf. Table 2.6–Table 2.9) demonstrates the operation of the control saturation-adapted strategy even during discharge. It corresponds to simulation case study 2 whose results are discussed in subsection 2.4.3.2 where (2.28) and (2.29) were defined as the equations that govern the operation of the strategy when supercapacitors are discharging. Fig. 2.17 shows the experimental results. The supercapacitor voltages are completely balanced by the time they reach 6.2 V at the 77 s mark, as shown in Fig. 2.17(a).

In terms of initial voltages, the present test case follows from the previous case study. There is a voltage difference of 0.23 V between $v_{sc,1}$ and $v_{sc,2}$, which itself is again greater than $v_{sc,3}$, by a relatively huge value of 1.23 V. Fig. 2.17(b) shows that SC_2 was saturated until the 16 s mark, while SC_1 was saturated throughout the whole charging period (until the 40 s mark). The supercapacitors may seem to be already balanced at the end of the charging period at the 40-s mark, but the saturation of SC_1 means that there was still a small difference in values. However, since the thresholds are different for the discharging period, the strategy operated in normal mode until the voltages are completely balanced at the 77 s mark.

Like in the corresponding simulation case study, this experimental case study shows that the control saturation-adapted strategy can be used as a general fast voltage-balancing strategy that works in both charging and discharging periods.

2.6 Conclusion

The case studies presented in this chapter show the principles of operation and limitations of the strategy for modular power converter balancing. Its use was initially limited by the difficulty of adapting it to control saturation. On the other hand, its features of constant weighting factors and constant converter output voltages made it easier to render it adaptable to control saturation. The proposed way works by deliberately saturating converters. Doing such corrects the energy shares to make the normal mode of the energy-based strategy work. The results show that the proposed strategy can be used as a fast voltage-balancing strategy during the supercapacitor charging period or as a general fast method even during discharge when balancing during a single charging period is not possible, regardless of system size.

Chapter 3

Online Supercapacitor Characterization

3.1 Introduction

Among various energy storage solutions, supercapacitors enjoy being one of the most efficient technologies with the longest lifetimes. They are capable of hundreds of thousands of deep charge-discharge cycles (with modern cells capable of even up to more than a million) because theoretically no chemical reaction takes place in the electrodes [10]. Aging is conventionally attributed to being driven mostly by processes affected by a cell's temperature and voltage level. Previously, the effects of cycling were not considered or were deemed negligible [11], [33]. However, more recent work on this subject introduced an additional factor in quantifying aging that accounts for cycling [12], [34]. The behavior of individual cells in a stack in terms of aging will briefly be considered in the following discussion.

When they are made, there is a natural tolerance to the parameters of supercapacitors because manufacturing processes themselves are not uniform [11], [14]. This is also true of other electrical energy storage devices like batteries [10]. The initial imbalance is exacerbated during operation because a cell's initial characteristics and system design affect its performance. In the Hybus project first mentioned in Section 2.1 and described in detail in Subsection 2.4.1 for example, the difference between the maximum and minimum temperatures in a supercapacitor stack during the accelerated aging test was as high as 36 °C at one point [31], [44]. Such a high difference in operating conditions leads to uneven aging of supercapacitor cells. For instance, an increase of 10 °C can reduce supercapacitor lifetime by a factor close of two [11]. State monitoring for diagnostics and maintenance purposes is thus warranted because nonuniform aging results in an abbreviated system life, whose duration is commonly taken to end once the weakest cell reaches one of the end-of-life criteria.

Considering the *RC* model comprised of a capacitance C_{sc} and an ESR R_{sc} first discussed in Subsection 2.2.2, we briefly explain here the behavior of these two macroscopic parameters that are

commonly kept under surveillance as a supercapacitor is used and ages. The capacitance increases slightly with an increase in temperature. It is more strongly correlated with an increase in bias voltage. In terms of aging, capacitance decreases with supercapacitor use, whether the mission profile resembles charge-discharge cycling or calendar aging (i.e., independent of cycle life). On the other hand, the resistance decreases with temperature, but increases with aging [14]. There are other factors that affect the two parameters like current and cycling frequency, but the factors just discussed are the most important.

Delving deeper into the effects of aging, application systems are designed to work within a specific range of operating conditions, so C_{sc} and R_{sc} cannot continue indefinitely as a supercapacitor is used lest the system go outside design specifications. For example, a decrease in capacitance leads to a reduction in the stored energy, which can easily be seen in their proportional relationship in equation (2.1). On the other hand, more heat is produced (and thus, more power is lost) as the internal resistance, the ESR, increases. This leads to increased heating of the supercapacitor stack, which is another important engineering problem. Thus, an end-of-life criterion is usually defined. This is normally the point when the supercapacitor's C_{sc} decreased by 20% or when the R_{sc} increased by 100% even though different limits could be set [14], [36], [74]. It is usually the case that the capacitance reaches the set end-of-life criterion before the ESR [36].

The foregoing discussion shows that the lifetime performance of supercapacitors heavily depends on both initial parameters, system design, and operational conditions. For them to operate within design specifications, there is a need for supercapacitor state monitoring systems. The information provided by such systems is crucial information for users of an application. Operation can be optimized for the desired function and the application itself maintained for sustained performance.

3.2 Supercapacitor Characterization

This section deals with the time- and frequency-domain characteristics of supercapacitors and how they evolve as a cell ages. It also discusses the attendant conventional characterization techniques and methods used for diagnostic and prognostic purposes.

3.2.1 Characteristics and Aging

At the device level, several causes were found to be at the root of supercapacitor aging according to a review of the literature: electrode impurities, overvoltage, excessive temperature, and cycling [35]. Metal impurities, surface functional groups, adsorbed water, and trapped hydrogen are just some of the electrode impurities that react with the electrolyte during supercapacitor operation producing solid and

gaseous products. Solvent decomposition and electrolyte evaporation are other processes producing gaseous products. Both solid and gaseous products reduce the contact surface between the electrode and the electrolyte. Solid products do this by blocking the electrode pores while gaseous products do this by being adsorbed on the electrode surface. Both products can also accumulate on the separator blocking the ionic charges. Gaseous products also increase internal pressure in the cell damaging the mechanical integrity of the components inside the cell and the cell packaging itself. The failure modes just described lead to a decrease in capacitance, an increase in the ESR, and may also lead to cell deformation. These three are the most obvious signs of supercapacitor aging. Impurities introduced into the electrode during fabrication is thus a dominant root cause of aging and failure. It is thus very important to reduce these impurities to a minimal level during manufacturing [35]. While capacitance and ESR are measurable through electrical characterization, cell deformation can either be visually observed or determined through a postmortem analysis of the cell.

Let us now turn our attention to the other root causes. Overvoltage, which means operating supercapacitor cells beyond the potential window of the solvent, causes the solvent to decompose. Excessive temperature also produces this in addition to bringing the electrolyte to evaporate and the electrolyte ions to intercalate into the electrodes. Both of these two root causes accelerate electrochemical reactions exponentially. The heat from the redox reactions during aging feeds back and contributes to the increase in temperature. As for the last root cause, cycling a supercapacitor cell through phases of charge and discharge generates significant heat that also adds to the increase in temperature. The cell's operating current, voltage, and temperature, thus, are all stressors as regards supercapacitor aging. However, the contribution of each depends highly on the type of application where a supercapacitor is used. This goes the same way for the root causes of supercapacitor aging and failure [35].

As previously discussed, a cell's capacitance and ESR are measured to characterize a supercapacitor. These quantities can serve not only as a diagnostic but also as a prognostic tool. Maxwell made public an application note containing data on the aging of its cells [36]. It also specifies the usual end-of-life criteria for supercapacitors. A cell can be considered to have reached its end of life once its capacitance has been reduced by 20% or once the ESR has increased by 100%. In practice, it is usual to observe capacitance reaching its end-of-life criterion first before ESR does. Fig. 3.1(a) shows the capacitance over time of a Maxwell supercapacitor cell that has been continuously measured using Maxwell's own measurement process. The evolution of the capacitance can be separated into three phases: (I) exponential decrease during the first cycles; (II) linear decrease during the main part of the life; and (III) slow exponential decrease due to natural aging. Because of the linear nature of the second

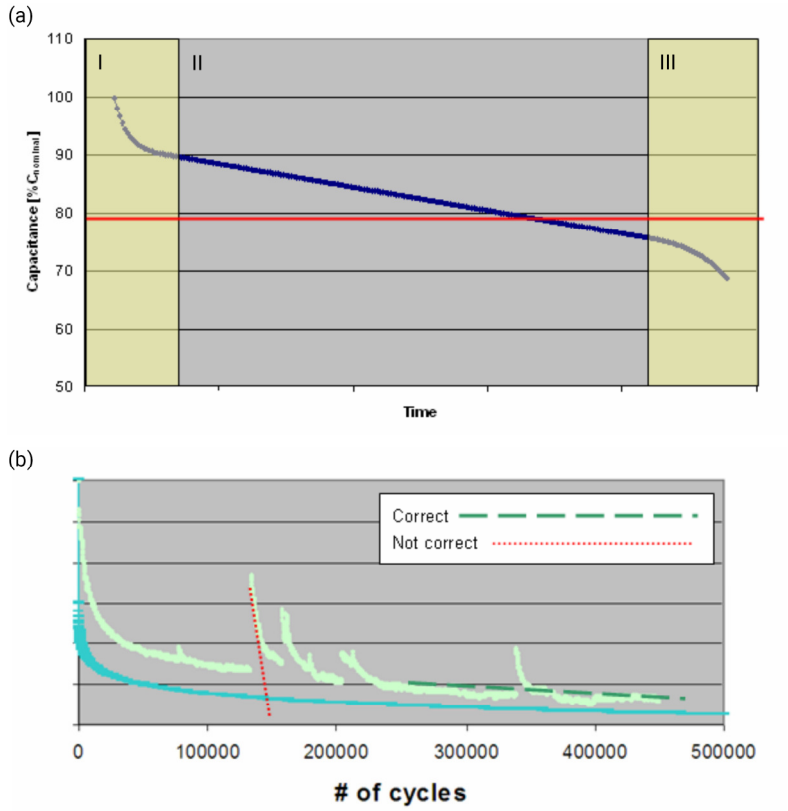

Fig. 3.1. Evolution of supercapacitor capacitance as it ages [36]: (a) The three domains: (I) exponential decrease, (II) linear decrease, and (III) slow exponential decrease in capacitance; and (b) The capacitance recovery phenomenon when the bias voltage is interrupted affecting correct measurement (observed using Maxwell's measurement process with a supercapacitor biased at 2.7 V at room temperature)

phase, it is possible to write a linear equation to calculate or estimate the cell's remaining useful life (RUL).

Maxwell also provided data on a phenomenon called recovery, which can be seen in Fig. 3.1(b) [36]. If the bias of the supercapacitor cell under test is interrupted after a period of continuous usage, the measured capacitance or ESR recovers as a function of the rest time. Recovery, which is also referred to as regeneration or relaxation, means that the measured capacitance (or ESR) upon resumption of operation will be significantly higher (or lower for ESR) compared to the previously measured value before the interruption. This phenomenon is relevant especially in the context of prognostics based on RUL. If a recovered capacitance value is used, it would result in an error in the calculations. It is thus recommended to wait before estimating RUL if recovery occurred. This could take as many as 40,000 cycles.

The time-domain characteristics of supercapacitor aging are clearly seen in Fig. 3.1. It is useful to see how this translates in the frequency domain. Fig. 3.2 shows how aging affects a supercapacitor's

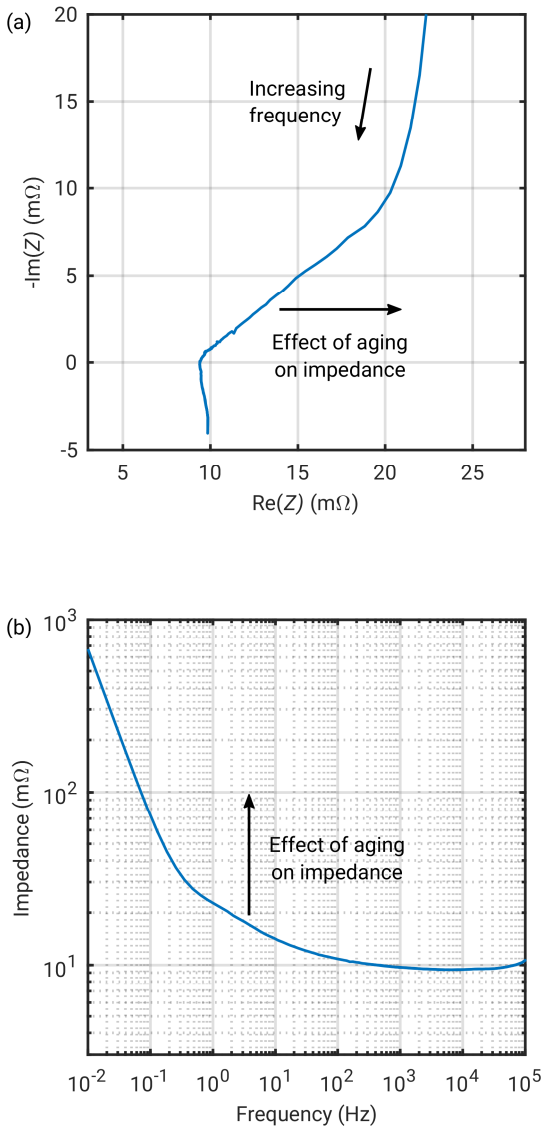

Fig. 3.2. Effect of aging on the impedance response of supercapacitors: (a) Nyquist impedance plot and (b) Bode modulus impedance plot

impedance response in the frequency domain. The response changes with aging in the direction indicated by the arrows for both the Nyquist and Bode plots in Fig. 3.2(a) and Fig. 3.2(b), respectively.

3.2.2 Time-Domain Characterization

Supercapacitors, also called electrical double-layer capacitors (EDLC) that have a significantly large energy density compared to common capacitors. Its construction is of two large-surface area electrodes with an thin layer of separator and electrolyte filling the porosities in between. Energy is stored as charge in the electric double layer at the two electrode-electrolyte interfaces [10], [14], [37],

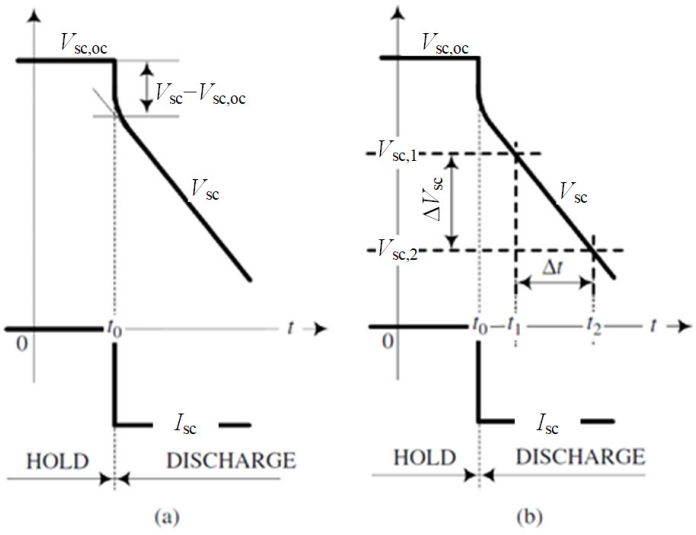

Fig. 3.3. Measurement of (a) ESR (R_{sc}) and (b) Capacitance (C_{sc}) during a transition from rest to a discharge phase [64]

[74], [78]. Capacitance C_{sc} in the *RC* supercapacitor model in Fig. 2.3(a), which characterizes an ideal capacitor, is the derivative of charge with respect to voltage. In practice, it is approximated by $C_{sc,meas}$ calculated from measurements:

$$C_{sc,meas} = \frac{I_{sc}\Delta t}{\Delta V_{sc}} \tag{3.1}$$

where two voltage measurements are made and I_{sc} is the constant current measurement through the capacitor, Δt is the time difference between the measurements, and ΔV_{sc} is the voltage difference between the measurements. In practical capacitors, real supercapacitors, a small current leaks through the separation in between the plates/electrodes causing voltage to decrease, i.e., they self-discharge over time [79].

On the other hand, measurement of the ESR takes advantage of the transition from a rest period when there is no current to a charge/discharge phase (or vice versa). Looking back at the *RC* model in Fig. 2.3(a), $v_{sc} = v_{Csc} + I_{sc}R_{sc}$ (with the DC charge/discharge current $I_{sc} = i_{sc}$ in the figure), it is not possible to directly measure the capacitor voltage v_{Csc} and have a value for it in order to isolate and solve for R_{sc}. However, when there is no current, open-circuit supercapacitor voltage $v_{sc,oc} = v_{Csc}$. Thus, if we start from a rest period towards a charge/discharge phase, the ESR measurement $R_{sc,meas}$ can be calculated as:

$$R_{sc,meas} = \frac{V_{sc} - V_{sc,oc}}{I_{sc}} \tag{3.2}$$

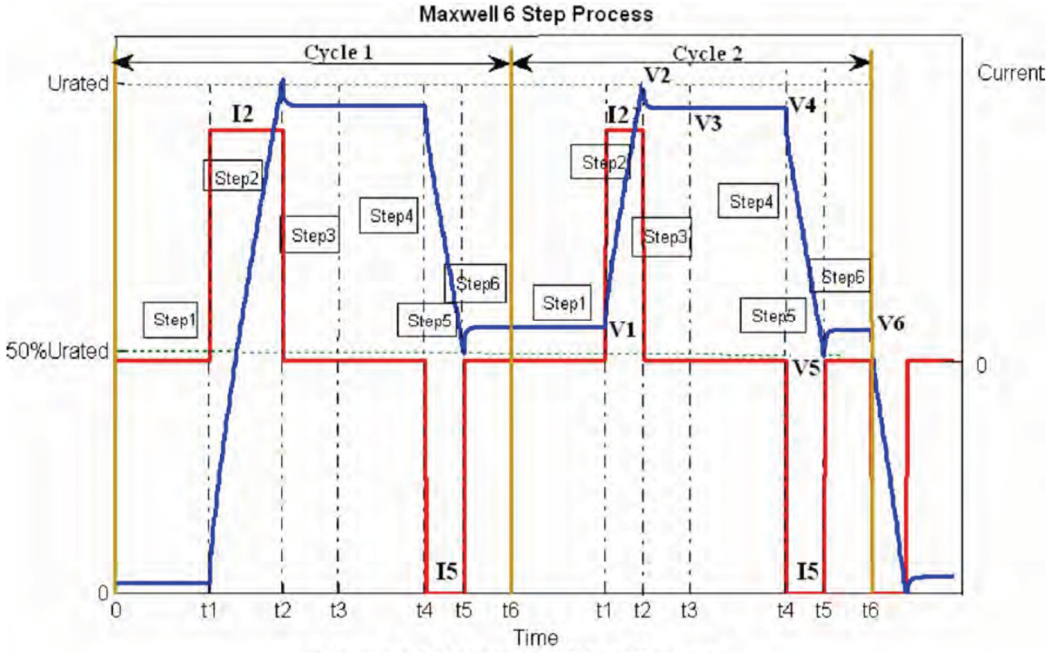

Fig. 3.4. The six-step capacitance and ESR measurement process of Maxwell Technologies [79]

where $V_{sc,oc}$ is the open-circuit voltage measurement and V_{sc} is the voltage measurement just after the application of the charge/discharge current I_{sc}. Both $C_{sc,meas}$ and $R_{sc,meas}$ measurement procedures are illustrated in Fig. 3.3.

According to Maxwell Technologies, one of the well-known supercapacitor manufacturers, characterization procedures of the capacitance and the ESR for DC applications depend on four factors. These are (i) the manner of charge and discharge of the supercapacitor; (ii) the choice and length of time of holding the voltage or opening the circuit during the period between charge and discharge; (iii) the starting and end voltages for the charge and discharge; and lastly, (iv) the timing of the measurements. With regard to the second factor, holding the voltage at a specific level provides a higher capacitance measurement, as is charging slowly. This is due to ions penetrating into deeper electrode pores during a slow charge. Maxwell proposes to open the circuit during the rest in between charge and discharge. About the third factor, the voltage levels must take into account the rated operational voltage range of the supercapacitor [79]. Considering the issues just discussed, Maxwell as a manufacturer has its own six-step capacitance and ESR measurement process, shown in Fig. 3.4.

The test profile Maxwell uses, shown in Fig. 3.4, has two cycles. Only the second cycle data are used because the first cycle is treated as an initialization cycle. The parameter values calculated from the first cycle data will be different from the succeeding cycles. Each cycle starts with a rest of 10 s until t_1, after which the supercapacitor is charged with a constant current until supercapacitor voltage reaches

Table 3.1. Test parameters defined by different standards [64]

Standard	Hold method	Hold time	Charge current	Discharge current	Referent voltages	
					$V_{\text{meas},1}$	$V_{\text{meas},2}$
Maxwell	Open circuit	15 s	100 mA/F	100 mA/F	$V_{C\text{sc,max}}$	$0.5V_{\text{max}}$
IEC 62391	Open circuit	30 min	75 mA/F	75mA/F	$0.8V_{\text{max}}$	$0.4V_{\text{max}}$
IEC 62576	Constant voltage	300 s	Specified for min. η = 95%	Specified for min. η = 95%	$0.9V_{\text{max}}$	$0.7V_{\text{max}}$
EUCAR	Constant voltage	30 s	50 mA/F	5 mA/F	$0.6V_{\text{max}}$	$0.3V_{\text{max}}$

V_{max} at t_2. The circuit is then opened, and the supercapacitor enters another rest period, but this time for 15 s until t_4. The supercapacitor is then discharged with a constant current until the voltage reaches $V_{\text{max}}/2$ at t_5. Then, the circuit is again opened for 5 s until the end of the cycle at t_6. Based on this test profile, it is possible to calculate the capacitance and the ESR from either the charging phase or the discharging phase. Maxwell uses the following formulas to calculate the parameter values:

$$C_{\text{sc,meas}} = C_{\text{dch}} = \frac{I_5(t_5 - t_4)}{V_5 - V_4}$$
$$R_{\text{sc,meas}} = R_{\text{dch}} = \frac{V_5 - V_6}{I_5} \tag{3.3}$$

where C_{dch} is the calculated capacitance for the discharge phase, R_{dch} is the calculated ESR for the discharge phase, and the subscripts of measured current and voltages correspond to the time of measurement (e.g. I_5 at t_5). It can also be seen in Fig. 3.4 that V_4 is the voltage level reached after the circuit was opened at t_2 (when V_{max} was reached). In the *RC* model, there is no voltage across the ESR when there is no current, V_4 can thus be regarded as purely the voltage across the capacitor $V_{C\text{sc,max}}$. The calculated values from (3.3) are what appear on the datasheets of Maxwell-manufactured supercapacitors [79].

It should be noted that the six-step capacitance and ESR measurement process just discussed was designed by a manufacturer and was thus optimized for the production line environment. For example, Maxwell does away with the holding period between charge and discharge making the whole process more efficient. Measurements can also be done from low to high current for small cells to large modules [79]. This measurement process is just one of the various characterization methods available. There are other standards available for testing supercapacitors: IEC 62391, IEC 62576, and EUCAR. Table 3.1 summarizes the various test parameters of these standards [64]. The most notable difference

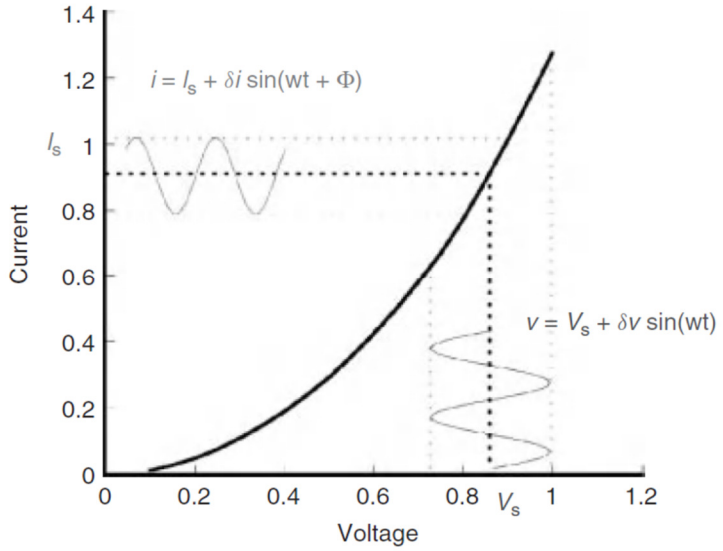

Fig. 3.5. Excitation with a single frequency at a given operating point: a sinusoidal voltage is imposed over the DC voltage and the resulting current is measured [14]

among the measurement protocols in the table are the hold time and the referent voltages. Referent voltages depend on the points at which measurements of the supercapacitor voltage are taken, as in Fig. 3.3(b). Because of the way C_{dch} is calculated in (3.3) and Fig. 3.4 using V_4 measured at t_4 when the discharge current turns on instead of waiting just a short time after the almost vertical fall of the voltage as in Fig. 3.3(b), it is possible that Maxwell underestimates the capacitance, though only by a negligible amount. As discussed, the resistance measurement takes advantage of this transition from open circuit/hold to discharge/charge, as in Fig. 3.3(a) and the formula for $R_{\text{sc,meas}}$ in equation (3.3). The small discharge current of 5 mA/F specified by the EUCAR standard thus presents a problem and will require increased measurement accuracy [64].

All the standards in Table 3.1 fall under a particular type of characterization method: constant-current charge/discharge (CCCD). CCCD methods take advantage of the constant-current charge/discharge and the resulting potential drop once current stops, as in Fig. 3.3 [37], [80]. They are considered to be versatile and accurate. From (2.2), (3.2), and V_{sc} for example, it is possible to derive other relevant properties like the time constant, power and energy densities, and leakage and peak currents. A cell's cycling stability can also be investigated. In addition, an experimental setup can be modified to become a three-electrode test where the specific capacitance, reversibility, and potential window can all be obtained [37].

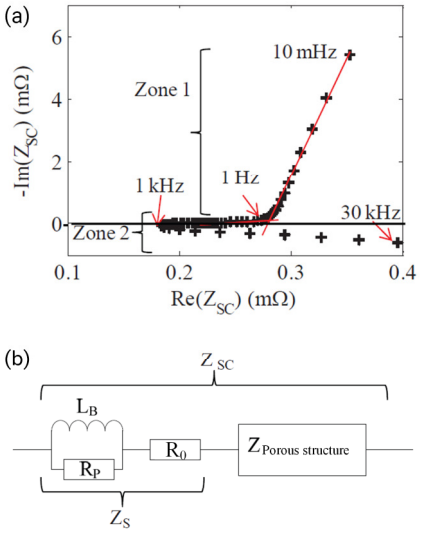

Fig. 3.6. (a) Typical Nyquist plot of the impedance response of a supercapacitor cell from 10 mHz to 30 kHz and an (b) Equivalent circuit model of the impedance response [83]

3.2.3 Frequency-Domain Characterization

The behavior of a supercapacitor can be characterized by its current response to the voltage changing in time (and vice versa). An AC voltage induces an AC current in the supercapacitor, which as said, also works the other way. For example, the response of an ideal capacitor with capacitance C is described by its impedance $Z_C = -\frac{j}{\omega C}$, where $j^2 = -1$, $\omega = 2\pi f$ is the angular velocity, and f is the frequency. In fact, impedance measurement using an AC current at a defined frequency has become one of the standard characterization methods usually employed for electrochemical devices like supercapacitors [14], [37], [38]. This method, called electrochemical impedance spectroscopy (EIS), measures impedance as a function of frequency. Its principle is illustrated in Fig. 3.5. A low amplitude AC voltage (< 10 mV), superimposed on a DC voltage, is used to bias an electrochemical device. Impedance is then calculated from the measured current signal and the AC voltage signal. The use of small signals permits assumption of linear current-voltage characteristics. On the other hand, a sweep of different frequencies allows us to capture the supercapacitor response for a large timescale from microseconds to hours. Results are usually presented in a Bode plot to show the impedance and phase angle as a function of frequency or in a Nyquist plot to show impedance on a complex plane [37].

The physical device construction of a supercapacitor cell was first described in Subsection 3.2.2. Recall that it consists of two porous carbon electrodes (typically activated carbon particles) that are separated by a liquid electrolyte composed of a salt dissolved in an aqueous or organic solvent [81]. The electrochemical behavior of the device is characterized by its impedance response. A typical Nyquist plot of the supercapacitor impedance response is shown in Fig. 3.6(a). Meanwhile, we have in Fig. 3.6(b)

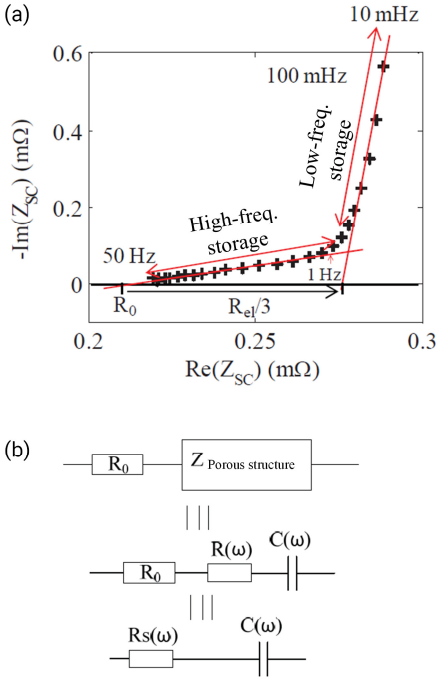

Fig. 3.7. (a) Zoom-in view of zone 1 of the supercapacitor impedance response and (b) Simplification of the equivalent circuit model of the impedance response in the frequency range of the porous structure energy storage [83]

an equivalent circuit model for the impedance response. Looking at Fig. 3.6(a), two distinct regions of the response curve are marked by zones 1 and 2. Since the imaginary axis is inverted, zone 1 is of a capacitive type of energy storage. On the other hand, we have zone 2 on the positive imaginary axis corresponding to an inductance produced through the rolling or folding of the electrodes and the contacts. This inductance is represented in the equivalent circuit model in Fig. 3.6(b) as the inductor L_B. The finite slope of the curve in the high-frequency region as seen in Fig. 3.6(a) is characteristic of a parallel parasitic resistor activating in high frequencies. This parallel resistor corresponds to the resistance R_p in Fig. 3.6(b) that is generated by the skin effect. On the other hand, the resistance R_0 constitutes the model for the contacts and is therefore present in the whole frequency range. These three components (L_B in parallel to R_p and in series with R_0) form the series impedance Z_s of the supercapacitor impedance Z_{sc} [82], [83].

As previously mentioned, zone 1 of the impedance response is capacitive in nature and this behavior is what we are concerned about when we talk of supercapacitor energy storage. We are thus interested in the aging behavior of this region for the determination of supercapacitor aging. Fig. 3.7(a) shows a zoomed-in view of zone 1 of the supercapacitor impedance response. It can be seen that even within the region of zone 1, the curve can be further subdivided into two subregions of different slopes: the high- and low-frequency storage subregions. The high-frequency subregion, called the high-

frequency storage, corresponds to the gradual entry of ions into the pores. As frequency decreases, ions travel a greater distance inside the pores increasing the resistive path traversed by the ions. Thus, the resistive part of Z_{sc} increases with a decrease in frequency. The other subregion, called the low-frequency storage, has a much steeper slope. This comes from the fact that ions travel entire pore lengths for very low frequencies and they accumulate inside the porous structures. This is accompanied by a drastic increase in the imaginary part of the Z_{sc}. The slope of the low-frequency storage is not infinite (which is the case for an ideal capacitor) because pore size is not uniform accompanied by slow charge redistribution. Because of this, the capacitance becomes dependent on the frequency and the electrode resistance increases in the subregion of low-frequency storage [82], [83].

For zone 1, all parasitic behavior at high frequency can be represented by a series resistance R_0 encapsulating all resistive phenomena not related to porosity (matter transport, contact quality, collector property, etc.). We see this resistance R_0 in Fig. 3.7(b). In the low frequency storage subregion, the impedance of the porous structure can simply be considered a frequency-dependent capacitance $C(\omega)$ in series with an also frequency-dependent resistance $R(\omega)$. We can therefore do the simplification in Fig. 3.7(b) resulting in the macroscopic RC model $Rs(\omega)$ in series with $C(\omega)$. The following equations describe their relationship to the supercapacitor impedance Z_{sc} [82], [83]:

$$\begin{aligned} Rs(\omega) &= \mathrm{Re}[Z_{sc}(\omega)] \\ C(\omega) &= -\frac{1}{\mathrm{Im}[Z_{sc}(\omega)]\omega} \end{aligned} \tag{3.4}$$

As a function of frequency, the low-frequency storage subregion is characterized by an almost constant capacitance and a decrease in resistance. This shows that charges accumulate throughout the porous structure of the activated carbon and the influence of charge redistribution. On the other hand, the high-frequency storage subregion is characterized by a steep decline in both $C(\omega)$ and $Rs(\omega)$ demonstrating the difficulty for pores to penetrate the porous structure.

While a Nyquist plot shows the impedance response on the complex plane (Fig. 3.8(a)), a Bode plot can show the same as a function of frequency (Fig. 3.8(b)). Fig. 3.8 shows the response of one of the 25-F supercapacitor cells used in the experiments. It was obtained through EIS characterization using the Zahner-Elektrik IM6 electrochemical workstation with a PP240 booster module. As said in Subsection 2.2.2, the operational SoE range is usually limited to 25% to 100%, so characterization was obtained at $SoE = 62.5\%$ ($v_{sc} = 2.13$ V), which is the midpoint of the SoE range. The response in Fig. 3.8(a) goes from the negative half-plane (with $-\mathrm{Im}(Z)$) and traverses the real axis to the positive half-plane (with $\mathrm{Im}(Z)$) as frequency increases. The point where the response crosses the real axis is purely a real number and thus, the supercapacitor exhibits a purely resistive behavior here. Below this point,

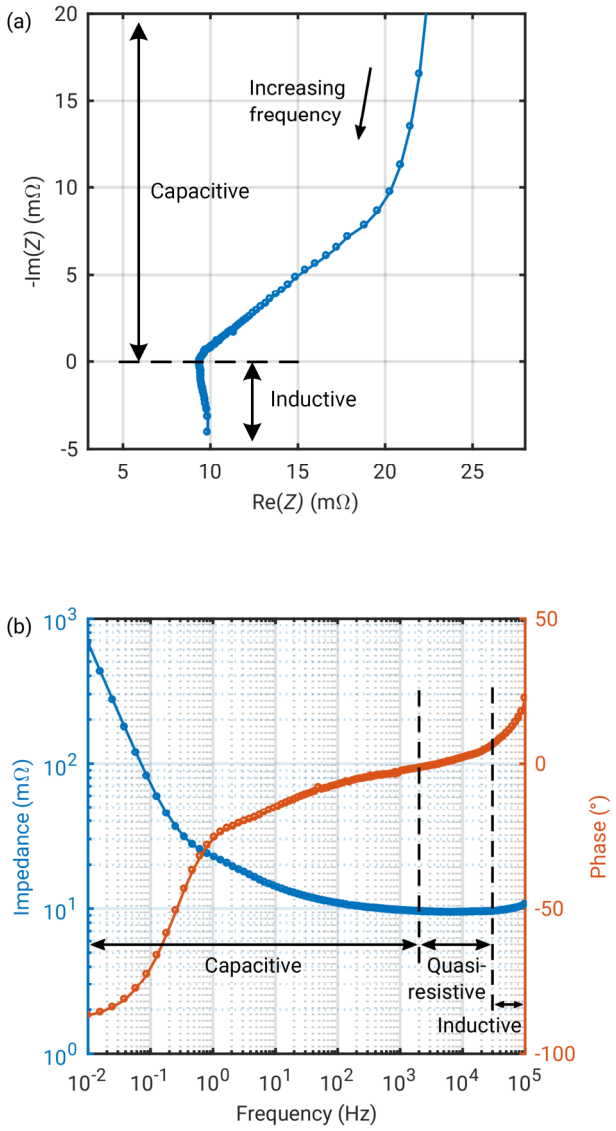

Fig. 3.8. Impedance response of a 25-F Maxwell BCAP0025 supercapacitor from 10 mHz–100 kHz at SoE = 62.5% (v_{sc} = 2.13 V) represented in a: (a) Nyquist plot and a (b) Bode plot

the supercapacitor displays inductive behavior. The frequency at which this occurs is referred to as the resonance frequency [40], [84]. The preceding discussion shows that practical supercapacitors exhibit inductive behavior in high frequencies [40], [84], [85]. The dependence of supercapacitor behavior on frequency can more clearly be seen in the Bode plot of Fig. 3.8(b).

The value of the resonance frequency can easily be obtained from the phase plot in Fig. 3.8(b). This is the resonance frequency point, which is 4.67 kHz for the considered supercapacitor, and where the phase has a value of zero and the resonance frequency impedance R_0 = 9.41 mΩ. As previously remarked, the resonance frequency demarcates the three possible supercapacitor behaviors: below this

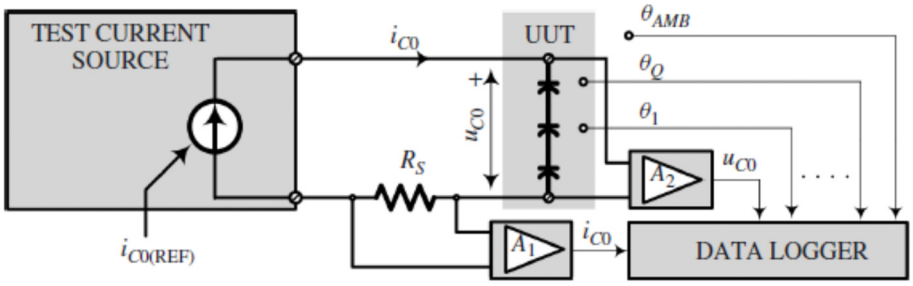

Fig. 3.9. A practical CCCD experimental setup [64]

frequency, the supercapacitor is mostly capacitive; at the resonance frequency, purely resistive; and below this frequency, mostly inductive. However, as Fig. 3.8(b) shows, the resistive behavior more or less extends to a range given the fairly constant impedance and phase for a span of frequencies. We could thus say that the behavior is quasi-resistive for this frequency range. If we limit the variation to within 1% of R_0, then the quasi-resistive behavior could be said to span the frequency range from 2 to 30 kHz for the considered supercapacitor, which can be seen to have been demarcated in Fig. 3.8(b) [40]. The resonance frequency impedance R_0 corresponds to the ESR. It is interesting to note in Fig. 3.2(b) that the frequency range where the supercapacitor exhibits quasi-resistive behavior remains the same even with aging [40]. This means that we can choose one specific frequency within this range where we characterize supercapacitor cells.

3.3 Online characterization

In this section, we review the difficulties of using the standard characterization methods discussed in the previous section in actual applications and present an online characterization method that is not only easy to implement but is also accurate.

3.3.1 Conventional Characterization Methods

In the previous section, we talked about two standard characterization methods: CCCD and EIS. We framed their use in terms of the domain for which they are mostly used. CCCD characterization is mostly based on the time domain, while EIS is based on the frequency domain.

As previously discussed in Subsection 3.2.2, a CCCD test involves biasing a supercapacitor in order to realize the specific test profile of a measurement method or standard being followed. In order to do this, a test source supplies the supercapacitor, as the device under test (DUT), with the current that charges/discharges it [64]. In a practical experimental setup such as in Fig. 3.9, a programmable two-quadrant power supply that can source and sink current is used as a test source, along with data-logging equipment that records current and voltage measurements together with other relevant physical

variables. Equipment programmability ensures that the supply can be controlled to follow the specific test profile of the measurement method or standard in use.

As regards EIS, the experimental setup is practically the same as the one used for a CCCD test with the exception that the test source be able to supply ac signals. It was mentioned back in Subsection 3.2.3 that an AC voltage superimposed on a DC voltage is used to bias a supercapacitor as the DUT. The AC current response is then measured. When a setup uses this mode, it is said to be in quasi-potentiostatic mode. Again, the prefix denotes that the mode is "almost" potentiostatic mainly because of the use of small AC signals, which, by nature, are not static. Instead of an AC voltage signal, it is possible to use an AC current superimposed on a DC current and measure the AC voltage response of the DUT. This is called the quasi-galvanostatic mode [86].

Before the advent of frequency response analyzers, AC bridges, lock-in amplifiers, and even oscilloscopes were used to obtain EIS data [86], [87]. AC bridges, specifically the Wien bridge which builds on the classical Wheatstone bridge, are used for impedance measurement. They work by putting the DUT in one arm and adjusting the other arms to null the bridge. They basically compare unknown DUT values to known values. Measurements are precise, but the process is laborious and time-consuming because the process has to be repeated for each frequency in question [87]. On the other hand, lock-in amplifiers work through phase-sensitive detection. A signal is mixed with a square reference signal twice: the first time with the original reference signal and the second time with the same reference signal shifted by 90°. This allows extraction of real (in-phase) and imaginary (out-of-phase) parts of the signal. Any signal that is not at the same frequency as the reference signal is attenuated. The process can be applied to the measured signal (whether current or voltage) to obtain its corresponding complex number that can then be processed together with the bias signal to calculate the impedance response [87].

While equipment can be built out of lock-in amplifiers, they are limited from use in low frequencies. Oscilloscopes suffer the same problem. Thus, frequency response analyzers came to be the most commonly used equipment in doing EIS [86]. Instead of a square reference signal, the reference signal that is mixed with the measured signal in a frequency response analyzer come in the form of sinusoidal signals. The same principle of a 90° phase shift governs regarding the cosine and sine reference signals. Integration of the mixed signals corresponds to their Fourier transforms producing the real and imaginary parts of the measured signal. Again, like in the lock-in amplifier case, the same process can be done for both the measured and bias signals from which the impedance response can be obtained. Frequency response analyzers can do a faster analysis over a wider frequency range compared

to the lock-in amplifier. However, these advantages come at a higher cost and at a more limited sensitivity [87].

3.3.2 An Online Characterization Method

It should be clear from the discussion in the previous subsection that conventional methods of characterizing supercapacitors are limited. First, it is impossible to characterize a supercapacitor while in use in an application. Fig. 3.9 shows that a supercapacitor as a DUT has to be connected to a test source whether the characterization is CCCD- or EIS-based. The supercapacitor must be disconnected first and then removed from the application before characterization is possible. Second, the test source itself is a separate equipment that is usually stationary in a laboratory setting. There is thus a need for online methods that allow for characterization without the need for the supercapacitors to be removed from the application.

One popular online characterization method is through observer-based control. Observers are algorithms that take advantage of knowledge of a system, the power conversion mechanism, and the sensor itself in addition to the sensor signals measured for control of the system. The resulting observed feedback signal is thus superior to that coming directly from the sensor. Observed signals can have the advantage of being more accurate. Because of the reduced need for sensors, they can also be cheaper and more reliable than sensed signals thus enhancing performance. However, implementation of observers add to a system's computational complexity and requires more overhead. The characteristic software control loops can also be a source of instability under certain conditions [39]. A cost-benefit analysis is therefore necessary not only in the selection of the observer technique but more broadly in the practicality of use of observers in a particular application. As an online supercapacitor characterization method, observers are suitable in representing SoH and RUL (through ESR and capacitance) as observed signals precisely because they are not directly measurable by sensors. Their observability is only possible through voltage and current measurements of the supercapacitor, quantities that can be directly sensed [88]–[90]. However, accuracy of observed signals against standard characterization methods like EIS varies depending on the observer technique used and the system model construction.

It is also possible to integrate ESR measurement with a passive or resistive balancing circuit. In which case, the resistors that dissipate charge from supercapacitor cells are controlled by a square wave with a frequency within the quasi-resistive range. This ensures that the response of the supercapacitors will be an impedance that is within the said range, i.e., the resonance frequency, which was shown to correspond to the ESR of Maxwell supercapacitor cells under test in Subsection 3.2.3. The ESR can then be taken to calculate cell's individual SoH and RUL [40]. This work shows another direction in terms

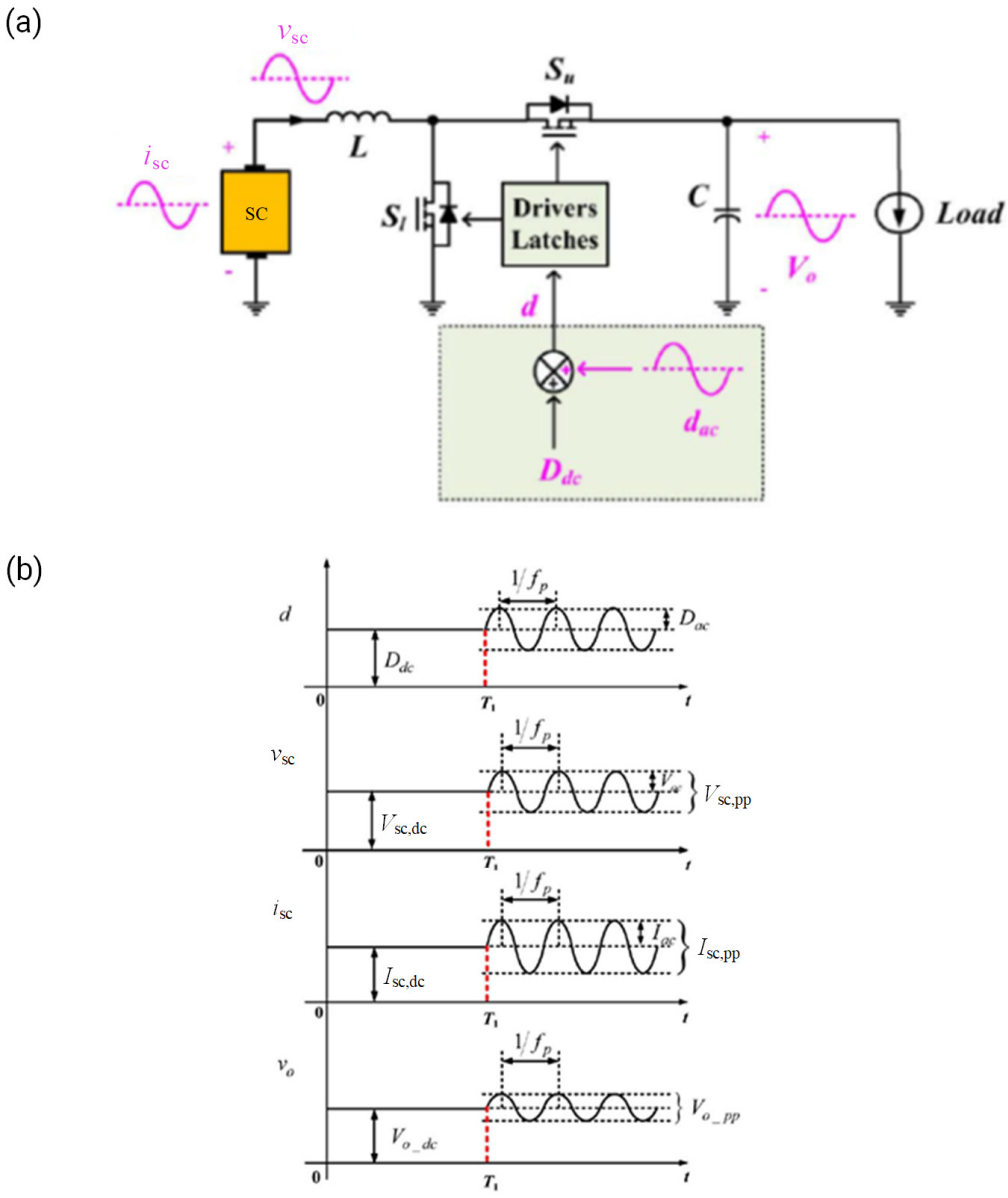

Fig. 3.10. Online supercapacitor characterization: (a) Inducing an impedance response using a small ac signal injected into the duty ratio of the nonisolated bidirectional dc-dc converter and (b) Measurements [41]

of online characterization that capitalizes on the system architecture, specifically on a component system (balancing circuit) in order to achieve another purpose on top of the original one for the component system.

Another line concerning online characterization methods works through the control of a DC-DC power converter connected to an electrochemical device. This method was previously demonstrated in the online measurement of the impedance of batteries [41], [42]. Considering the system of Fig. 2.2 comprising modular power converters interfacing energy storage with an application, we propose to use the same method for supercapacitors. As in conventional EIS in Fig. 3.5, there is a need to excite the

supercapacitor with a small AC signal at a certain frequency in order to solicit a response. This perturbation in our system comes from the addition of the small signal into the control of the modular power converters through the duty ratio D_j. It is expressed in the supercapacitor response as perturbed voltage and current signals, from which the supercapacitor impedance at the test frequency can be calculated. The proposed method is shown in Fig. 3.10(a) with the expected measurements in Fig. 3.10. (b). As previously discussed in Subsection 3.2.2, supercapacitor response is quasi-resistive for a range of frequencies. Within this range, $C_{sc} \cong 0$ and the ESR can be approximated as the resonance frequency impedance R_0. ESR itself can be calculated from specific points in the voltage and current signals:

$$ESR_{meas} = \frac{V_{sc,pp}}{I_{sc,pp}} = \left|\frac{v_{sc,max} - v_{sc,min}}{i_{sc,max} - i_{sc,min}}\right| \tag{3.5}$$

where the "max" and "min" in the subscripts denote the maximum and minimum values of the variable (voltage or current), respectively, within a single period. Even though the signals in Fig. 3.10(b) are periodic, there are always errors in measurement, so a number of periods have to be considered where Eq. (3.5) is applied to obtain an averaged more precise value for the ESR.

3.4 Experimental Results

The online characterization method in Subsection 3.3.2 was experimentally implemented on the small-scale 30-W system with three modular converters. This section discusses validation of the method through the experimental setup and the results.

3.4.1 Experimental Setup

We used the same experimental setup as in Fig. 2.14, which was first described in Subsection 2.5.1. As Fig. 3.10. (a) shows, a small AC signal d_{ac} has to be added to the duty ratio D_j. This was easily done to the control system in Fig. 2.2(b) that was programmed into the target machine using MATLAB and Simulink.

It was mentioned back in Subsection 3.2.3 that the quasi-resistive range of 25-F Maxwell BCAP0025 supercapacitors is from 2 kHz to 30 kHz. The frequency of d_{ac} should thus be within this range. However, the small-scale prototype has a 10kHz sampling frequency. If we set d_{ac} to be at 2 kHz, there will only be five samples for a single period. This is vastly inadequate and substitution of the measurements in equation (3.5) will result in inaccurate ESR values. There is thus no choice but to settle for a much lower frequency. Among the possible frequencies, 250 Hz in the lower end of the range was chosen in order to capture enough samples of the supercapacitor response with the 10 kHz sampling frequency of the mock-up. At this perturbation frequency, 40 supercapacitor voltage and current samples

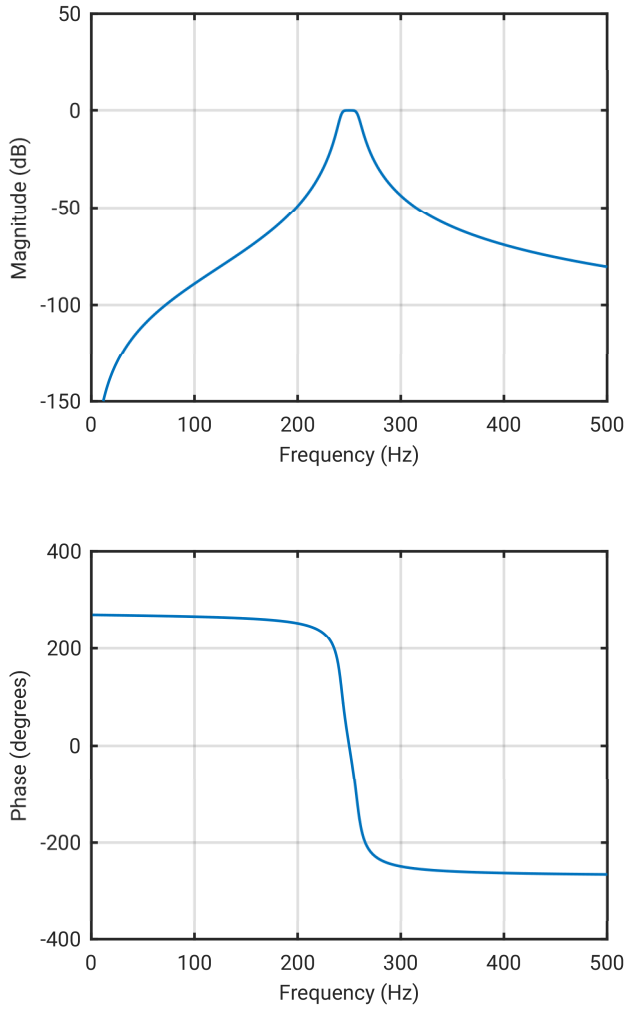

Fig. 3.11. Bode plot of the sixth-order Butterworth bandpass (240–260 Hz) filter used to filter the noisy voltage signal.

can be obtained within a single duty ratio perturbation that allows retention of important response characteristics in the signals. This choice also leads to a systemic error of ~9% when compared to EIS characterization data obtained using the Zahner-Elektrik IM6 electrochemical workstation. With regard to the capacitance at this frequency, if we use $Z_C = \frac{1}{j\omega C_{sc}}$, we will get $C_{sc} = 0.68 \ll 25$ F, which is the nominal capacitance. This means that we are still close to the quasi-resistive range.

To accommodate the 250-Hz frequency, the filter was specified to be a passband from 240 to 260 Hz (with at most 1 dB passband ripple) with stopbands of below 50 Hz and above 450 Hz (with at least 50 dB attenuation in the stopbands). It was found that a sixth-order digital Butterworth filter satisfies the specifications using the MATLAB command for finding the lowest order. The filter's Bode

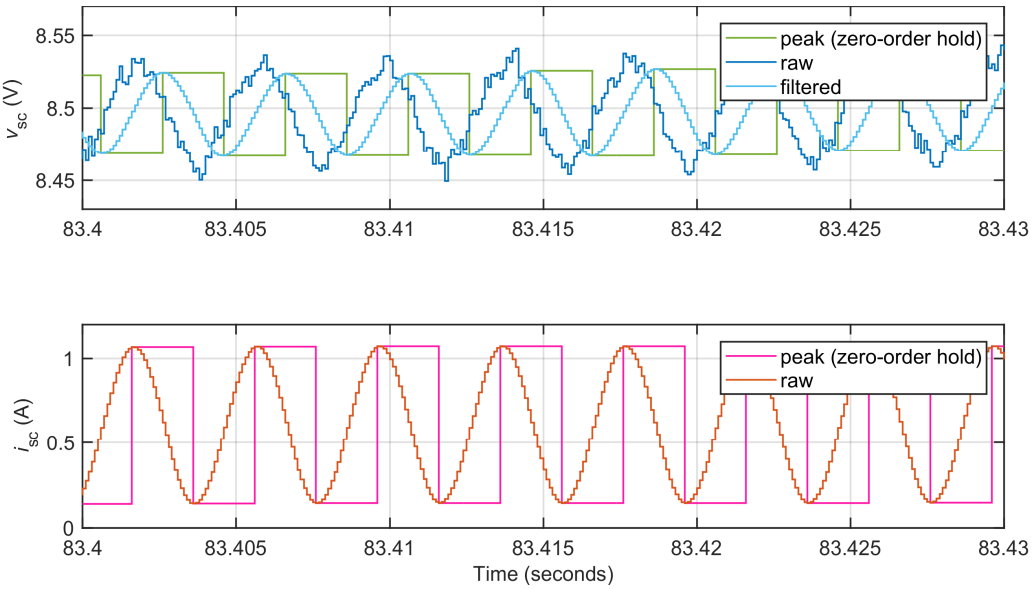

Fig. 3.12. Measured voltage and current signals using the online characterization method

plot can be seen in Fig. 3.11 and it was used for the measured voltage signal. To account for systemic errors, measurements using the online method were compared to an oscilloscope's. Oscilloscope probes were hooked to pins on the motherboard (refer to Subsection 2.5.1 for the discussion of the experimental setup) to have its measurement points as close as possible to the voltage and current sensors used by the prototype. Since the application of the experimental setup is for the accelerated aging of supercapacitors, some measurements were done with wires connected between motherboard where the converter switches are and the daughterboard (cf. Subsection 2.5.1) where the supercapacitors are soldered.

3.4.2 Experimental Results

Following the discussion so far, we see in Fig. 3.12 a sample of measured voltage and current signals. It can be seen that the raw voltage signal is noisy and thus the need for filtering. The sixth-order digital Butterworth filter described in the previous subsection was used this purpose. In addition, while there is no noticeable phase shift between the raw voltage and current signals, the same is not true for the filtered signal. It is thus the filtered signal that is used in determining the maximum and minimum values within periods. In the figure, these values are represented as zero-order hold (ZOH) signals. Calculating the ESR then is just a matter of applying equation (3.5) to the ZOH voltage and current signals. The small AC signal d_{ac} was applied for 5 s and the ESR values obtained for each period within this duration were averaged to obtain a mean ESR value.

Table 3.2. Comparison of ESR measurements between the prototype and oscilloscope

Supercapacitor	SC impedance measured at motherboard terminals by oscilloscope (mΩ)	SC impedance measured at motherboard terminals by prototype (mΩ)
Group	107.	117
Cells 1–4	26.8	29.2
		Error: 8.92%

Table 3.2 shows a comparison between ESR results obtained through the online characterization method as implemented in the small-scale prototype and ESR values obtained through oscilloscope measurement. It can be seen that there are four cells in a group connected to each daughterboard. However, measurements are done only at the motherboard terminals or pins, so what was obtained was the sum. It was not possible to obtain results for each cell. The error in measurements is 8.92%.

3.5 Conclusion

This chapter presented how supercapacitors are characterized. We presented characterization methods in two domains: time and frequency. We proceeded to discuss what parameters can be obtained from each method and how they are represented. The conversion of results between domains was also tackled. Characterization is important for determining supercapacitor SoH and estimating RUL. We then proceeded to discuss how these laboratory methods are inadequate in actual applications and presented an online method, which we have shown through a validation experiment to work and to be accurate enough for our purposes. This online characterization method will be used in the next chapters in determining the relevant supercapacitor parameters for diagnosis and prognosis.

Chapter 4

Optimizing Supercapacitor System Life

4.1 Introduction

Supercapacitors, otherwise called electrical double-layer capacitors (EDLC), have much higher charge storage capability compared to capacitors. Unlike usual capacitors, there is no dielectric separating the electrodes of supercapacitors. An electrolyte fills the space between the electrodes. The electrical double layer (EDL) refers to the two charged layers formed at the electrode-electrolyte interfaces. The high charge storage capability, manifested in the capacitance, is due to the large surface area of activated carbon used in the electrodes and the extremely thin distance between the double layers [10], [37], [78]. Compared to batteries, much higher charge-discharge cycles and therefore, longer lifetimes are possible with supercapacitors [10].

As mentioned back in Sections 2.1 and 3.1, there is a natural tolerance to the parameters of the supercapacitors as a result of uneven manufacturing processes [11], [14]. In the endurance test of the Hybus project, which was first introduced in Section 2.1and which aimed at the recovery of the braking energy of trolleybuses for storage in a stack of supercapacitors, the difference between the hottest and coldest temperatures in a supercapacitor stack could be as high as 36 °C. The endurance test was meant to approach real supercapacitor usage conditions in order to anticipate possible challenges due to them and was essentially an accelerated aging test with power cycling. Fig. 4.1(a) shows the thermal image from the endurance test of the project [31], [43], [44]. Such an irregular temperature distribution leads to an uneven aging of supercapacitor cells over time. If we remember, it was mentioned that approximately every increase of 10 °C halves a supercapacitor's life [11]. This means that hotter cells will reach the supercapacitor end-of-life criteria first before colder ones. Ultimately, this leads to a

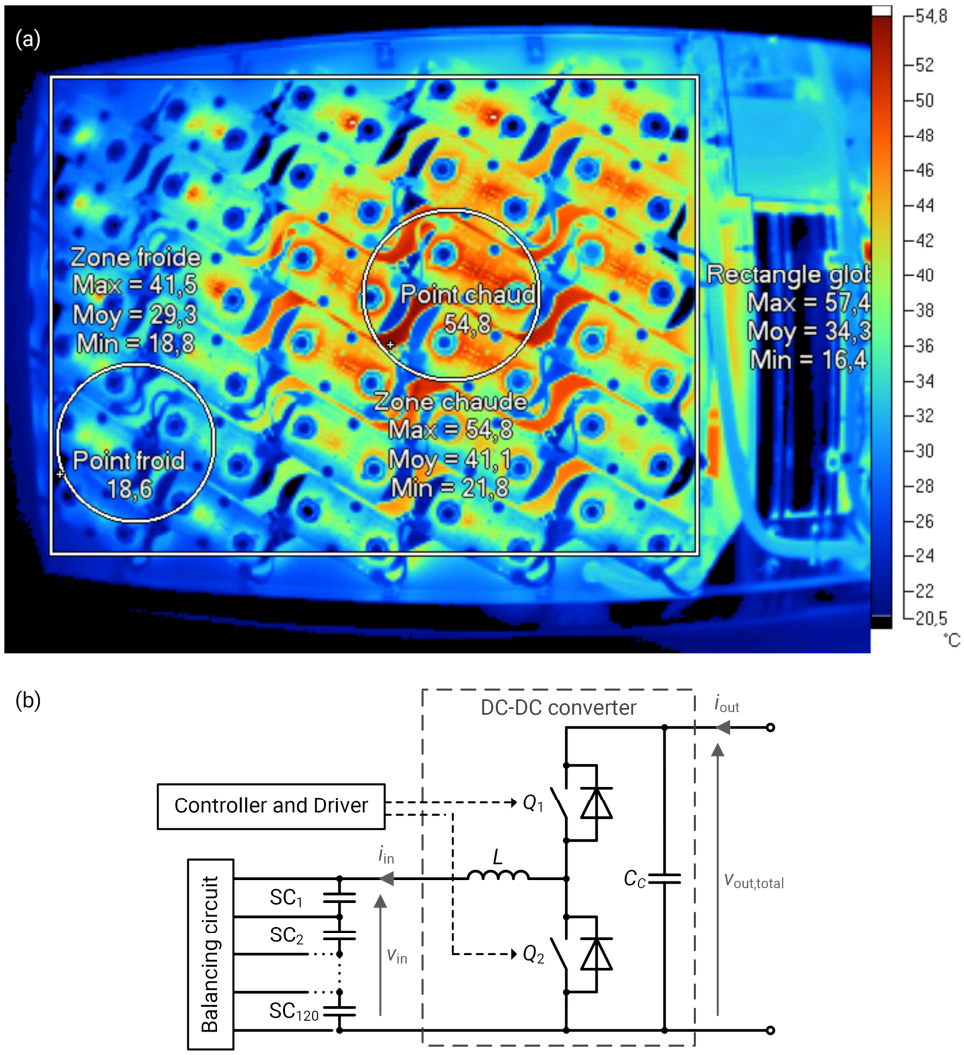

Fig. 4.1. Stack of 120 supercapacitors in the Hybus project: (a) Thermal image [43] and (b) Interfaced by a nonisolated bidirectional DC-DC converter.

shorter system lifetime, which means lower overall system reliability. There is thus a need for a balancing system that can minimize the imbalance in aging by biasing the supercapacitors according to their states of health (SoH).

4.2 Controlling Aging

The system in the Hybus project serves as the basis for the system considered in the first half of this chapter. The project aimed to have supercapacitors as auxiliary supply during power cuts in the operation of trolleybuses. Supercapacitors were the energy storage device of choice because of the power requirement of the application. They supply energy during the power cuts, and recharge and recover energy when the trolleybus brakes. The study involved dimensioning the supercapacitors and

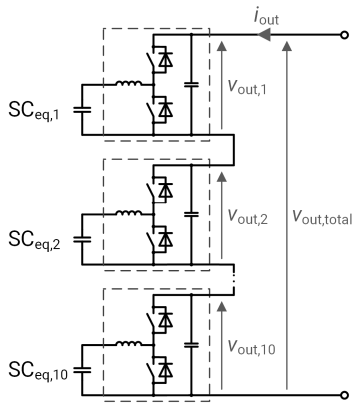

Fig. 4.2. 120 supercapacitors grouped by ten modular buck-boost converters.

designing the power electronics considering the power requirements and the conditions under which the system operated [31], [43], [44].

In the Hybus project, 120 supercapacitors with a total voltage varying from 120 to 300 V depending on the charge stored in the stack were connected to a nonisolated bidirectional DC-DC converter whose output was regulated at $v_{\text{out,total}} = 350$ V. The system is shown in Fig. 4.1(b). In light of minimizing the imbalances among the cells through balancing circuits to extend the system life, the interesting approach of partitioning the single DC-DC converter into smaller modular ones arises. The 120 supercapacitors were grouped by ten and the groups with 12 cells each are connected to smaller converters whose outputs are connected in series. Fig. 4.2 illustrates such partitioning where $SC_{eq,j}$ is the equivalent supercapacitor of 12 cells. As discussed in Subsection 2.4.1, this choice of grouping was made in consideration of the thermal behavior of a supercapacitor stack with Fig. 4.1(a) as an example. While the ideal case would have each cell connected to its own converter, this is simply not tenable against costs. Thus, great flexibility in control that is possible with the ideal case had to give way to practical considerations. Anyway, the thermal homogeneity of each group served as basis for the groupings through a thermal model of the supercapacitor stack [31].

Where does balancing to maximize the lifetime come into the picture? As in the single-converter system of Fig. 4.1(b), the output voltage $v_{\text{out,total}}$ of the system in Fig. 4.2 is regulated. While evenly dividing the load of the single converter into ten achieves modularity and has reliability benefits in itself, we can further take advantage of the new architecture by considering the parameters crucial to the aging of the supercapacitors, namely voltage, current, and temperature. These, on the other hand, are coupled to the output voltages and currents according to the operational characteristics of the converters. Since the converter outputs are connected in series, the same current flows through them. Thus, we can control the amount of power that goes into and out of the supercapacitor groups through the output voltages $(v_{\text{out},1}, v_{\text{out},1}, \dots, v_{\text{out},10})$ of the converters. The research problem in this chapter then is looking for the

optimal values of converter output voltages that maximize system lifetime while maintaining the regulation of the total output voltage.

The physical aspects of Fig. 4.2, namely supercapacitors, modular power converters, and control systems down to the dimensions, are the same as the ones first described in Section 2.2. Where they differ is in the control objectives. Subsection 2.3.4 fully described an energy-based voltage-balancing strategy used for such systems. The objective of this chapter, however, is optimizing supercapacitor system lifetime. Instead of a voltage-balancing strategy, a lifetime-balancing strategy will be developed for use in the same physical systems. More concretely, going back to Fig. 2.2(a), which showed the systems described in Section 2.2, the lifetime-balancing strategy will have to provide the reference $V_{\text{ref},j}$ to each of the converters that controls their output $v_{\text{out},j}$ such that supercapacitor system lifetime is optimized in the long term and that the regulation of $v_{\text{out,total}}$ is conserved.

As previously discussed, no matter the recent advances in manufacturing, there will always be variation in the initial characteristics of supercapacitors. The act of assembling cells in a stack will introduce another source of variation during operation as evidenced by the thermal image in Fig. 4.1(a) that shows nonuniform heating of supercapacitor cells. Over time, the initial and operational sources of variation in characteristics contribute to the nonuniformity of aging itself [11]–[13], [18]. Supercapacitor cells that have high voltage, current, and temperature levels age faster and will limit a system's lifetime by reaching end-of-life criteria first. Thus is there the necessity for balancing systems to reduce such dispersion [10], [11], [14]. Balancing is commonly integrated with other systems such as monitoring and management systems [10], [15].

As first discussed in Chapter 2, there are two types of balancing circuits: passive (or dissipative) and active (or redistributive) balancing circuits in the literature [91]. These two have fundamental differences in terms of circuits, control, and operation. Each has its own advantages and disadvantages as well. In passive balancing circuits, the excess charge in the cells is dissipated through resistors. This is the simplest and cheapest strategy to implement. On the other hand, active balancing circuits redistribute charge from overcharged to undercharged cells. We can see just from the balancing mechanisms that active balancing circuits are more complicated and thus, more expensive to implement. The advantage, however, is in their better efficiencies.

The latest approach in balancing is to use modular power converters. Its architecture is fundamentally different. Unlike in the previous circuits, power to the rest of the system is drawn from the output of the converter. The output voltage of converters can be controlled, and by doing that, we also control the power we draw from the individual cells [19], [20], [22]. Power converters have a long history of being used in interfacing energy storage devices. Their flexibility in terms of the architecture

and control lend themselves for use in electric vehicles and grid applications [22], [63], [92]. Their use for balancing energy storage devices was born out of the need to integrate more storage cells for more power.

Aside from the task of voltage regulation, the converters have to be controlled in such a way that the other task of balancing is achieved. Most of the algorithms do these two tasks by balancing the cells' SoCs [13], [16]–[19], [22], [24], [30], [30]. SoC indicates the remaining electricity available from a storage capacity. The total energy is shared among the converters such that when charging, cells with higher SoCs get charged less compared to cells with lower SoCs [20]. In many examples in the literature (commonly using batteries as energy storage), SoC balancing must be realized in tandem with another objective or in the context of more realistic conditions. For example, in an application where second-life batteries that have varying SoH's are incorporated into a system, SoC balancing can still be done, but system stability becomes a crucial factor. Control has to consider the individual SoHs of the batteries, but this has the effect of wide variations in the individual control bandwidths causing a stability problem. Thus, more robust control is needed because real systems are far more complex and other factors like temperature and aging are important as well during operation [10], [22], [23]. One other study looked into adding the third task of thermal balancing to ensure the uniform aging of battery cells [25]. In the case of supercapacitors, converters were designed for reduced inductor size and weight, and controlled for voltage balancing of the supercapacitors [30].

4.3 Control Allocation Based on Reliability Indicators

As mentioned, a modular system has reliability benefits. This has mainly to do with the maintenance and replaceability of components. Consequently, another advantage it brings for the system in Fig. 4.2 lies in redundancy. For example, when there is a fault in one of the converters, the rest can still function and shoulder the load. This assumes that the modular converters were initially oversized in anticipation of faults in order for the whole system to become fault tolerant. Controlling such a system with the express goals of fault tolerance and reliability is a difficult task.

For a general linearized system such as:

$$\begin{aligned} \dot{\mathbf{x}}(t) &= \mathbf{A}\mathbf{x}(t) + \mathbf{B}_u\mathbf{u}(t) \\ \mathbf{y}(t) &= \mathbf{C}\mathbf{x}(t) \end{aligned} \tag{4.1}$$

where $\mathbf{x} \in \mathbb{R}^n$, $\mathbf{u} \in \mathbb{R}^m$, and $\mathbf{y} \in \mathbb{R}^p$ are the state, control, and output vectors; $\mathbf{A} \in \mathbb{R}^{n\times n}$, $\underline{\mathbf{B}_u \in \mathbb{R}^{n\times m}}$, and $\mathbf{C} \in \mathbb{R}^{p\times n}$ are the state, control, and output matrices. Generally, control allocation is used for overactuated systems where the number of operable controls is greater than the number of controlled variables. The system in (4.1) is overactuated if $\text{rank}(\mathbf{B}_u) = k < m$. This means that $\mathbf{B}_u$ can be factorized

as $\mathbf{B}_u = \mathbf{B}_v\mathbf{B}$, where $\mathbf{B}_v \in \mathbb{R}^{n\times k}$ and $\mathbf{B} \in \mathbb{R}^{k\times m}$. The virtual control input is $\mathbf{v}(t) = \mathbf{B}\mathbf{u}(t)$, where $\mathbf{v} \in \mathbb{R}^k$. In general, it represents the total control effort by actuators. However, for the system considered in this thesis, it represents the total constraint of the supercapacitors. For simplicity, the assumption $k = p$ is considered. The control allocation problem can be expressed as the constrained linear mapping problem:

$$\mathbf{v}(t) = \mathbf{B}\mathbf{u}(t) \tag{4.2}$$

$$\mathbf{u}_{\min} \le \mathbf{u} \le \mathbf{u}_{\max} \tag{4.3}$$

where $\mathbf{u}_{\min}$ and $\mathbf{u}_{\max}$ in (4.3) are the saturation points or physical limits of the supercapacitors. Furthermore, in managing the redundant supercapacitors, we use a weighting matrix $\mathbf{W}_u$, which is based on their health or reliability. It is defined as:

$$\mathbf{W}_u = \begin{bmatrix} \frac{r_1}{r_{\max}} & 0 & \cdots & 0 \\ 0 & \frac{r_2}{r_{\max}} & \cdots & 0 \\ \vdots & \vdots & \ddots & \vdots \\ 0 & 0 & \cdots & \frac{r_n}{r_{\max}} \end{bmatrix} \tag{4.4}$$

where r_j is the reliability indicator taken as the baseline or nominal aging rate (λ_j^{bl} in s^{-1}) of the jth supercapacitor and $r_{\max}$ is the maximum among all the reliability indicators [45], [46].

In control allocation, the weighting matrix is used to allot the control input into the different supercapacitors. Maximizing the reliability of a system based on it is thus an optimization problem. Optimal control-based solutions are used to solve the control allocation problem in (4.2). They aim to look for the optimal solution, the best one if there many solutions, or the most feasible one if no exact solution exists. For example, the optimal solution can be solved using a two-step sequential quadratic programming:

$$\psi = \underset{\mathbf{u}_{\min}\le\mathbf{u}\le\mathbf{u}_{\max}}{\arg\min} \|\mathbf{B}\mathbf{u} - \mathbf{v}\|_2 \tag{4.5}$$

$$\mathbf{u} = \arg\min_{\mathbf{u}\in\psi} \|\mathbf{W}_u(\mathbf{u} - \mathbf{u}_{\mathrm{d}})\|_2 \tag{4.6}$$

where $\mathbf{u}_{\mathrm{d}}$ is the desired control input. If the constraint in (4.3) is not considered, the quadratic programming problem can be minimized into:

$$\begin{aligned} &\min_{\mathbf{u}} J = \|\mathbf{W}_u\mathbf{u}\| \\ &\text{subject to } \mathbf{B}\mathbf{u}(t) = \mathbf{v}(t) \end{aligned} \tag{4.7}$$

where an explicit analytic expression for the optimal solution can be obtained. This solution is based on the pseudoinverse method for control allocation and is given by:

$$\mathbf{u}^*(t) = \mathbf{W}_u^{-1}(\mathbf{B}\mathbf{W}_u^{-1})^+\mathbf{v}(t) \tag{4.8}$$

where the "+" sign in superscript is the pseudoinverse operator. The analytic nature of the optimal solution in the pseudoinverse method makes its application in many systems easy. While there is no guarantee that the solution is within the saturation points because the constraint was disregarded, there are methods to take care of it. In the redistributed pseudoinverse method, for example, saturated supercapacitors are removed from the optimization problem. The pseudoinverse formula is then just solved for the remaining unsaturated supercapacitors [45], [46].

To achieve the objectives according to the formulation of the problem in the previous section, Section 4.2, we employ a control allocation module that is separate from the task of regulation. Its implementation is easy with the formula for the optimal solution in (4.8). The previous discussion of the technique demonstrates that it considers the health of the components in the system and aims to improve overall system reliability.

Adapting the control allocation method using the pseudoinverse operator for our system in Fig. 4.2, the control input is $\mathbf{u}^*(t) = [V_{\text{ref},1} \quad V_{\text{ref},2} \quad \cdots \quad V_{\text{ref},10}]^{\text{T}}$ and, considering that $\mathbf{v}(t)$ represents all total control constraint by the supercapacitor, $\mathbf{B} = [1 \quad 1 \quad \cdots \quad 1]$, such that:

$$\mathbf{B}\mathbf{u}^*(t) = \mathbf{v}(t) = \left[\sum_{i=1}^{10} V_{\text{ref},j} = V_{\text{ref,total}}\right] = \left[V_{\text{ref,total}}\right] \tag{4.9}$$

where $V_{\text{ref},j}$ is the reference voltage (V) for the jth converter and $V_{\text{ref,total}}$ is the total reference output or bus voltage (V). Using the pseudoinverse method in (4.8) applied to the control of the modular power converters leads to the analytic formula:

$$V_{\text{ref},j} = \frac{V_{\text{ref,total}}}{w_j^2\left(\sum_{k=1}^{n}\frac{1}{w_k^2}\right)} \tag{4.10}$$

where $w_j = \frac{r_j}{r_{\max}}$, which is the diagonal element of (4.4). Use of (4.10) should result in supercapacitors with better health being loaded more and supercapacitors with less health being loaded less. Thus, to use this method to obtain the reference voltages needed to control the modular power converters, the reliability indicator for the weighting matrix based on the model for supercapacitor lifetime must be designed.

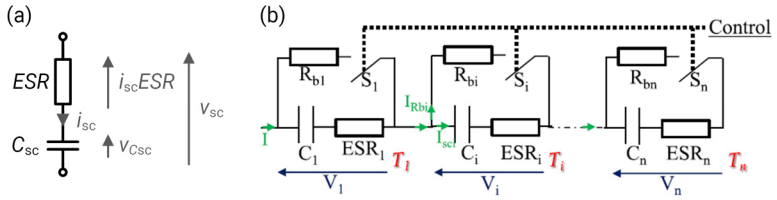

Fig. 4.3. (a) The macroscopic *RC* model of a supercapacitor and (b) the model used in a passive balancing circuit [47]

4.4 Application in Trolleybus Supercapacitor Auxiliary Supply

4.4.1 Supercapacitor Aging Model

The conventional goal of balancing circuits is to balance the SoC's of individual cells, or in the case of supercapacitors, to balance voltages [10]. These balancing circuits only approximately minimize aging. An altogether different approach was started in the Ampère laboratory by the work of Shili [47], [93]. She directly used a model for the lifetime of each cell to control a passive balancing circuit with the express goal of minimizing the aging imbalance and prolonging the lifetime of the whole system. This is the first time that instead of balancing SoC's, we are balancing SoH's. SoH is the parameter that indicates storage degradation in terms of capacity and power fade [94]. It tells us how much useful life is left.

Shili's work uses a lifetime model for supercapacitors which was also developed in the laboratory [12]:

$$\tau_{\mathrm{d}}(t) = \frac{\tau_0}{\frac{1}{T}\int_{t-T}^{t} \exp\left[\frac{v_{\mathrm{sc}}(t)}{V_0} + \frac{\theta(t)}{\theta_0} + \frac{i_{\mathrm{rms}}(t)}{I_{\mathrm{rms},0}}\right] \mathrm{d}t} \tag{4.11}$$

where τ_{d} is the dynamic lifetime (s); $v_{\mathrm{sc}}(t)$is the dynamic value of the voltage (V) across the supercapacitor; $\theta(t)$ is its dynamic temperature (°C); and $i_{\mathrm{rms}}(t)$ is the dynamic RMS current (A). V_0, θ_0, and $I_{\mathrm{rms},0}$ are constants that relate the latter three quantities to their effect on lifetime, while τ_0 is the theoretical lifetime for a supercapacitor at 0 V and 0 °C [43], [93].

In Fig. 4.3(a), we have the basic supercapacitor *RC* model, which is that of a capacitance C_{sc} in series with the supercapacitor's ESR. As a supercapacitor is used, its capacitance decreases and the ESR increases until its end of life. The usual end-of-life criteria are when a reduction of 20% is reached for a supercapacitor's capacitance or its ESR increases by 100% [36].

This model was used to propose a method of controlling the passive balancing circuit to prolong system lifetime. Dissipation of the shunt resistors in the circuit in Fig. 4.3(b) was controlled through finite control set model predictive control with the goal not to balance voltages or SoC's, but to balance the supercapacitors' SoH's instead. The novel method was compared to the classical voltage balancing strategy and was found to have extended lifetime by 23% more. For both strategies, the stack's lifetime was set by the cell that reached its end of life first.

4.4.2 Supercapacitor Remaining Life as the Reliability Indicator

In the general system considered in the previous section (cf. Section 4.3), a supercapacitor's aging rate served as the reliability indicator for the control allocation. There are many definitions for aging rate and specific ones depend highly on the components, systems, and conditions under consideration [45], [46].

In the system we are considering where the system of supercapacitors and modular converters are, in a general sense, redundant actuators, we take the inverse of the remaining life of supercapacitors as the reliability indicator:

$$r_j(t) = \frac{1}{RUL_j} \approx \lambda_j^{\mathrm{bl}} \tag{4.12}$$

where $r_j(t)$ is the reliability indicator, RUL_j is the remaining useful life, and λ_j^{bl} is the baseline or nominal aging rate of the jth supercapacitor group [45], [46]. According to (4.12), a supercapacitor is deemed failed when it reaches the end of its lifetime and its remaining useful life is the amount of time left until failure.

To obtain an expression for the analog of RUL_j, we consider Fig. 4.4. This design for the supercapacitor remaining useful life as the reliability indicator assumes that for small time steps, ESR evolves linearly. It is thus easy to obtain an expression for the reliability indicator and the remaining useful life analog:

$$r_j = \frac{1}{ESR_{\mathrm{EOL}} - ESR_{k+1,j}} \tag{4.13}$$

where ESR_{EOL} is the ESR at the end of life and $ESR_{k+1,j}$ is the projected ESR for the jth supercapacitor at the next time step $k + 1$ given by:

$$ESR_{k+1,j} = 2ESR_{k,j} - ESR_{k-1,j} \tag{4.14}$$

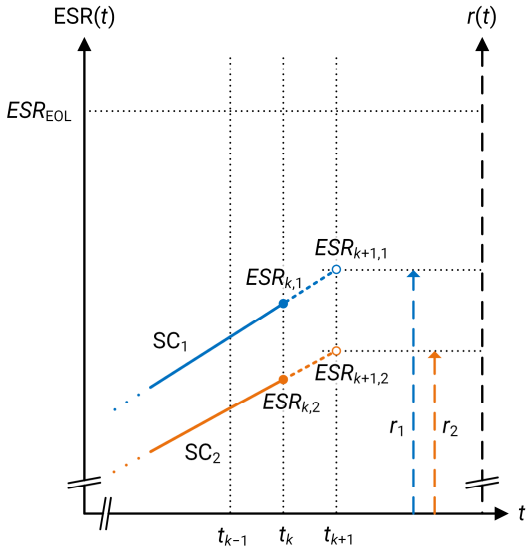

Fig. 4.4. Supercapacitor $ESR(t)$ evolution of two supercapacitors with different aging rates and the corresponding reliability indicators (not to scale)

We call the denominator of (4.13) an analog of RUL_j because as we saw in (4.12), RUL_j is conventionally defined in terms of time (cf. the nominal aging rate λ_j^{bl}). What (4.13) does is to redefine the remaining useful life in terms of ESR. This redefinition was needed because the initial simulations using the original time-defined reliability indicator in (4.12) showed a very slow system response to the control and thus the need for an analog expression based on the ESR. The new reliability indicator is based on the assumption of the linear ESR evolution mentioned earlier and thus on the equation of the lines in Fig. 4.4 formed as $ESR_{k+1,j} - ESR_{k,j} = \frac{ESR_{k,j} - ESR_{k-1,j}}{t_k - t_{k-1}}(t_{k+1} - t_k)$ and solved for ESR_{k+1}. It makes use of the ESR value predicted for the next time step $k + 1$. Given how the reliability indicator was designed in (4.13), supercapacitor 1 is more reliable than supercapacitor 2, which can also be seen in the lengths of the reliability indicators in Fig. 4.4. Formula (4.10) when applied to the current scenario should output a $V_{\mathrm{ref},2}$ greater than $V_{\mathrm{ref},1}$, which means that the supercapacitor 2 would be loaded more than supercapacitor 1. The consequence is that as the supercapacitors are cycled, the difference in reliabilities and thus in remaining useful lives should decrease with time.

4.4.3 Supercapacitor Modeling

The model for a supercapacitor Fig. 4.3(a) was implemented using Simscape, an environment within Simulink for multidomain physical modeling and simulation. A variable resistor block for ESR and a variable capacitor block for C_{sc} represented the supercapacitor model. Considering the end-of-life

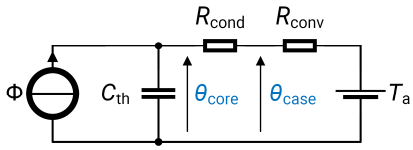

Fig. 4.5. A thermal model for supercapacitors [31], [47]

criteria for a supercapacitor, we use the dynamic lifetime model in (4.11) to update the value of $ESR_j(t)$ every time:

$$ESR_j(t) = \int_0^t \frac{ESR_{0,j}}{\tau_{d,j}(t)} \mathrm{d}t + ESR_{0,j} \tag{4.15}$$

$ESR_j(t)$ here represents the equivalent ESR of the jth supercapacitor group. Equation (4.15) starts off with an initial ESR value of $ESR_{0,j}$. As previously mentioned, an end-of-life criterion is when the ESR increases by 100% and thus we have another $ESR_{0,j}$ in the numerator inside the integral term. $ESR_j(t)$ needs to dynamically update every time, so the $ESR_{0,j}$ in the numerator is divided by the dynamic lifetime τ_d. The integral operator accumulates the resulting quotient over time and is then added to the initial value term. Each group is composed of 12 supercapacitors. It is assumed for simulation purposes that supercapacitors within a group have uniform characteristics. The same principles hold for the capacitance, but because the end-of-life criterion for this parameter is when it reaches 80% of its original value, the equivalent initial capacitance has to be multiplied with −0.2:

$$C_{sc,j}(t) = -0.2 \int_0^t \frac{C_{sc,0,j}}{\tau_{d,j}(t)} \mathrm{d}t + C_{sc,0,j} \tag{4.16}$$

where $C_{sc,0,j}$ is the initial capacitance (F) of the jth supercapacitor group. Because of (4.15) and (4.16), we assume that ESR and C_{sc} change at the same rate and reach the end-of-life criteria at the same time. Since it does not matter which of the two parameters to track, we express supercapacitor SoH in terms of ESR:

$$SoH_j(t) = 100 \cdot \frac{2ESR_{0,j} - ESR_j(t)}{ESR_{0,j}} \tag{4.17}$$

As was discussed in Subsection 4.4.2, the conventional reliability indicator in (4.12) has been redefined to be based on $ESR(t)$ in (4.13).

Another important parameter in the aging of supercapacitors is temperature. A circuit model for the thermal behavior was used and is shown in Fig. 4.5 [31], [47]. In this model, Φ is the heat generation from Joule heating (W); C_{th} is the thermal capacity (J/K) of the supercapacitor; R_{cond} is the thermal conduction resistance (K/W) and models heat transfer from the core of the supercapacitor to its case;

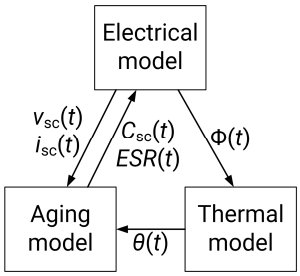

Fig. 4.6. The supercapacitor multiphysical model and the interactions among the models.

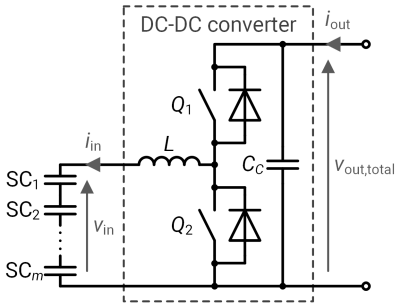

Fig. 4.7. A single nonisolated bidirectional DC-DC converter interfacing a supercapacitor stack at the low side ($v_{\text{out,total}} \geq v_{\text{in}}$).

R_{conv} is the thermal convection resistance (K/W) and models heat transfer between the case and the air; and T_{a} is the ambient temperature (K). θ_{core} represents the temperature (K) of the supercapacitor core and θ_{case} represents the case temperature (K).

The supercapacitor core temperature (in °C) is fed into the dynamic lifetime model in (4.11). To complete the parameters in the lifetime model, voltage- and current-sensing blocks were employed in the Simscape model to measure these parameters. An additional RMS block was needed for the measured current before being fed into the lifetime model. With the aging, thermal, and electrical models, and the interdependency among them as can be seen in Fig. 4.6, we now have a suitable multiphysical model we can use for the supercapacitors.

4.4.4 Modeling the Converter

To be able to use our supercapacitor model in simulation with modular power converters, we must have a model for the converter as well. A similar nonisolated bidirectional DC-DC converter to the one first discussed in Sections 2.1 and 2.2 (specifically Fig. 2.1(a)) with additional details in Appendix A, with specifications in Table 2.1 was used in this case. Fig. 2.1(a) is reproduced here and is shown in Fig. 4.7. The original converter for 120 supercapacitors in the Hybus project was sized to have an inductor with $L_{\text{orig}} = 160$ mH and a capacitor with $C_{C,\text{orig}} = 1{,}600$ μF for a maximum voltage ripple of 2% and a maximum current ripple of 12% [44]. A pulse-width modulated (PWM) signal with a

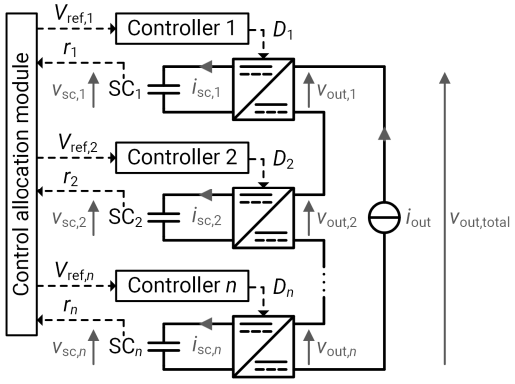

Fig. 4.8. The multiple modular power converter system used for the simulations.

frequency of 10 kHz serves as the control signal [44]. For the modular converter approach, the 120 supercapacitors were grouped by ten ($n = 10$). Each group has 12 supercapacitors, which now shoulders a tenth of the original load. Based on this and on the formulas for the ripple voltage and current [95], the new inductor size $L = 16$ mH should be ten times smaller than the original L_{orig} and the new capacitor $C_C = 16$ mF ten times larger than $C_{C,\text{orig}}$ to keep the same ripple values.

The PWM signal controlling the two switches are complementary. For example, in Fig. 4.7, when switch Q_1 is on, the other switch Q_2 is off, and vice versa. The signal's duty cycle is represented as D. While it is possible to implement the switched model in Simscape, we will have faster simulation if we used the averaged model instead. The goal is to simulate the whole system lifetime, so it is imperative that we do it fast, and derive and use the averaged model of the converter. We use the state-space averaged model in (2.3)–(2.5) (cf. Subsection 2.2.3 and Appendix A), which was derived by considering the two states of the converter. The first state is: switch Q_1 is off and Q_2 is on; and the second state is: switch Q_1 is on and Q_2 is off. We then look for each state's system equation of the form $\dot{\mathbf{x}} = \mathbf{Ax} + \mathbf{Bu}$. We then solve for the average values of $\mathbf{A}$ and $\mathbf{B}$ over the switching period: $\mathbf{A} = \overline{\mathbf{A}} = D\mathbf{A}_1 + (1 - D)\mathbf{A}_2$ and $\mathbf{B} = \bar{\mathbf{B}} = D\mathbf{B}_1 + (1 - D)\mathbf{B}_2$ to find the averaged model. We followed a similar process for the output equations ($\mathbf{y} = \mathbf{Cx} + \mathbf{Eu}$). Doing that, we arrive at our goal, the state-space averaged model of the converter in equations (2.3)–(2.5).

We then use this averaged model in (2.3)–(2.5) to build the Simscape model of the nonisolated bidirectional buck-boost DC-DC converter in Fig. 4.8 that we then connect to our supercapacitor model. The actual Simscape implementation of the power converter is in Fig. A.2, but Fig. 4.8 represents the overall system implementation of the multi-modular converter system including the control allocation module that has the supercapacitor reliability indicators as input and the converter reference voltages as output.

Table 4.1. Simulation parameters.

Parameter		SC group 1	SC group 2	SC group 3
V_{ref}	(V)	Control allocation	Control allocation	Control allocation
V_{ref} period	(s)	10	10	10
$C_{sc,0}$	(F)	3,150/10	3,000/10	2,850/12
ESR_0	(mΩ)	10 × 0.272	10 × 0.29	10 × 0.308
V_0	(V)	10 × 2.7	10 × 2.7	10 × 2.7
T_a	(°C)	25	25	25
C_{th}	(J/K)	700	700	700
R_{conv}	(K/W)	4.1	5.9	7.7
R_{cond}	(K/W)	0.627	0.627	0.627
Acceleration factor		10	10	10

4.4.5 Simulation

We simulate a smaller system of three converters ($n = 3$) for the initial simulation results here. The schematic diagram in Fig. 4.8 with $n = 3$ shows the system under consideration. The total voltage output $v_{out,total}$ is regulated at 105 V. An ideal current source i_{out} sinks and current sources at ±50 A. It roughly simulates what happens in the Hybus trolleybus for example: the supercapacitors supplying power to the auxiliaries (or discharging) and the supercapacitors drawing in power from regenerative braking (or charging). The period for this discharge-charge cycle was set at 40 s. The regular discharging and charging makes it easy as well to compare the modular converter approach with the classical balancing one. On average, each converter processes 5.25 kW of power.

Table 4.1 shows the parameters used in the simulation. The control allocation module provides the reference voltages, which are held for a period of 10 s. The values for the three groups, each connected to a converter, are the same except for the initial capacitance $C_{sc,0}$ and the thermal resistance to convection R_{conv}. The variation in capacitances was set not only to simulate real conditions, but to induce a difference in the voltages of the supercapacitor groups at the end of the discharge-charge cycling. This is required for the comparison with the classical balancing later. Such a variation in capacitances must be accompanied by a variation in the initial ESR_0 as well. Meanwhile, the variation in the thermal resistance to convection values was set to simulate the different positions of the supercapacitor groups in a 120-cell stack. A supercapacitor group's heat generation affects the thermal behavior of its neighboring groups.

The normal discharge-charge cycling of supercapacitors happens for ~12 min. Fig. 4.9 shows the 1,499 h 45 min up to 30 min later portion of the converter reference voltages and the voltages of the three supercapacitor groups during the first discharge-charge cycling. The decreasing supercapacitor voltages are mainly due aging control through control allocation and to the efficiencies of the

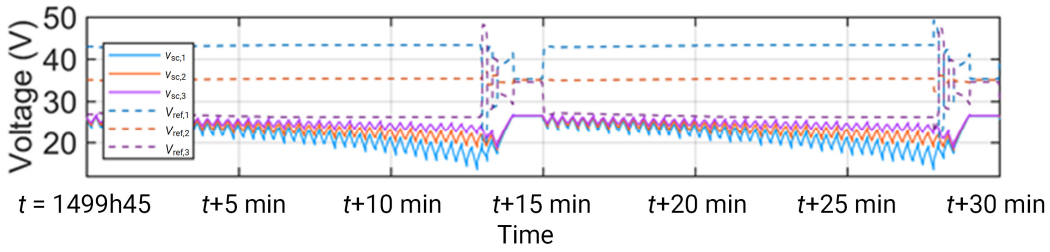

Fig. 4.9. The reference voltages of the converters and the voltages of the supercapacitors.

supercapacitors, which are around 95%. A portion of the power that goes through a supercapacitor is lost as heat in its ESR. The uneven dynamics of the converters for their buck and boost modes also contribute to this loss but is negligible. Supercapacitor 1, which has the lowest voltage is the most loaded as evidenced by its converter reference voltage, which is the highest. It also has the coldest temperature. This means supercapacitor group 1 is the most healthy among the three and that aging control works. Because supercapacitor 1 is the healthiest and the most reliable, the control strategy demanded more power from it, and this was reflected in the highest converter reference voltage (or the highest converter output voltage) among the three. Remember that all three supercapacitor voltages are equal at the beginning of the 15-min cycle and the highest power load demanded from supercapacitor 1 manifested as the highest current load. Over the 12-min normal discharge-charge period, the voltage of supercapacitor group 1 decreased the most because of the current load.

As can be seen in Fig. 4.9, starting at ~1,500 h 12 min, a different phase operates for 2 min until 1,500 h 15 min. This is the charging phase and during this period, the voltage-balancing strategy of Subsection 2.3.4 operates. Once the supercapacitor cells reach 2.7 V, charging stops and the system enters a rest period until the normal discharge-charge cycling operates again at the next cycle. Note that in Table 4.1, there is an acceleration factor of 10. The effect of this parameter is to accelerate the aging of the supercapacitors ten times. Thus, the lifetimes that will be shown in the next figures are not the values that can normally be expected of supercapacitors at the end of their lives.

4.4.6 Comparison with classical balancing

We now compare the new strategy towards lifetime balancing, the modular converter approach, with the classical balancing strategy. For the classical balancing strategy, the switched resistors (SR) circuit, as shown in Fig. 4.10, was used. Supercapacitor voltages are measured every 0.1 s and if a group has a voltage that is greater than 0.15 V of the average of all the groups' voltages, that group is shunted. Each shunt resistor was designed to have R = 120 Ω. This was done to ensure that the current through the shunt resistor has a value of 270 mA when the supercapacitor group has a voltage of $V_{\max}$. Power dissipation in the shunt resistors was also limited to 8.75 W because of this. Fig. 4.11(a) shows the

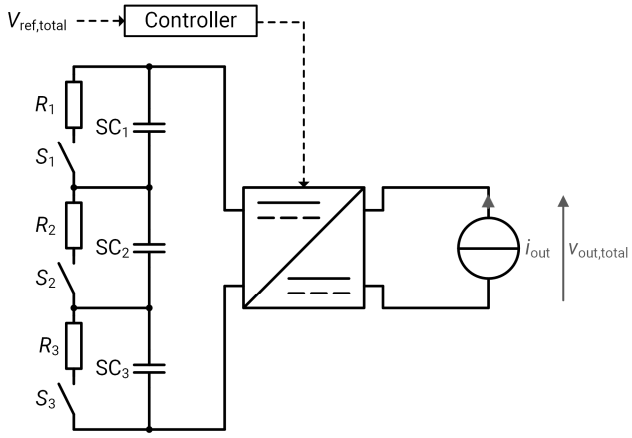

Fig. 4.10. The three supercapacitor groups using the classical balancing technique.

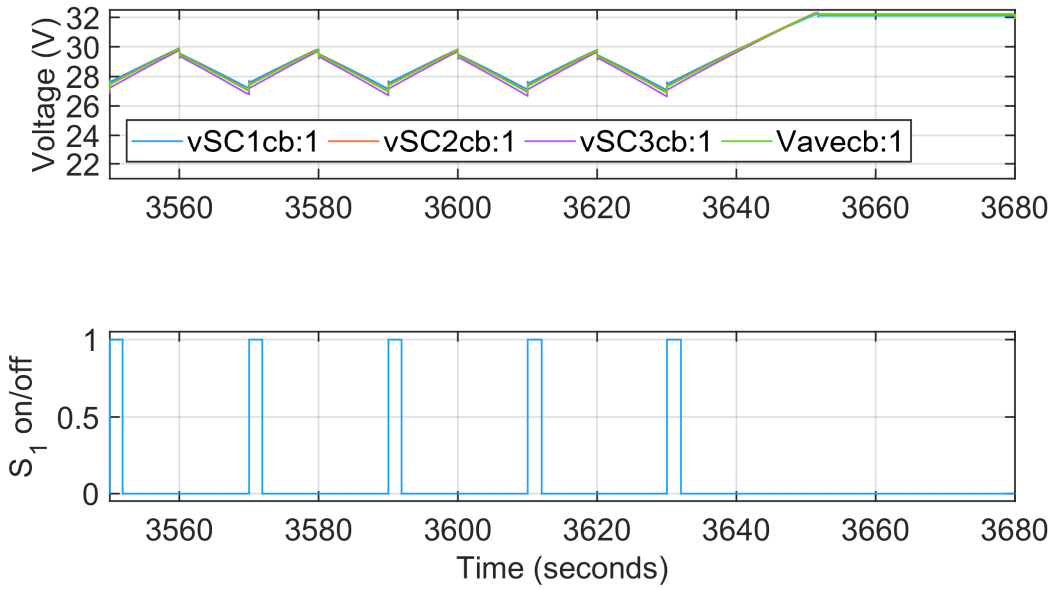

Fig. 4.11. (a) The voltages of the supercapacitors with a classical balancing strategy and (b) The switching of the shunt resistor for supercapacitor group 1.

supercapacitor voltages when the classical balancing strategy is used. On the other hand, we have in Fig. 4.11(b) the switching of the shunt resistor for voltage balancing of supercapacitor group 1. It can be seen that the shunting is only active for ~2 s out of the 20-s discharge-charge cycle. However, this period depends on the level of aging of the supercapacitors and is expected to grow longer as the supercapacitors age.

The same procedures for modeling and controlling the converter in the SR circuit were followed as in Subsections 4.2 and 4.3 but adapted for the sizing in Fig. 4.10. Additionally, the dynamic performance of the converter for the classical balancing strategy and its control was compared with that of the modular converter approach to ensure that the comparison is valid. There is a very small difference

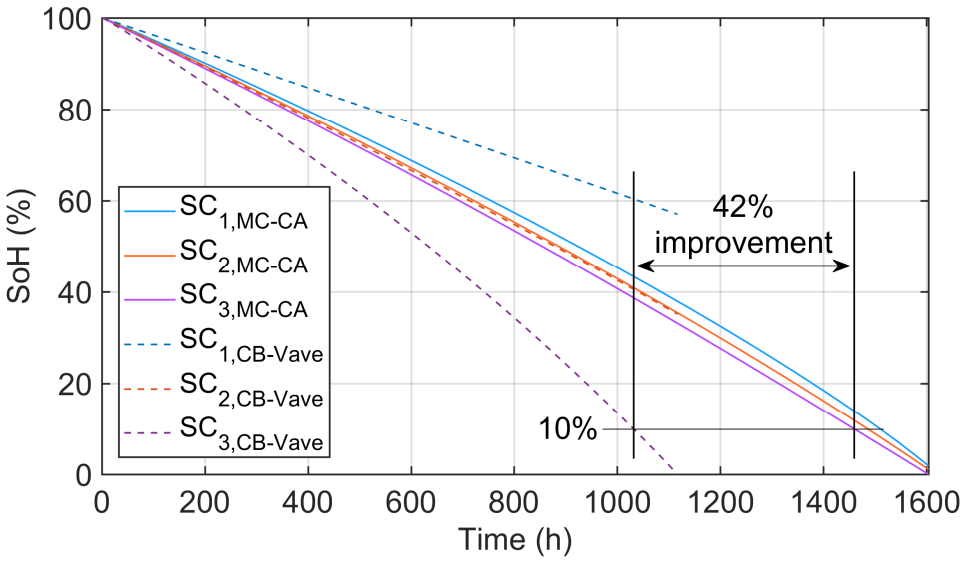

(a)

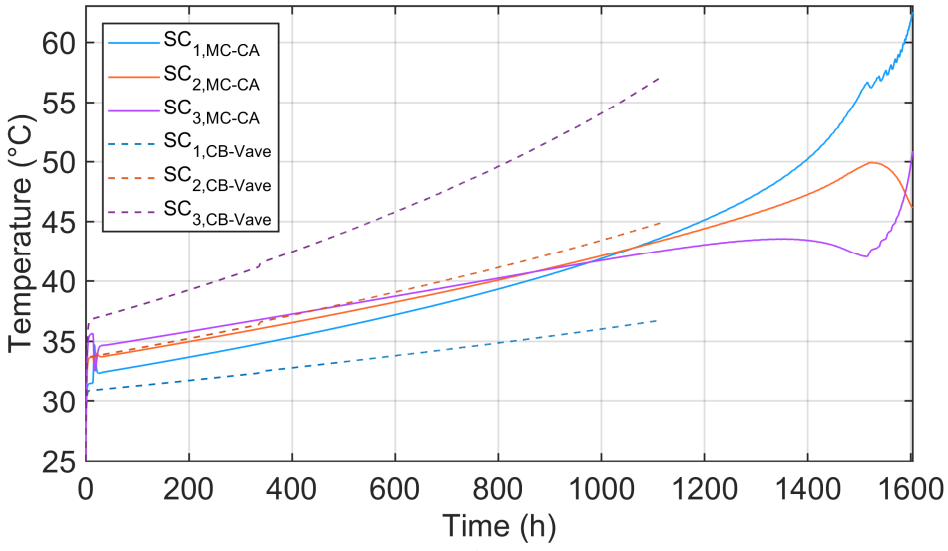

(b)

Fig. 4.12. (a) Comparison of SoHs for the classical and modular converter approaches and (b) the temperatures.

in terms of the performance of their dynamics, so in this aspect, it was taken to mean that the control systems for the two approaches are comparable.

Fig. 4.12(a) shows the comparison of the simulation results for the two approaches. It shows that the modular converter approach can prolong the system lifetime by 42% in the case study. The SoH's of the supercapacitors in the modular converter approach are much closer to one another (curves $SC_{j,MC\text{-}CA}$), compared to those of the classical balancing approach (curves $SC_{j,CB\text{-}Vave}$), which are more dispersed. In both cases, supercapacitor group 1 has a higher SoH compared to the others. Group 2 follows it, then group 3. The modular converter approach is able to extend system lifetime because

supercapacitor group 1 is loaded more, compared to the other two. The load that group 1 takes is freed up for the other two groups. Because of this, supercapacitor groups 2 and 3 are loaded less. However, the effect is most noticeable for group 3, which has the worst SoH. Fig. 4.12(a) illustrates this point. It shows the reference voltages for the three converters, which are also the output voltages of the converters at steady state. The output current is the same for all three converters, so the reference voltages basically show how the supercapacitor groups are loaded. Remember that the reference voltages are computed through the pseudoinverse method in (4.8) based on the supercapacitor remaining life as the reliability indicator. The extension of the system lifetime would not have been possible if the three converters were loaded equally with a reference voltage of $\frac{V_{\text{out}}}{3} = 35$ V.

Fig. 4.12(b) shows the effect of the modular converter approach to the supercapacitor temperatures. While there was initially a ~3°C difference among the groups for the classical balancing strategy, the difference grew to at least 10 °C at the group's end of life. The same is not true for the modular converter approach. There was also an initial difference, but the strategy was able to keep the temperatures close to each other not exceeding a difference of 1–2 °C for most of the system life. It was only at 1,200 h that the temperatures started to diverge. The main reason for this divergence is the saturation of the control for aging due to the aged parameters of the supercapacitor groups.

4.5 Application in Modular Multilevel Converters with Integrated Energy Storage

4.5.1 Supercapacitors Integrated with Modular Multilevel Converters

The continued reduction in costs of batteries and other technologies has led to increased applications of energy storage in the power grid. Energy storage has been employed to provide energy shifting and peak shaving services to the electrical grid. In energy shifting for example, energy is stored during off-peak hours, when price is lower. It is then discharged during peak hours, which is also a period when price is higher. While energy storage is a net consumer of energy, it has been demonstrated able to earn a net revenue from this energy arbitrage. Energy shifting thus finds many uses in the grid: energy storage during times of overgeneration from variable energy sources, avoiding costly startups of other generators through use of stored energy, providing operating reserves as an ancillary service, and providing peaking capacity during times of net peak load [48]. Peak shaving is related to the latter in the sense that energy storage provides peak capacity and power systems no longer need to be dimensioned for peak load thus minimizing the system's under-utilization. In another sense, energy storage provides additional capacity to the grid through peak shaving and makes possible deferment of costly grid upgrades improving overall efficiency [48], [96].

High-voltage direct current (HVDC) has emerged as a solution to bulk power transmission over long distances making possible intra- and intercontinental electric energy exchange and overcoming other geographic challenges. Renewable energy is not necessarily abundant at the place where there is demand for it or where the main network is, say in industrial and urban centers. Solar energy plants for example, need huge tracts of land with insolation and are thus necessarily located a long distance away from metropolitan areas. Offshore wind farms located in the middle of the sea where wind speeds are higher compared to the mainland are another example. This is notably different from large, centralized fossil fuel power plants that are located near the demand centers. In the renewable energy case, HVDC is employed in transmitting electrical energy from where the variable source is to where the demand is. In this context, modern power electronic converters in the form of voltage source converters (VSC) capable of AC-DC conversion are at the core of HVDC transmission technology (VSC-HVDC). VSC-HVDC systems are ideal for a robust and efficient transmission of electrical energy from remote sources. They are envisioned to form the backbone of future supergrids that will allow countries to trade high volumes of energy delivering electricity to where it is needed [49].

The active and reactive power in a VSC-HVDC system can be controlled within its operating range allowing full export or import of active power. This introduces additional flexibility in maintaining power quality in the connected AC networks. Modular multilevel converters (MMCs) are fast becoming the topology of choice in applications of VSC-HVDC systems. It has built-in redundancy, high efficiency, and low harmonics. The two-level converter VSC topology is still the preferred solution for low-voltage applications up to a couple of kilovolts. Above this level however, no power semiconductors are able to block the voltage. It is possible to connect the semiconductors in series to withstand higher voltages, but this solution has proven to be complex and expensive. Multilevel converter topologies that do not require direct series connection have thus been used at these levels. Cascaded topologies based on series connection of converter submodules are used to increase the operating voltage [49].

The intermittency of renewable energy sources, which VSC-HVDC systems interface introduces a new host of challenges. Regard has to be paid to strengthening operation and balance management, forecasting, and energy flow management with large integration of renewable sources into power systems. Balance must always be maintained between generation and consumption and the system frequency serves as an indicator. If the frequency rises, generation is exceeding consumption. The converse happens when consumption overtakes generation. The intermittent nature of renewable sources introduces a lot of uncertainty on the generation side making instances of imbalance much more common. Integration of energy storage is thus employed to ensure power balance. In times when energy from the renewable source suddenly plummets, stored energy from spinning reserves or from energy storage systems such as batteries can make up for the lost generation due to intermittency [49]. Of

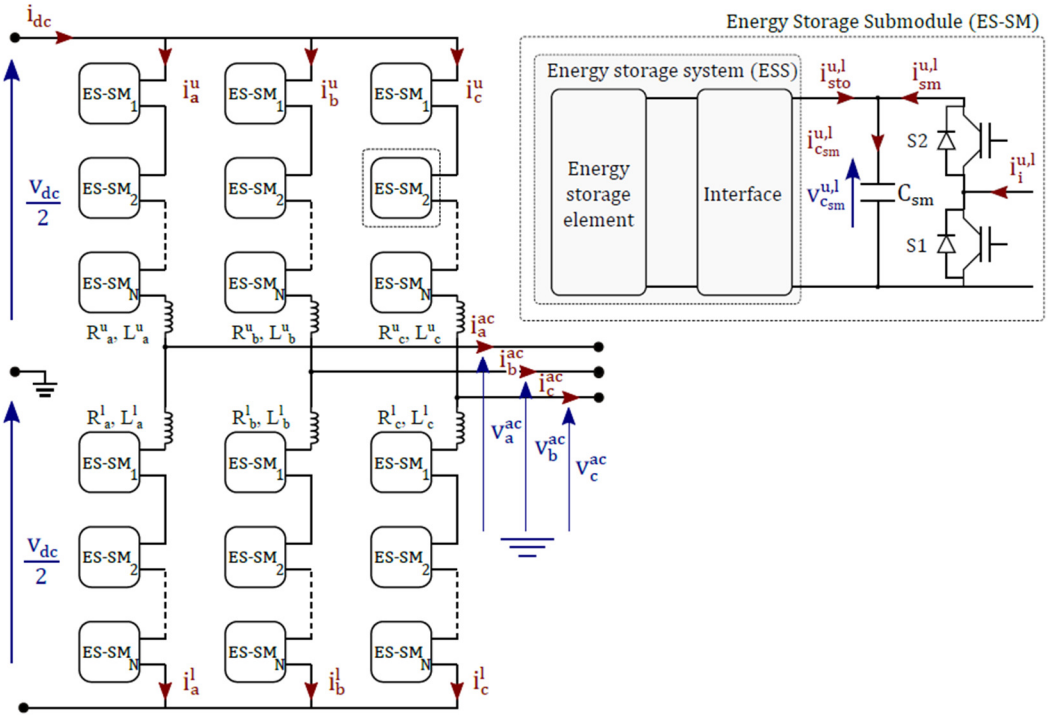

Fig. 4.13. A modular multilevel converter (MMC) whose submodules (energy storage submodule or ES-SM) have integrated energy storage (energy storage system or ESS) through an interfacing converter [50] © 2022 IEEE

course, as previously said, energy can also be stored when it is overflowing from the renewable source. A number of energy storage technologies are already in use and individual characteristics and purpose dictate the suitable architecture for grid integration. In the context of MMCs, energy storage systems have recently been integrated into MMC submodules [29], [32], [50].

In place of an energy storage system connected to a common DC bus, it can instead be distributed among the MMC submodules. However, a direct connection of energy storage cells to the submodule capacitor is not possible owing to the coupling of the voltage of the cells to the capacitor's and the presence of voltage ripples due to the switched current through the submodule capacitor. In addition, the latter has a negative effect on the lifetime of the energy storage cells. For the intended scheme, passive filters and control methods have been proposed for the integration of energy storage systems into MMC submodules. Furthermore, the high voltage level across the submodule capacitor is interfaced by DC-DC converters to the energy storage cells. The interfacing converter has its own independent control that adds to the system flexibility. At SuperGrid Institute, a modular design for the interfacing converter to supercapacitor energy storage cells has been proposed. The proposal has a better power density in addition to a control strategy that mitigates the low-frequency fluctuations of the MMC submodule at the supercapacitor side and that equalizes the supercapacitor SoC without modifying the

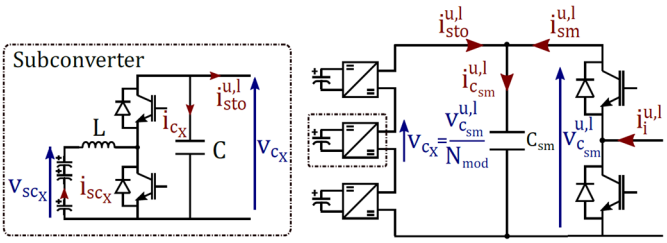

Fig. 4.14. Cascaded modular DC-DC converters serving as interfacing converters between strings of supercapacitor cells and one submodule (ES-SM) of an MMC [50] © 2022 IEEE

control structure for the MMC [32], [50]. Fig. 4.13 shows the architecture of an MMC and the proposed connection of the interfacing DC-DC converter and energy storage cells to a submodule.

Fig. 4.13 shows the general structure of a three-phase MMC. Each phase leg is composed of an upper arm and a lower arm. In turn, each arm consists of a string of identical half-bridge submodules in series with an inductor [32], [49], [50]. In the SuperGrid Institute MMC with integrated energy storage for delivering power for fast frequency response services, each submodule's capacitor has been connected to an interfacing converter and supercapacitors, thus making up an energy storage submodule (ES-SM). This solution has been shown not to require significant changes to the design of the MMC. The MMC with integrated energy storage follows a rating of 1 GW and has to be able to provide 5% of its power, which is 900 MJ at 50 MW power output for 18 s. The energy storage cells thus must have a power density high enough to deliver a fast power response. For this reason, supercapacitors were chosen in addition to their full discharge capability, high reliability, and long lifetime [32], [50].

In Fig. 4.13, three interfacing converter topologies were considered for integrating energy storage cells into the MMC submodules: single-stage, interleaved, and modular converters. Modular DC-DC converters were chosen to interface the supercapacitors on the bases of costs and volume. It was found that among the three, modular converters presented the least cost and the least volume, which are important factors because assembled MMC submodules are physically large [32], [50]. Fig. 4.14 shows the schematic diagram of the modular power converters connected to the submodule capacitor C_{sm}. The converter outputs are in series and connected at their inputs are the supercapacitors strings. We can immediately see the same architecture as in Fig. 4.2. We can assume that much like any case, the supercapacitors integrated into the SuperGrid Institute MMC with integrated energy storage in the submodules will have varying initial characteristics. Each submodule will need to be connected to 460 supercapacitor cells and in the specific MMC application, each phase leg has 800 submodules or 400 submodules per arm. Such large stacks are distributed in a facility and are thus bound to have nonuniform temperatures. Over time, these variations in operational characteristics reflect in the nonuniform aging of the cells. The SuperGrid Institute MMC with integrated supercapacitor energy

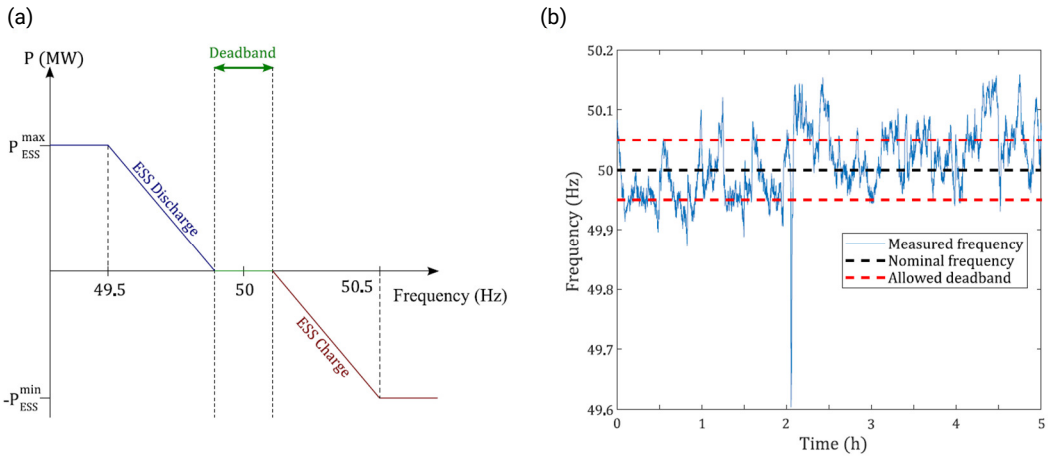

Fig. 4.15. (a) Power response of the supercapacitor energy storage system during a grid frequency deviation and (b) A five-hour sample of the 2016 historic grid frequency [28] © 2020 IEEE

storage application presents an opportunity to use the lifetime optimization method that was developed in the prior half of this chapter for the Hybus application.

4.5.2 Reliability Indicator for Calendar Aging

The United Kingdom's electricity sector is one among many that has become increasingly decarbonized. Inverter-based renewable energy sources like wind and solar have progressively replaced fossil fuel-based power plants. The resulting grid energy mix has created an operability challenge in the form of reduced inertia. Fossil fuel-based plants have traditionally provided the inertia needed in order to maintain the system frequency. It has become more unpredictable and volatile due to renewable energy intermittency. Therefore, the United Kingdom's National Grid Electricity System Operator (ESO) called for auctions for enhanced frequency response (EFR) in 2016 [97].

National Grid ESO's EFR is a balancing service meant to replace its legacy service firm frequency response used before in the age dominated by fossil-fuel power plants and to be at least four times as fast. EFR achieves 100% active power within one second or less of registering a frequency deviation or event with the goal of maintaining the system frequency at 50 Hz. Significant changes happened in the energy landscape since EFR's launch that presented new challenges. It has since been determined that a single product for fast frequency response service will not suffice and a suite of products has to be developed [97]. National Grid ESO has in fact discontinued EFR auctions with the 2020 launch of another service, dynamic containment, which offers even faster frequency response.

The second-by-second historic frequency data in 2016 provided by the National Grid ESO for the United Kingdom grid was used to obtain a load profile for the supercapacitor energy storage system [98]. It must be able to provide a proportional frequency response in either direction to a change in

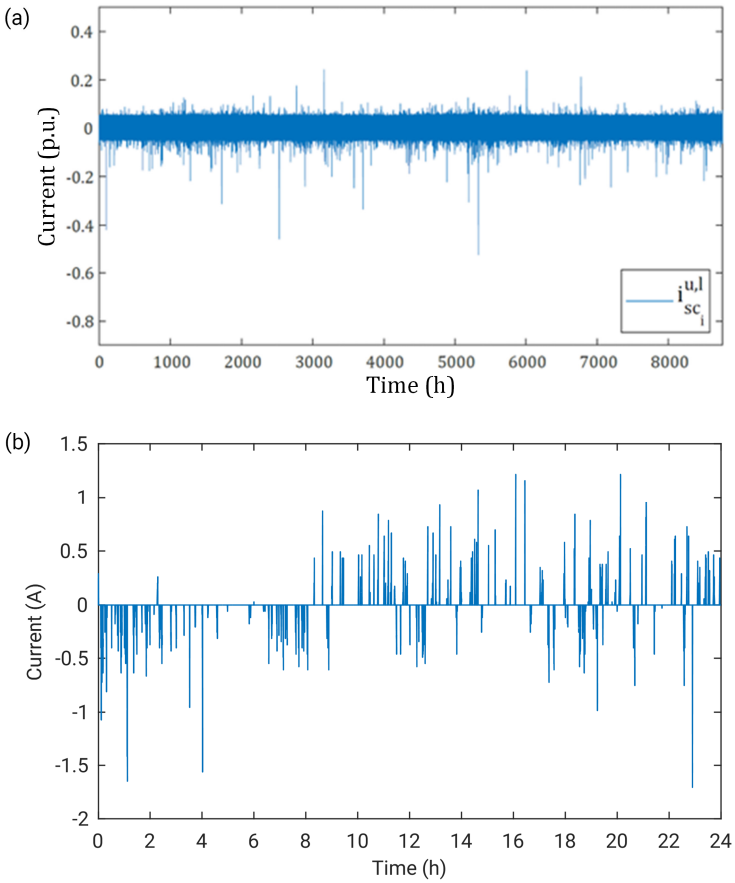

Fig. 4.16. (a) One-year current load profile of the interfacing modular converters [28] © 2020 IEEE and (b) The first day (24 hours) of the load profile

system frequency outside of the range 50 ± 0.05 Hz for a maximum of 30 s. Fig. 4.15(a) shows how the supercapacitor energy system responds to a frequency deviation. When the system frequency goes below the set range, the supercapacitors have to inject power into the grid and thus discharge its stored energy. This is a case when power generation suddenly cannot meet consumption. Above the set frequency range, the supercapacitors have to absorb energy from the grid and charge. The latter happens when power generation suddenly exceeds consumption. Fig. 4.15(b), on the other hand, shows a five-hour sample of the 2016 historic frequency data. The set frequency range can also called a deadband because the energy storage system neither has to supply nor absorb energy to/from the grid for fast frequency response. Within this deadband, the supercapacitors are allowed to charge/discharge up to ±9% of the rated energy storage system power in order to maintain the SoC [28], [32].

The generated current load profile for the modular converters based on the historic frequency data can be seen in Fig. 4.16(a) with the first 24 hours of the profile zoomed in in Fig. 4.16(b). The first thing we can observe from Fig. 4.16(a) is that the current very seldom peaks at a value above 1.17 A. In fact, there is no current most of the time and this can be verified in Fig. 4.16(b). This profile is thus very

different from the current load profile of the Hybus project, which is characterized by cycling. This case for the SuperGrid Institute MMC with integrated energy storage system application is mostly characterized by calendar aging even though there are sometimes bursts of current. The reliability indicator as currently designed in (4.13) will not work in this case. If we take another look at the thermal model in Fig. 4.5 and consider the present application, the temperature of the supercapacitors should be about the same as the ambient temperature because of the low current levels. The supercapacitors should not heat up above the ambient level. As for the dynamic lifetime in (4.11) which considers contributions from the voltage, temperature, and current levels, we can see that the current share is almost nil compared to the supercapacitor voltage and temperature for the same reason that the current levels are almost always zero in the load profile. Since the temperature is approximately the ambient temperature, this means that controlling supercapacitor aging should focus on controlling the voltage.

Fig. 4.9 shows how the supercapacitor voltages relate to the reference voltages using the current definition of the remaining useful life as the reliability indicator in Subsection 4.4.2. As the figure shows, the higher the reference voltage $V_{\text{ref},j}$ (and therefore the higher the converter output voltage $v_{\text{out},j}$), the lower the supercapacitor voltage $v_{\text{sc},j}$ even though all voltages started at the same level. Remember that the reference voltages come from the pseudoinverse method applied to the control of the modular power converters in (4.10) based on the reliability indicator defined in (4.13). This behavior is due to the efficiency characteristics of the bidirectional converter shown in Fig. 4.7 where the converter becomes more efficient as the converter output current becomes lower. This is true without regard to whether the converter is in buck (charging) or boost (discharging) mode. In the Hybus project test case, the converter output current was set at a constant value of 50 A. The converter with higher reference voltages also have higher output currents. Following the efficiency characteristics just discussed, the same converters with higher reference voltages should also be less efficient. The result is that charge is not retained in the supercapacitors because of the lower efficiency. Thus, converter 1 in Fig. 4.9, which has the highest reference voltage among three, has its connected supercapacitor group 1 with the lowest voltage. Supercapacitor group 3, on the other hand, has the highest voltage level and the lowest converter reference voltage.

The foregoing discussion underpins the reason why the current design of the reliability indicator will not work in the present SuperGrid Institute MMC with integrated supercapacitor energy storage case. Because the current is almost always zero, the effect of the same reliability indicator used in the Hybus project case applied in the current case would be higher converter reference voltages resulting in higher supercapacitor voltages. However, what we desire is the converse, which is to have lower supercapacitor voltages. In order to resolve this, we took the simple route of taking the inverse of the

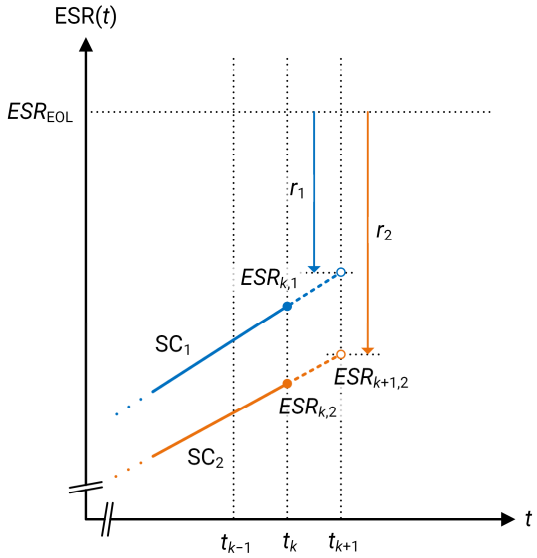

Fig. 4.17. The reliability indicators of two supercapacitors based on their present ($ESR_{k,j}$) and projected ($ESR_{k+1,j}$) ESR values

present definition of the reliability indicator in (4.13). Thus, the new reliability indicator for use in the present case is:

$$r_j = ESR_{\text{EOL}} - ESR_{k+1,j} \tag{4.18}$$

$ESR_{k+1,j}$ is still given by (4.14). If the previous reliability indicator was the inverse of the remaining useful life, the present one is approximately the remaining useful life itself. It is illustrated for two supercapacitors in Fig. 4.17 where $r_2 > r_1$. This should result in converter reference voltage $V_{\text{ref},1} > V_{\text{ref},2}$ and supercapacitor voltage $v_{\text{sc},2} > v_{\text{sc},1}$. The effect of higher converter reference voltages is to have lower supercapacitor voltages, which was the goal of taking the inverse of the previous reliability indicator definition in proceeding to the current definition in (4.18) for the present case. This will be shown in the next subsection. Ultimately, the more reliable supercapacitor will take in a higher share of the load and offer the less reliable one some measure of relief.

4.5.3 Modeling and Simulation Results Using an Aging Model

A preliminary discussion of the workings of the SuperGrid Institute MMC with integrated supercapacitor energy storage has been presented in Subsection 4.5.1. In order to test the lifetime optimization method presented in Section 4.3 with the new reliability indicator in (4.18) for the present application, the system in Fig. 4.14 was implemented in MATLAB and Simulink. As previously mentioned, MMCs are large and take up whole facilities because they are made up of 2,400 submodules, which in turn are further composed of subsystems and components. Since MMCs have six arms, each

Table 4.2. Energy submodule (ES-SM) and modular converter specifications

Parameter	Value
Energy Storage Submodule (ES-SM)	
SM capacitor voltage $v_{C\mathrm{sm}}^{\mathrm{u,l}}$ (V)	1,600
SM capacitor C_{sm} (mF)	10
Max. power $P_{\mathrm{sm}}^{\mathrm{max}}$ (kW)	20.83
No. of modular converters N_{mod}	4
Modular Converter Characteristics	
Operating voltage v_C (V)	400
Inductance L (mH)	0.91
Capacitance C (μF)	13
No. of supercapacitors per converter (N_{cells})	115
Max. supercapacitor voltage $V_{\mathrm{sc}}^{\mathrm{max}}$ (V)	310

arm then has 400 submodules. There is no need to simulate all ES-SMs in the proposed MMC with integrated supercapacitor energy system. In fact, there is only a need to simulate one in order to demonstrate how the lifetime optimization method will work for the application. The specifications of the one ES-SM and the connected modular converters are detailed in Table 4.2 [32], [50].

It was assumed in the simulation that the harmonics of the MMC present in the SM capacitor current that have both DC and AC components have already been eliminated at the supercapacitor side through the control of the ES-SM, previously done by another researcher in a related work. The AC component contains pulses and harmonics at the line and double line frequency. It is essential that they are removed not only to prevent oversizing the system and to prolong supercapacitor lifetime, but also to run a fast simulation of the system [32], [50]. The simulation was thus done purely in DC. Fig. 4.16 was previously mentioned to show the current load profile for the ES-SM. It was generated from the 2016 United Kingdom National Grid ESO historic frequency data seen in Fig. 4.18(a) [98]. Respecting the EFR specifications in Section 4.5.2 and summarized in Fig. 4.15(a), a power load profile, shown in Fig. 4.18(b), was generated for the 50-MW energy storage power that the 1-GW SuperGrid Institute MMC should be able to provide in either direction for a maximum duration of 30 s. The power profile was distributed equally among all the 2,400 ES-SMs in the MMC resulting in a maximum power rating of 20.83 kW for each. The smaller ES-SM power profile was then used to generate the current load profile by dividing the former by the SM capacitor voltage of 1,600 V. This current is designated as the energy storage current or i_{sto}, which is what is seen in Fig. 4.14 and Fig. 4.16.

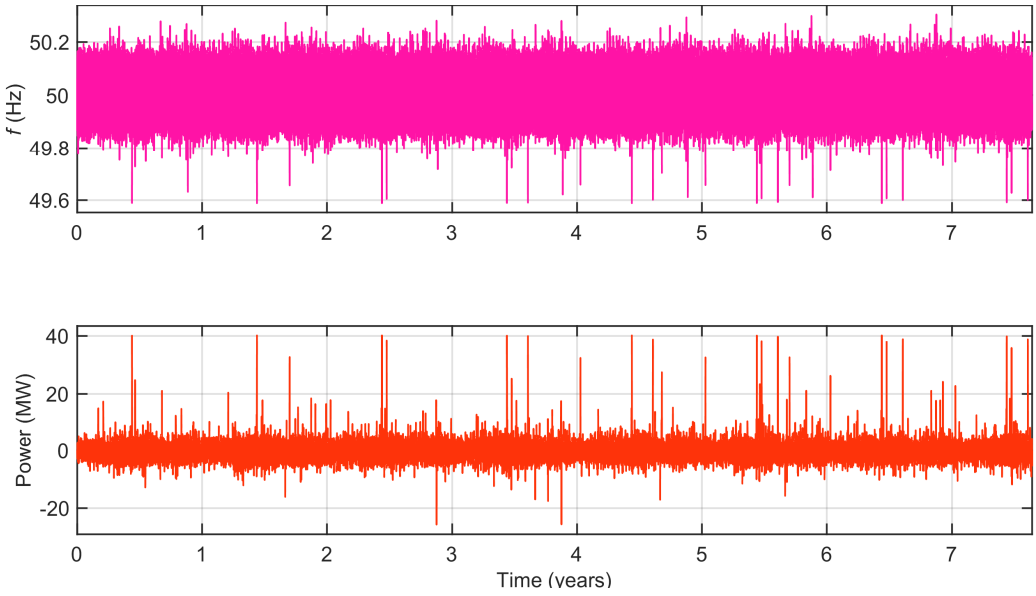

Fig. 4.18. (a) The 2016 United Kingdom National Grid ESO historic frequency data is repeated every year [98] and (b) The power load profile for a 1-GW MMC with 50-MW integrated supercapacitor energy storage following specifications for National Grid ESO's enhanced frequency response (EFR)

As each ES-SM has four modular power converters connected to it, each converter has a group of 115 supercapacitors in series connected at its input side. However, as was previously done in Subsections 4.4.4 and 4.4.5, we can treat the supercapacitor string as one equivalent supercapacitor. Recall that the ES-SM architecture is shown in Fig. 4.14. Table 4.3 shows the characteristic parameters of each supercapacitor group. The initial capacitance $C_{\mathrm{sc},0}$ = 310 F and initial ESR ESR_0 = 2.2 mΩ come from the datasheet of Maxwell BCAP0310 supercapacitors. The fact that the supercapacitor cells do not heat up much from the ambient temperature level due to the minimal current load profile was mentioned back in Subsection 4.5.2. Because of this, there is no reason to introduce a variation in R_{conv} values to induce different temperatures in the supercapacitor groups. Instead, it was the ambient temperature T_{a} that was varied from 59 to 65 °C in 2°C increment. This assumption is needed in order

Table 4.3. ES-SM supercapacitor simulation parameters

Parameter		SC group 1	SC group 2	SC group 3	SC group 4
V_{ref}	(V)	Control allocation	Control allocation	Control allocation	Control allocation
V_{ref} period	(s)	1	1	1	1
$C_{\mathrm{sc},0}$	(F)	$310/N_{\mathrm{cells}}$	$310/N_{\mathrm{cells}}$	$310/N_{\mathrm{cells}}$	$310/N_{\mathrm{cells}}$
ESR_0	(mΩ)	$2.2 \times N_{\mathrm{cells}}$	$2.2 \times N_{\mathrm{cells}}$	$2.2 \times N_{\mathrm{cells}}$	$2.2 \times N_{\mathrm{cells}}$
V_0	(V)	$2.14 \times N_{\mathrm{cells}}$	$2.14 \times N_{\mathrm{cells}}$	$2.14 \times N_{\mathrm{cells}}$	$2.14 \times N_{\mathrm{cells}}$
T_{a}	(°C)	59	61	63	65
C_{th}	(J/K)	60	60	60	60
R_{conv}	(K/W)	10.9	10.9	10.9	10.9
R_{cond}	(K/W)	0.627	0.627	0.627	0.627

to demonstrate how the lifetime optimization method works in this case and is reasonable in view of the physical size of a single MMC or even of just a single ES-SM. It can also be gleaned in Table 4.3 that the ambient temperature is the only factor that varies among the groups.

Like in the Hybus project application, the operational SoE was limited to 25% to 100% following the discussion in Subsection 2.2.2. The midpoint of this range is 62.5%, which corresponds to a supercapacitor voltage $v_{\text{sc}} = 2.14$ V. This same level should be the target voltage per cell if voltage equalization were the goal. However, as has been shown in Subsection 4.4.5 and Fig. 4.9 for the Hybus project, application of the lifetime optimization method based on control allocation results in unequal supercapacitor voltages. This voltage imbalance is necessary, so keeping all cell voltages at 2.14 V would not result in the goal of lifetime optimization. However, there is also a need to keep the SoE at the midpoint of 62.5% in case the energy storage system suddenly needs to supply or absorb power. An alternative formula for the SoE, whose original formula was expressed in equation (2.2), was formulated in order to deal with this problem:

$$SoE_{\text{ave}} = \left(\frac{\sum_{j=1}^{N_{\text{mod}}} v_{\text{sc},j}}{V_{\max} N_{\text{cells}} N_{\text{mod}}} \right)^2 \times 100 \tag{4.19}$$

This new formulation will let us keep the SoE of the energy storage system at 62.5% without necessarily keeping individual supercapacitor cell voltages at 2.14 V. Equation (4.19) is used to monitor the average SoE of all supercapacitor cells in the ES-SM. An $SoE_{\text{ave}} = 62.5\%$ means an average SoE of 62.5% for all cells. Keeping this midpoint during the deadband is important in lifetime optimization because we cannot let supercapacitor group SoE (or voltages) to just diverge over time. If we do, one group would reach $V_{\max}^{\text{sc}}$ or $V_{\min}^{\text{sc}}$ first and the whole MMC with integrated supercapacitor energy storage would not be able to do its job of fast frequency response, which entails the supply or absorption of power. For the same reason, operational SoE was further limited to between $SoE_{\min} = 35\%$ and $SoE_{\max} = 90\%$ with a 10% difference from the usual limits. Once a supercapacitor group reaches either limit, the voltage-balancing strategy previously presented in Subsection 2.3.4 kicks in until all supercapacitor cells are back to $v_{\text{sc}} = 2.14$ V. This means that the voltage-balancing strategy takes over the control of the modular power converters. Once the voltage-balancing strategy has reached this goal, the lifetime balancing method takes over the control of the modular converters again. This is similar to the transitions between lifetime optimization and voltage equalization in the Hybus project case, though also different in the specific implementation. In the latter, the transitions are timed, whereas in the present SuperGrid Institute MMC with integrated energy storage case, the transitions depend on the average SoE and supercapacitor voltages. Recall that both the voltage-balancing and lifetime optimization strategies can work even while delivering the current load profile.

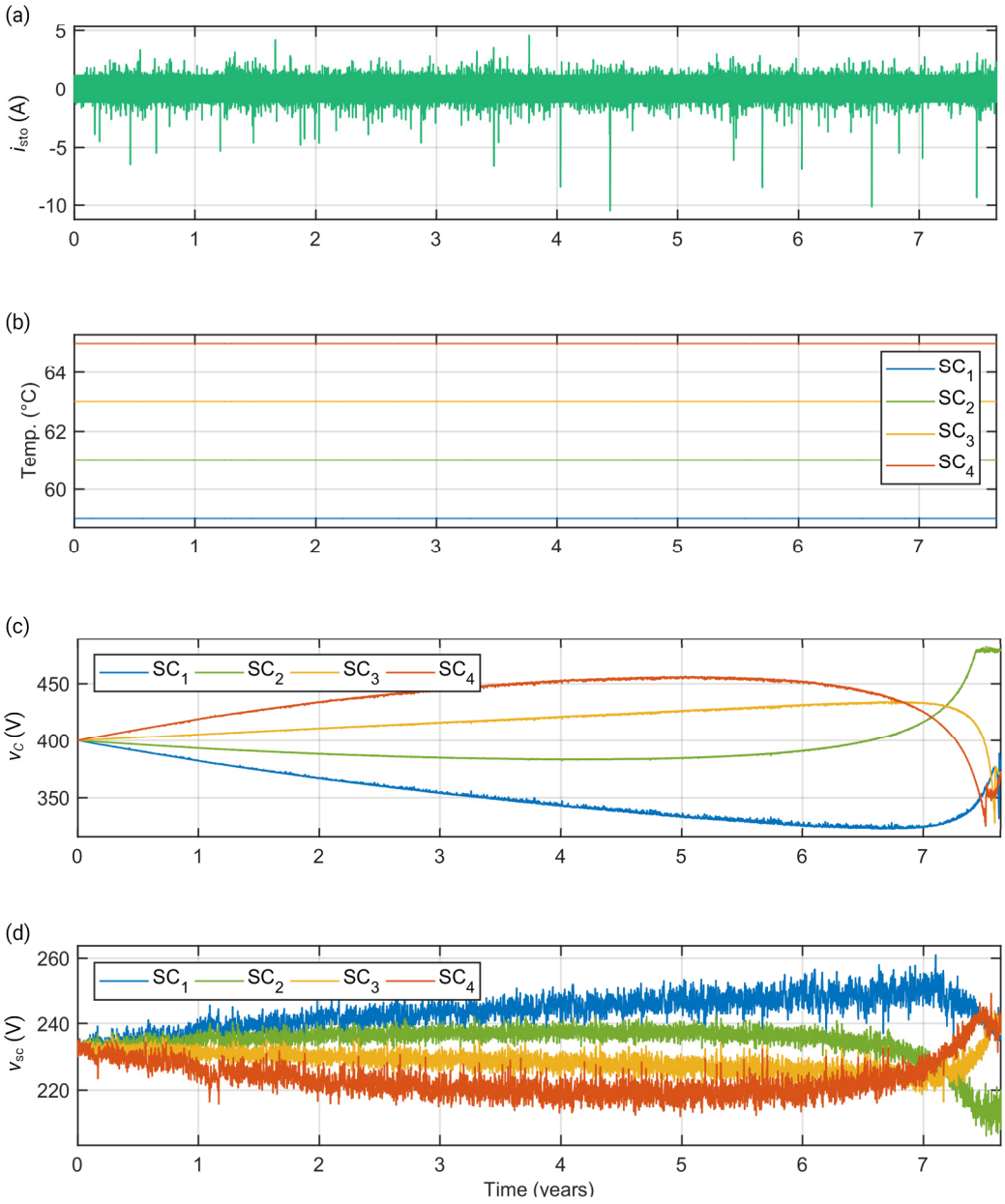

Fig. 4.19. (a) The current load profile for one ES-SM; (b) The temperatures of supercapacitor groups; (c) The output voltages of modular power converters following each converter reference voltage $V_{\text{ref},j}$ under lifetime optimization control; and (d) The voltages of each supercapacitor groups

For simulation purposes, assuming that the supercapacitor system lifetime is not known beforehand, National Grid ESO's historic frequency data and the following power load profile generated for the MMC with integrated supercapacitor energy storage (both shown in Fig. 4.18) were repeated every year until supercapacitor system end of life was reached. The resulting current load profile for one ES-SM is shown in Fig. 4.19(a). Recall that this current was designated as the energy storage current or i_{sto}, which is also the common current flowing through the outputs of the modular power converters in Fig. 4.14. Recall as well that because of the nature of the power load profile, i_{sto} is mostly zero as can

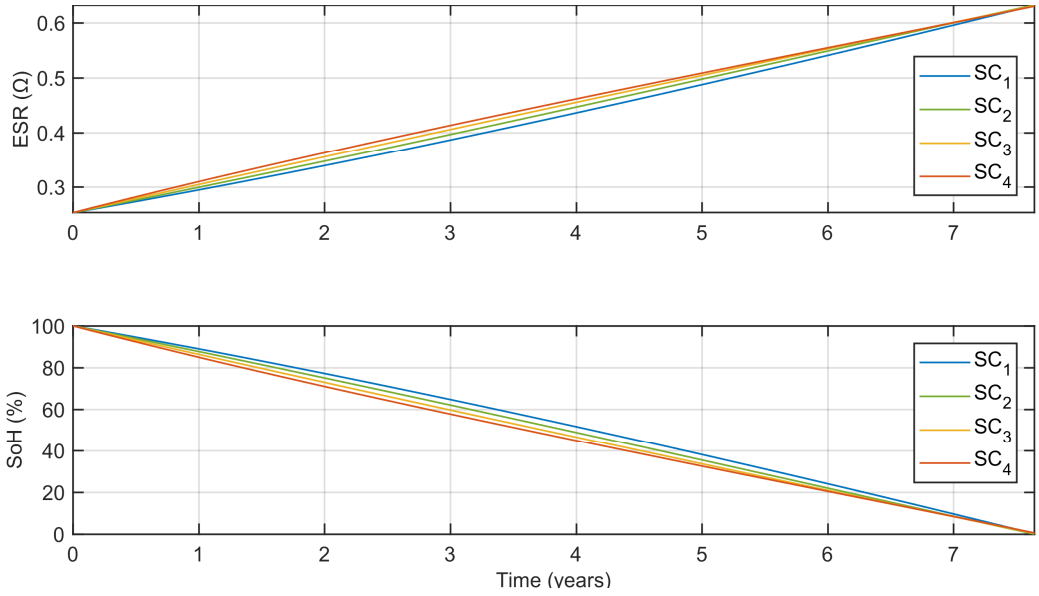

Fig. 4.20. (a) Evolution of the ESR of the supercapacitor groups under lifetime optimization control and (b) The SoH of the supercapacitor groups

be seen in Fig. 4.16(b). The current's appearance in Fig. 4.19(a) as being active with pulses is due to long period of the time axis up to the supercapacitor system end of life at 7.66 years. The four supercapacitor groups' temperatures are displayed in Fig. 4.19(b). It was assumed that the placement of each group has a different ambient temperature from 59 to 65 °C in 2-°C increment with group 1 having the lowest temperature and group 4 the highest. Recall that in Table 4.3, the ambient temperature was the only parameter varied.

Fig. 4.19(c) and Fig. 4.19(d) demonstrate how the reliability indicator designed for the present load profile and the overall control with the goal of supercapacitor system lifetime optimization works. Remember in Subsection 4.5.2 that the reliability indicator in (4.18) was formulated so that the supercapacitor with higher reliability will receive a lower reference voltage for modular converter control and for inducement of a higher supercapacitor voltage. In essence, the reliable one shoulders more of the work. This is illustrated by Fig. 4.19(c) and Fig. 4.19(d). Remember that all characteristic parameters of the four supercapacitor groups are the same except for the ambient temperature. We can thus consider the group with the highest temperature to be the weakest and the group with the lowest temperature to be the strongest. In this case, group 4 is the weakest or the least reliable and group 1 is the strongest or the most reliable. We can see that $v_{C,1}$ is the lowest, therefore $V_{\text{ref},1}$ is also the lowest and that induced $v_{\text{sc},1}$ to have the highest voltage. The reverse is true for supercapacitor group 4. The strongest group, group 1, shoulders more of the electrical load through a higher voltage. Because group 4 is the weakest, it was given a lighter electrical load that is reflected in lower voltage. This way, the higher contribution to aging of group 1's voltage makes up for lower contribution to aging of group 1's

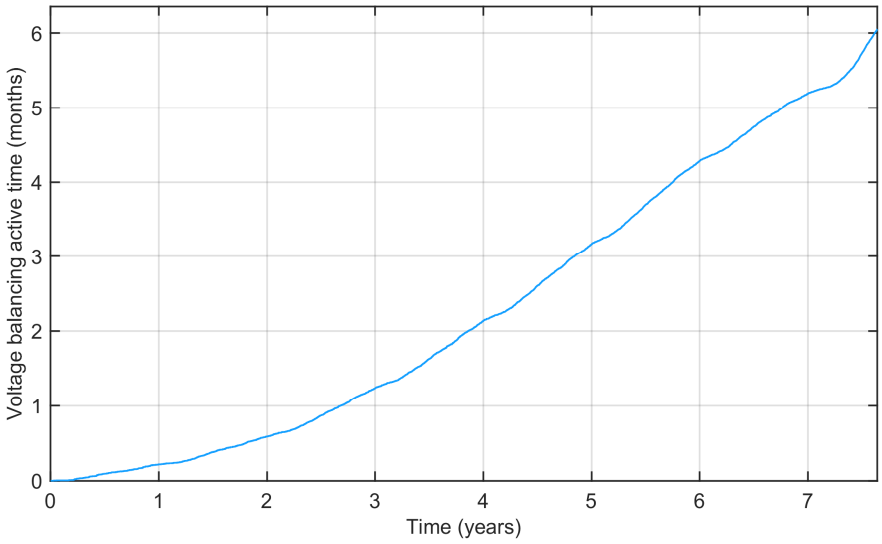

Fig. 4.21. Cumulative period of time during which the voltage-balancing strategy was active

temperature relative to the other groups. However, for group 4, the lower contribution to aging of voltage makes up for the higher contribution of the temperature. This is how the supercapacitor system life is optimized.

The evolution of the supercapacitor groups' ESR and SoH can be seen in Fig. 4.20(a) and Fig. 4.20(b), respectively. It can be seen in both the ESR and SoH plots that the supercapacitor system lifetime optimization method has the effect of balancing the groups' lifetimes. A similar effect was seen in the case of the Hybus project in Fig. 4.12(a). The initial trajectories of the individual group plots are to diverge until around after the third-year mark where they start converging again. Convergence is a long process and it took around after the seventh year mark before we can say that ESR and SoH are balanced or equalized. Simulation stopped at 7.66 years, where SoH reached 0%.

It was mentioned that the voltage-balancing strategy was also used in the simulation. Voltage balancing starts when one of the group voltages reaches one of the set SoE limits of either $SoE_{\min}$ = 35% or $SoE_{\max}$ = 90%. The voltage-balancing strategy in Subsection 2.3.4 then becomes active and remains active until the SoE_{ave} reaches 62.5%. Once SoE_{ave} = 62.5%, lifetime optimization becomes active again. In order to verify that it is the lifetime optimization method that is active most of the time, the cumulative period of time during which the voltage-balancing strategy is active was recorded in the simulation. A plot of that can be seen in Fig. 4.21. It is obvious that the voltage-balancing strategy was only active for a total of 6.15 months out of the 7.66 years of supercapacitor system life. This means that during the 7.66 years, the voltage-balancing strategy was active for only 6.7% of the time.

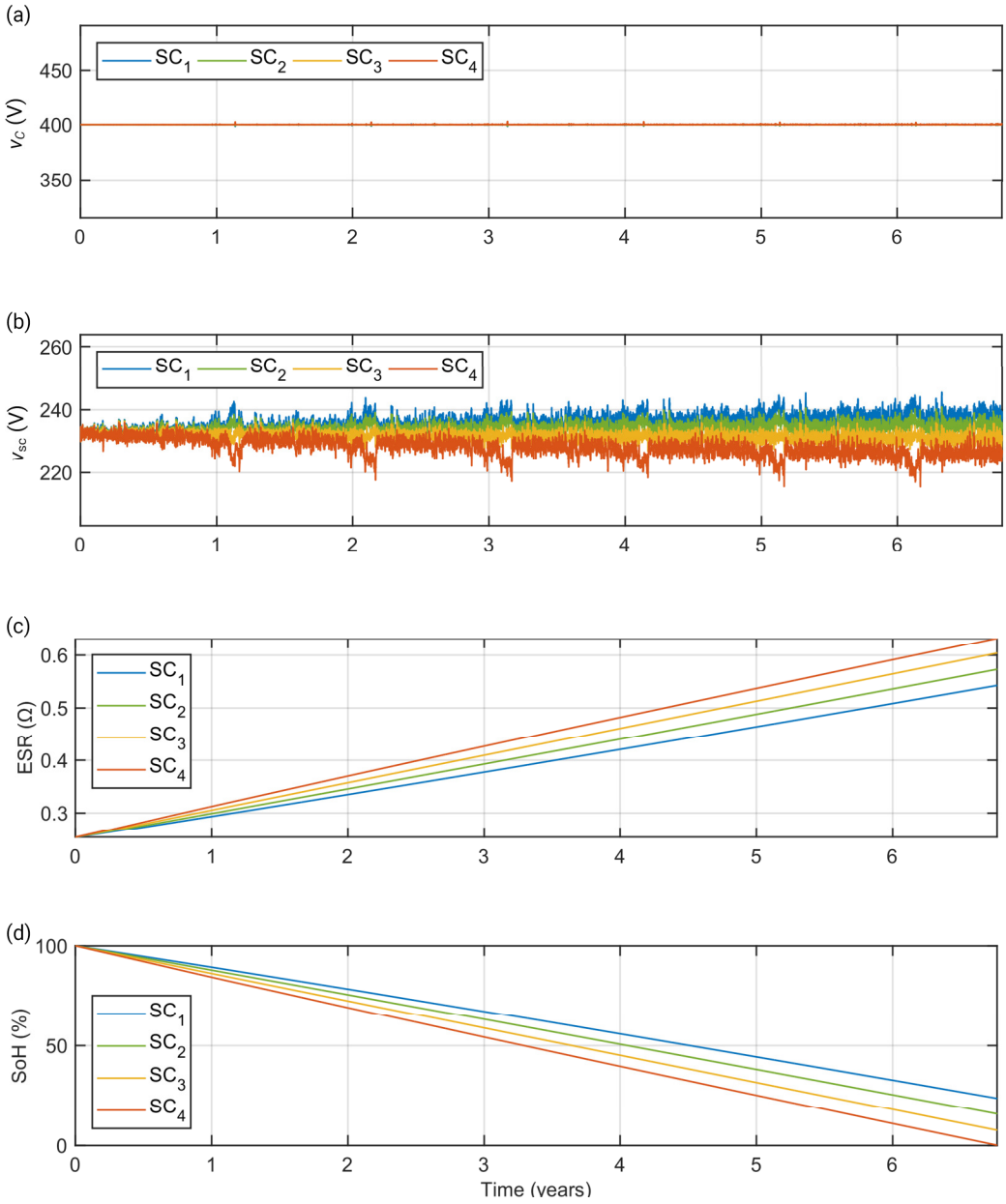

Fig. 4.22. (a) The output voltages of modular power converters with equally distributed converter reference voltage $V_{\text{ref},j}$; (b) The voltages of each supercapacitor groups; (c) Evolution of the ESR of the supercapacitor groups and (b) The SoH of the supercapacitor groups

In order to evaluate the benefits of the supercapacitor system lifetime optimization method, it has to be compared to a conventional case. In the SuperGrid Institute MMC with integrated supercapacitor energy storage case, the conventional case would be without the lifetime optimization method, i.e., the reference voltages that are used to control the converters are equally distributed. Like in the lifetime optimization case, it was assumed that there was a passive voltage-balancing system to keep cell voltages within the groups the same. Another simulation was run still following the

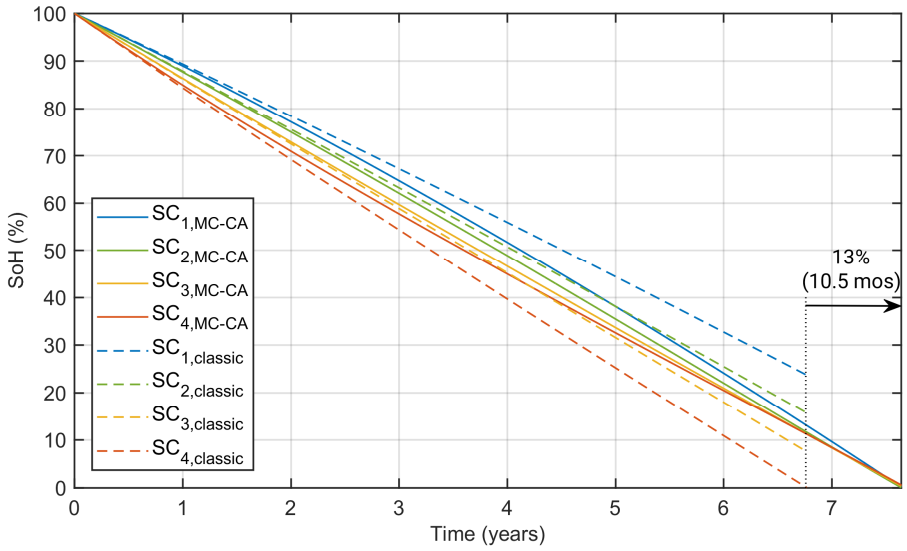

Fig. 4.23. Comparison of SoHs for the conventional (with equally distributed $V_{\text{ref},j}$) and modular converter (with lifetime optimization method) approaches

characteristic parameters in Table 4.3, but this time, $V_{\text{ref},j} = \frac{v_{Csm}^{u,l}}{N_{\text{mod}}} = 400$ V. The results of this simulation can be seen in Fig. 4.22. Fig. 4.22(a) shows the converter output voltages, which sure are held constant at 400 V and the supercapacitor group voltages are shown in Fig. 4.22(b). Because of the same initial characteristic parameters and of the different group temperatures, the individual capacitances and ESRs of the groups evolve differently. In fact, they diverge as seen in Fig. 4.22(c) for the ESRs and this is the effect of the different group temperatures. In turn, the different capacitances and ESRs cause the voltage imbalance seen in the supercapacitor group voltages. Because of the unequal voltages, one of the groups will sometimes reach the set SoE limits. For this reason, the voltage-balancing strategy also activates from time to time. The cumulative duration for voltage balancing is 2 months, which translates to a 2.5% active time. Overall, the SoH's of the groups also diverge, as seen in Fig. 4.22(d) with the SoH of the weakest group reaching 0% in 6.78 years.

A comparison of the control (classical) case with the proposed lifetime optimization method (modular converter approach) is shown in Fig. 4.23. Considering the SoH's, it is clear that the lifetime optimization method has a longer lifetime compared to the classical case. We can say that use of the method extends supercapacitor system life by 13% (or 10.5 months). A comparison with the Hybus project case can also be made. From the 42% improvement in Fig. 4.12(a), it is obvious that the benefits (13% improvement) in the present case of the SuperGrid Institute MMC with integrated supercapacitor energy storage is less. This is explained by the nature of the load profiles of the two cases. The Hybus project case has a high-test current level, while in this case, the current load profile is zero most of the

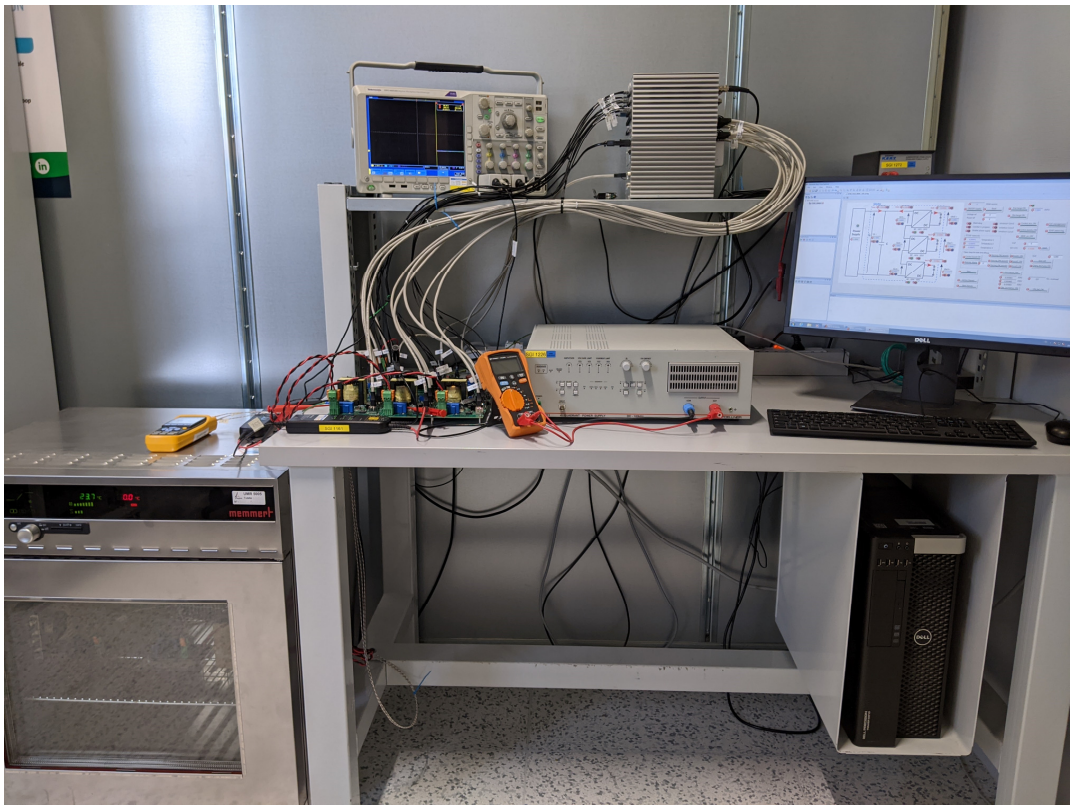

Fig. 4.24. Experimental setup of a small-scale prototype of modular converters with connected supercapacitors [32], [50]

time. The lifetime optimization method thus has no opportunity to also optimize the contribution of current to aging. This led to the lower improvement in the present case.

4.5.4 Experimental Results

To test the lifetime optimization method on the MMC with integrated supercapacitor energy storage, it was implemented on a small-scale 30 W ES-SM prototype by SuperGrid Institute [32], [50]. Fig. 4.24 shows the test bench composed of three modular power converters in a main motherboard that also includes the instrumentation, a Speedgoat real-time target machine, and a four-quadrant Toellner TOE 7621-40 power supply that has been programmed to simulate an MMC submodule, specifically the current that goes into the submodule capacitor and the modular converters. The Speedgoat machine is a field-programmable gate array (FPGA)-based target computer that serves as the main controller and as the control system in general. It connects to the workstation through a Simulink real-time explorer user interface. Through the latter, test specifications can be set and the ES-SM can be controlled. The experimental setup was the same one that was used in testing the voltage-balancing strategy in Subsection 2.5.1, so the modular converter and system specifications are the same as in Table 2.8. Note that the ES-SM in Subsection 4.5.3 had four modular power converters. In the current small-scale mock-up, there are only three.

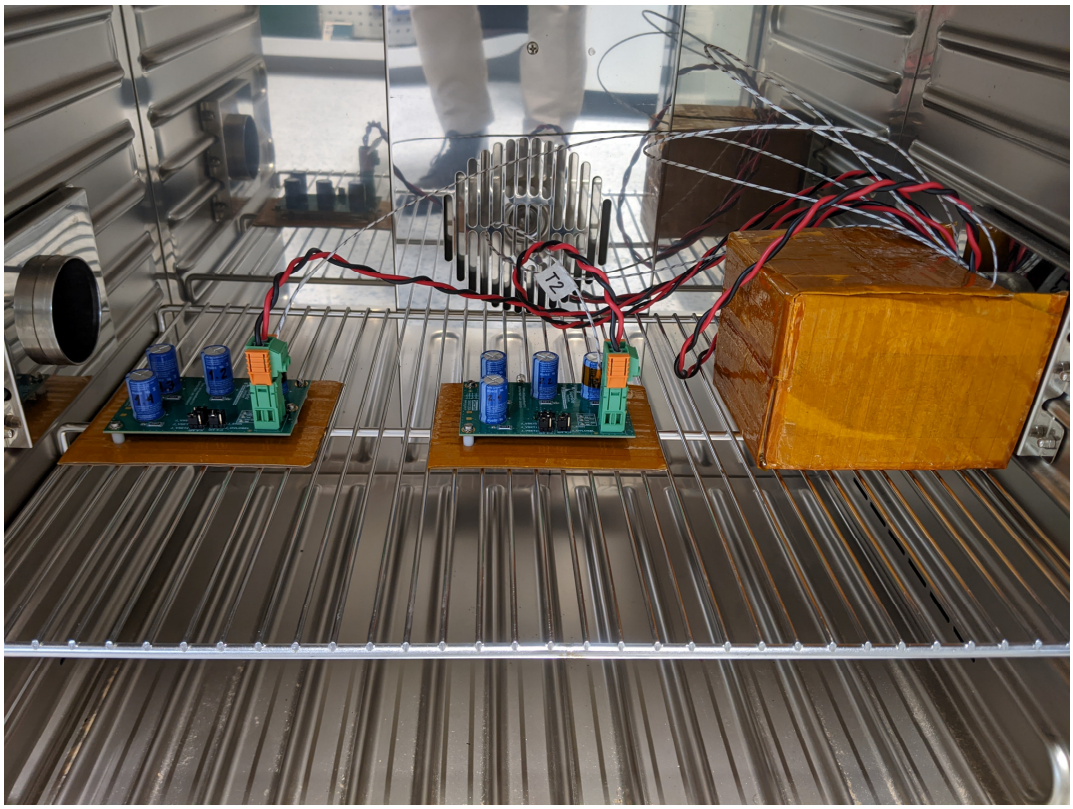

Fig. 4.25. The three daughterboards connected to the motherboard terminals through the wires going out of the oven vent; the temperature of one of each group's supercapacitors is measured by a thermocouple

Three daughterboards containing the supercapacitor cells under test are inside the Memmert UFP 500 universal oven, as seen in Fig. 4.25. They were put in the high-temperature environment of the oven to accelerate the aging of the cells. In other words, the experiment is a modified accelerated aging test because supercapacitor groups 1 and 2 are directly within the oven environment which was set at 80 °C and the last supercapacitor group, group 3, was covered by a box, as can be seen in Fig. 4.25. It is also covered by the same box, but the oven has a vent for the evacuation of air from inside the chamber. The box serves as a simple insulator between the oven chamber and supercapacitor group 3. This induces a temperature difference between supercapacitor groups 1 and 2 whose temperatures are set by the oven controls and the inside of the box which opens to the outside of the oven through the vent. This situation is needed in order to test the lifetime optimization method. The measured temperatures (in ranges) were recorded and are shown in Table 4.4. The temperature of supercapacitor group 3 is smaller and depends on the room temperature On average, group 3 is colder than the other two groups by 12.3 °C.

Table 4.4. Measured temperatures of the supercapacitors

Parameter		**SC group 1**	**SC group 2**	**SC group 3**
Temperature	(°C)	79.9–81.3	80.0–81.0	59.9–68.4

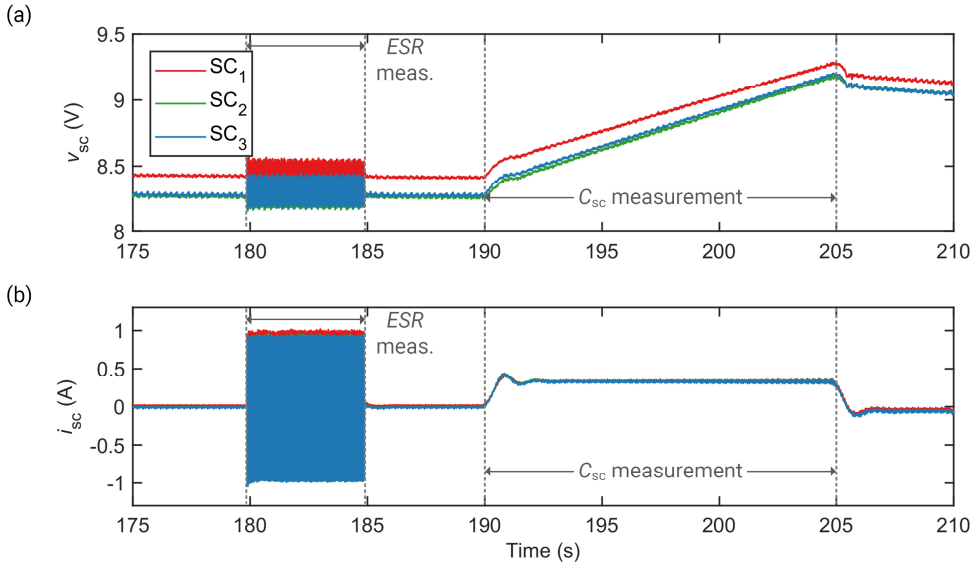

Fig. 4.26. Characterizing both ESR (180–185 s) and the capacitance (190–205 s): (a) Supercapacitor voltages and (b) Supercapacitor currents

A similar procedure as in the simulation of the previous subsection, Subsection 4.5.3, was followed. However, the current load profile was scaled down to the level of the small-scale prototype. In addition, the online characterization method of Subsection 3.3.2 was implemented to base the reliability indicator on the results of the online ESR characterization. However, it was found early on during the tests that the change in ESR values as the supercapacitors age is much slower than the change in the capacitance. This introduced a problem given the limited period that could be allocated for the accelerated aging test. If the supercapacitor reliability indicators were based on the measured ESRs, the effect of the lifetime optimization method would not be obvious. For this reason, it was decided that the equivalent capacitance of the supercapacitor groups would also be measured through a simple online constant-current charge method. Recall in Subsection 3.2.1 that this falls under the CCCD (constant-current charge/discharge) methods that take advantage of the increase/decrease in potential. In this particular implementation, the simple formula:

$$C_{\mathrm{sc}} = \frac{I_{\mathrm{sc}} \Delta t}{\Delta v_{\mathrm{sc}}} \tag{4.20}$$

It comes from the characteristic equation of a capacitor with a constant capacitance where I_{sc} is the constant current (A), $\Delta v_{\mathrm{sc}} = V_{\mathrm{b}} - V_{\mathrm{a}}$ is the voltage difference (V) between two measurement points a and b, and Δt is the time difference (s) between the two measurement points. An instance of characterization of both ESR and the capacitance is shown in Fig. 4.26. ESR is measured first using the online characterization method of Subsection 3.3.2. After 5 s, a constant current of $I_{\mathrm{sc}} = 400$ A was set

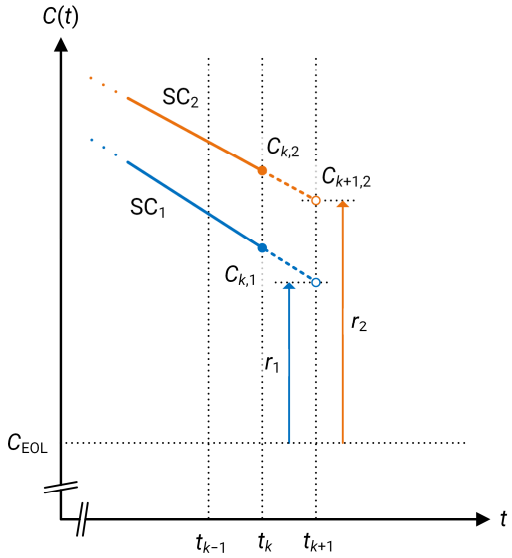

Fig. 4.27. The reliability indicators of two supercapacitors based on their present ($C_{k,j}$) and projected ($C_{k+1,j}$) capacitance values

for 15 s. The two measurement points are well within the 15 s because of the transients at either end of the period. The three supercapacitor groups were set to be characterized every 12 hours.

Because of the change in the supercapacitor characteristic that is measured from the ESR to the capacitance, the reliability indicator should be adapted as well. The reliability indicator in (4.18) that was based on the ESR was modified to:

$$r_j = C_{k+1,j} - C_{\text{EOL}} \tag{4.21}$$

This new capacitance-based reliability indicator accounts for the fact the capacitance decreases with time, unlike the ESR, which increases with time. The expression for ESR_{k+1} in (4.14) was first presented back in Subsection 4.4.2. Adapting it to the capacitance value at the next time step and simplifying gives us:

$$C_{k+1} = 2C_k - C_{\text{EOL}} \tag{4.22}$$

Both (4.21) and (4.22) are illustrated in Fig. 4.27. The resulting reliability indicators where $r_2 > r_1$ should similarly give us converter reference voltages where $V_{\text{ref},1} > V_{\text{ref},2}$ leading to supercapacitor voltages where $v_{\text{sc},2} > v_{\text{sc},1}$ similar to these quantities' trajectories we discussed back in Subsection 4.5.2.

Now that we have talked about characterization and adaptation of the reliability indicator to be based on the capacitance, let us turn our attention to the employment of the voltage-balancing strategy. Similar to the real ES-SM case, the voltage balancing kicks in when one of the supercapacitor groups

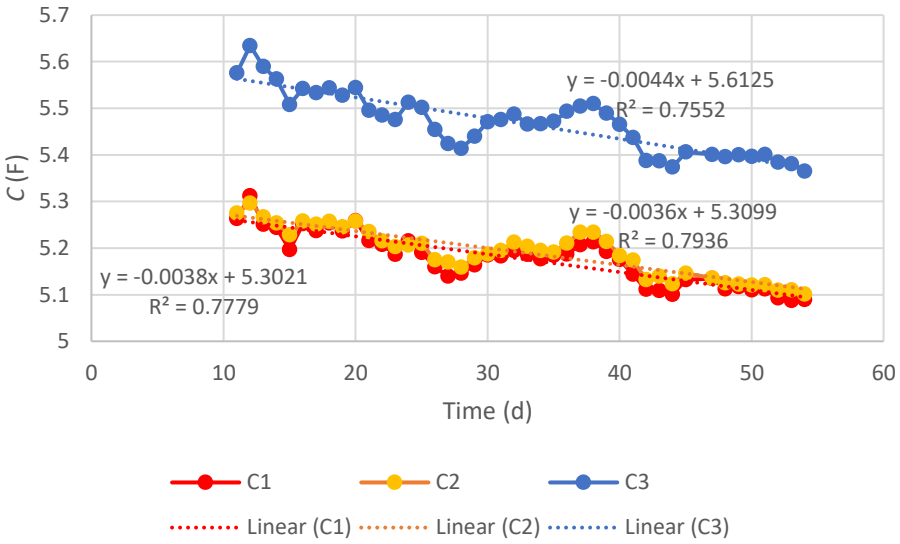

Fig. 4.28. Evolution of C_{sc} (moving average with a three-day window)

reaches the SoE limits and goes beyond SoE_{min} = 35% and SoE_{max} = 90%. Voltage balancing controls the modular converters until all groups return to an SoE_{ave} = 62.5%. However, the voltage-balancing strategy was also employed for another purpose. Recall that supercapacitor characterization happens every 12 hours. For proper characterization, the supercapacitors all have to be at the same voltage. For this reason, the voltage-balancing strategy was also used before every characterization. Fig. 4.26 is an example where group voltages were v_{sc} = 8.54 V (individual cell voltages of 2.14 V).

The experimental setup was run from February to April 2021. Fig. 4.28 shows the results of the capacitance measurements we made with a three-day moving averaging for each supercapacitor group. The signal is not stable due to the phenomenon of capacitance recovery as in Fig. 3.1. The Speedgoat target machine reset from time to time due to memory overload stopping the continuous operation of the setup and resetting the supercapacitor voltages resulting in capacitance recovery. In order to filter some of the noise, the three-day moving average was computed. Linear regression was then applied. The regression equations can also be seen in Fig. 4.28. Recall that group 3 is the strongest among all groups because its temperature is 12.3 °C lower than the two other groups, which are both nominally at 80 °C. It can be seen in the slopes of the lines that group 3 is aging faster than the other two. It is aging 19% faster even though it has the lowest temperature. The reason is group 3 is shouldering more of the electrical load as an increase in its voltage. This is similar to the simulation of a real ES-SM in Fig. 4.19(d).

To see how well the lifetime optimization works, we define here the parameter homogeneity H:

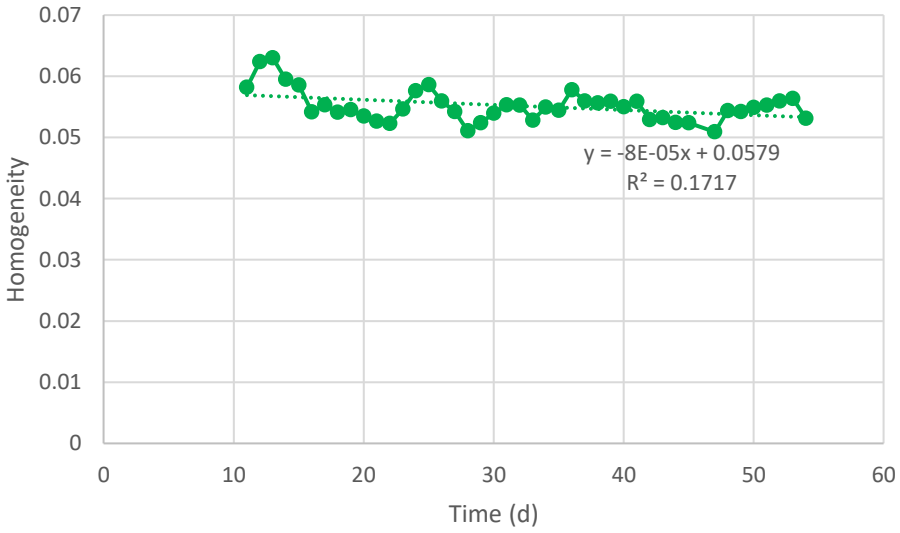

Fig. 4.29. Evolution of C_{sc} homogeneity

$$H = \frac{C_{max} - C_{min}}{C_{ave}} \tag{4.23}$$

where C_{max} is the maximum among all the measured capacitances, C_{min} is the minimum, and C_{ave} is the average of the measured capacitances. We have established in Subsection 4.5.3 that optimizing supercapacitor system life has the effect of balancing individual supercapacitor lifetimes. Here in (4.23), homogeneity is a measure of how balanced the capacitances are. However, we said in (4.17) in Subsection 4.4.3 that the SoH can be expressed either through the supercapacitor ESR or the capacitance, so the homogeneity that can be calculated from (4.23) is also a measure of how balanced the lifetimes are. Applying the formula to our results, we have Fig. 4.29. We can see that the regression line has a negative slope. This means that the data trend toward balancing or equalization of the group capacitances.

As mentioned, the supercapacitor groups' ESRs were also measured through the online ESR characterization method. Similar to the capacitances, three-day moving averaging was also applied to the data and the results are shown in Fig. 4.30. As is obvious, the ESRs are flatter and are therefore slow in terms of aging, even though it was already accelerated. Also notable is the behavior of the ESR of group 3. The slope of its regression line shows that its aging is 4.5 times slower than the slopes of the other two groups. This means that if the lifetime optimization method was based on the ESR instead, control saturation would likely ensue given how slow group 3's ESR ages. This means that for the ESR, even if group 3 shoulders the bulk of the electrical load, it still would not be enough to make up for the temperature differences among the groups. Given the slopes in Fig. 4.30, we can see that a homogeneity formula version for the ESR will give us an increasing homogeneity slope, which means that the ESR

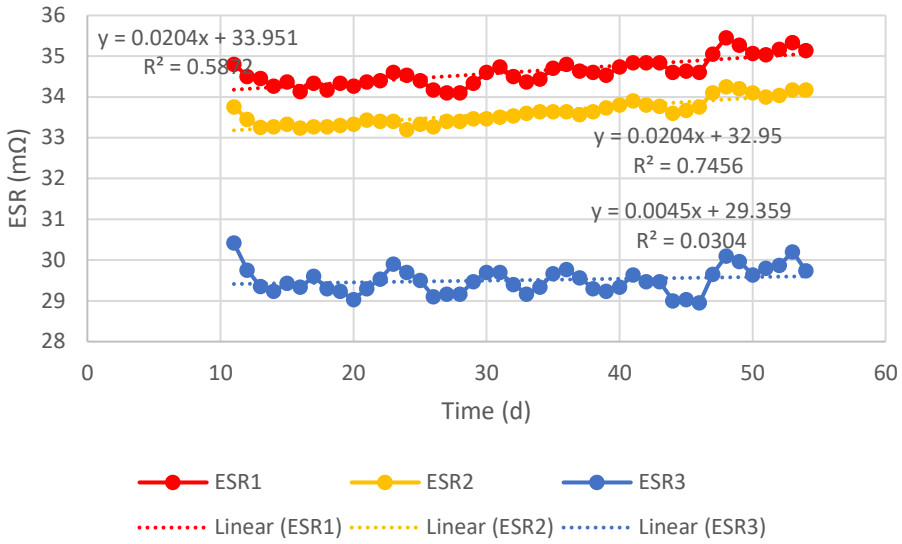

Fig. 4.30. Evolution of *ESR* (moving average with a three-day window)

could not be balanced or equalized given the present specifications. Another possibility is that because the ESR ages much slowly than the capacitance, it slows down the control producing the same effect on the evolution of the group ESRs.

4.6 Conclusion

We have shown how important it is to solve the problem of uneven aging among supercapacitor cells. The reliability of an energy storage system using supercapacitors depends on it. Solving the problem also has the additional benefit of extending the system lifetime, which then results in reduced costs and savings. We have proposed in this chapter a novel method of balancing that uses modular power converters to control the loading of supercapacitor cells based on SoH. Conventional balancing methods are based on SoC and do not directly optimize system lifetime. We demonstrated how the new method operates through modeling and simulation. Control allocation based on the supercapacitor remaining life as the reliability indicator is at its core. While there remains work to improve the modeling and simulation, the results are positive given the present specifications. They show that the use modular power converters can balance the SoH's of the supercapacitors and significantly extend overall system lifetime.

General Conclusion

The work presented in this thesis studied the improvement in supercapacitor system lifetime by optimizing the control of connected modular power converters. Two applications have served as case studies for the control methods developed to achieve this goal: (i) trolleybus auxiliaries supply based on supercapacitors in the Hybus project and (ii) MMCs with integrated supercapacitor energy storage by the SuperGrid Institute.

This thesis can be summarized in three contributions that appear as the main chapters:

1. Development of a control saturation-adapted energy-based voltage-balancing strategy. This control strategy was a new contribution itself and was also integral in accomplishing the third point on lifetime optimization.

2. Development of online supercapacitor characterization methods that can provide supercapacitor capacitance and ESR measurements over time. This again is an integral step in accomplishing the next point on lifetime optimization.

3. Development of a supercapacitor system lifetime optimization method based on measured online characteristics and whose operation is integrated with the voltage-balancing strategy in the first point.

The first chapter of this thesis presented a general overview of energy storage and the need for it for a decarbonized future, the next chapters threshed out the three-point contribution of this thesis.

Chapter 2 first presented the base system architecture that we have worked with throughout the thesis. It described how supercapacitors as energy storage, the modular power converters, and the application are all connected. We also provided the basic control system for the architecture. This chapter also expounded on the problem of control saturation and how our new control strategy can adapt to it. Both simulations and experiments were conducted and results show that the proposed control saturation-adapted voltage-balancing strategy works.

The third chapter explained the characteristics of supercapacitors. We also talked about the different methods of characterization and the requisite experimental setup. Because of the nature of our applications, an online characterization method was needed. A proposed EIS-like method for batteries in the literature was adapted for supercapacitors for our purposes. Experiments were conducted to show the workings of the method and to demonstrate how it can be used for our applications.

The fourth chapter forms the core of this thesis. As mentioned, the last two chapters and their contributions were in service of this chapter. The two applications and how their respective energy storage's lifetimes could be extended were discussed in this chapter. Supercapacitor aging models were first presented. Next presented was the control allocation method and how it considers supercapacitor reliability in order to optimize the system life. For the two applications, they were both modeled and simulated. However, because of the time constraints for the accelerated aging test, only experiments for the MMC with integrated supercapacitor energy storage were conducted. Nonetheless, both simulation for the two applications and the experiments for the latter show that supercapacitor system lifetime can be extended. The improvement level, however, depends on the specific application context and specifications.

Future Work

Results presented in this thesis show that the proposed methods of control, illustrated in the last three chapters, for balancing of supercapacitor voltages, characterization of supercapacitor cells, and optimization of supercapacitor system life work. While true, there remain significant and quite consequential lines of inquiry for future work in this topic in order to realize the objective of employing lifetime optimization in industrial applications of energy storage as a standard control strategy. The following are some subjects resulting directly from the conduct of research for this thesis that may be of interest for future work:

- While the voltage-balancing, characterization, and lifetime optimization methods are, theoretically, applicable in any energy storage system composed of cells, it remains an imperative that they be demonstrated in such cases. It would be ideal to have a similar study for batteries, which are a more popular energy storage choice for different applications because of the higher energy density. The relatively flat voltage curve of batteries (open-circuit voltage $v_{\mathrm{oc}} = f(SoC)$) on their operational range may present itself as an advantage in terms of the lifetime optimization method and its limits in control saturation. It was mentioned in Subsection 2.3.2 that the large operational voltage range of supercapacitors is one reason for control saturation.

- Different definitions for the reliability indicator were used in Subsections 4.4.2 and 4.5.2 for the two different applications. The reason was that the Hybus and MMC applications had different load profiles. The former had a current-heavy load while the opposite was true for the latter. In real applications, it may be difficult to characterize whether the load profile is current-heavy or not. Another possibility is that an application could be both: interchanging between being

current-heavy and current-light, one at a time. It is similarly hard to choose which reliability indicator definition to use. A future study on a general lifetime optimization method with a general reliability indicator definition is thus warranted.

- Another issue related to the structure of the control method itself is the indirect control of supercapacitor voltages through the converter reference voltages, which was expounded in Subsection 2.2.1. For the purpose of balancing supercapacitor voltages, these converter reference voltages were made to come from the energy-based voltage-balancing strategy, while for the purpose of optimizing supercapacitor system life, they were managed by the control allocation method in Section 4.3. However, it can be observed that the technique was indirect in the sense that what was directly controlled was the converter output voltage and not the associated supercapacitor voltage. This is another fruitful line of inquiry that could also help avoid the need for the voltage-balancing strategy from time to time.

- It was mentioned in Subsection 4.5.4 the challenge in using supercapacitor ESRs in the lifetime optimization method because of its slow evolution even under an accelerated aging test. Because of time constraints, we decided in this thesis to use online measurements of the capacitance instead of the ESR. It would be ideal if more time could be given to the accelerated aging test so that the lifetime optimization method can applied to the ESR as well. This should settle the issue of using ESR under normal operating conditions.

As the points above show, there remain technical issues that need to be addressed by future work on this topic. The successful use of the lifetime optimization method as a standard control method for energy storage systems hinges on them. However, as this thesis has shown, the method can bring about promising results depending on the individual application context. This thesis has highlighted what the lifetime optimization method can contribute towards extending an energy storage system's end of life.

Bibliography

[1] "Goal 7 | Department of Economic and Social Affairs." https://sdgs.un.org/goals/goal7 (accessed Jul. 19, 2022).

[2] "The Paris Agreement | UNFCCC." https://unfccc.int/process-and-meetings/the-paris-agreement/the-paris-agreement (accessed Apr. 15, 2022).

[3] "Climate Change 2021: The Physical Science Basis," Intergovernmental Panel on Climate Change (IPCC), Aug. 2021. [Online]. Available: https://www.ipcc.ch/report/ar6/wg1/downloads/report/IPCC_AR6_WGI_SPM_final.pdf

[4] A. Alleyne, "Power Density as the Key Enabler for Electrified Mobility," *Polytechnica*, vol. 1, no. 1–2, pp. 10–18, Oct. 2018, doi: 10.1007/s41050-018-0002-4.

[5] "Verkor selects Dunkirk for its first Gigafactory," *Verkor*, Feb. 01, 2022. https://verkor.com/en/verkor-selects-dunkirk-for-its-first-gigafactory/ (accessed Apr. 06, 2022).

[6] "Northvolt - the future of energy," Jan. 20, 2021. https://northvolt.com/ (accessed Apr. 06, 2022).

[7] "Decarbonizing transportation and energy systems...," *FREYR Battery Norway*. https://www.freyrbattery.com/ (accessed Apr. 06, 2022).

[8] "Tesla Gigafactory | Tesla." https://www.tesla.com/gigafactory (accessed Apr. 06, 2022).

[9] M. M. Rahman, A. O. Oni, E. Gemechu, and A. Kumar, "Assessment of energy storage technologies: A review," *Energy Conversion and Management*, vol. 223, p. 113295, Nov. 2020, doi: 10.1016/j.enconman.2020.113295.

[10] A. Rufer, *Energy Storage: Systems and Components*. Boca Raton, FL, USA: CRC Press, Taylor & Francis Group, 2018. Accessed: Mar. 21, 2018. [Online]. Available: https://www.crcpress.com/Energy-Storage-Systems-and-Components/Rufer/p/book/9781138082625

[11] D. Linzen, S. Buller, E. Karden, and R. W. DeDoncker, "Analysis and Evaluation of Charge-Balancing Circuits on Performance, Reliability, and Lifetime of Supercapacitor Systems," *IEEE Transactions on Industry Applications*, vol. 41, no. 5, pp. 1135–1141, Sep. 2005, doi: 10.1109/TIA.2005.853375.

[12] P. Kreczanik, P. Venet, A. Hijazi, and G. Clerc, "Study of Supercapacitor Aging and Lifetime Estimation According to Voltage, Temperature, and RMS Current," *IEEE Transactions on Industrial Electronics*, vol. 61, no. 9, pp. 4895–4902, Sep. 2014, doi: 10.1109/TIE.2013.2293695.

[13] F. M. Ibanez, "Analyzing the Need for a Balancing System in Supercapacitor Energy Storage Systems," *IEEE Transactions on Power Electronics*, vol. 33, no. 3, pp. 2162–2171, Mar. 2018, doi: 10.1109/TPEL.2017.2697406.

[14] F. Béguin and E. Frackowiak, *Supercapacitors: Materials, Systems, and Applications*. Weinheim, Germany: Wiley-VCH Verlag GmbH & Co., 2013.

[15] L. Zhang, X. Hu, Z. Wang, F. Sun, and D. G. Dorrell, "A review of supercapacitor modeling, estimation, and applications: A control/management perspective," *Renewable and Sustainable Energy Reviews*, vol. 81, pp. 1868–1878, Jan. 2018, doi: 10.1016/j.rser.2017.05.283.

[16] Y. Diab, P. Venet, and G. Rojat, "Comparison of the Different Circuits Used for Balancing the Voltage of Supercapacitors: Studying Performance and Lifetime of Supercapacitors," in *Proc. 2nd European Symposium on Super Capacitors and Applications (ESSCAP'06)*, Lausanne, Switzerland, Nov. 2006. Accessed: Apr. 25, 2018. [Online]. Available: https://hal.archives-ouvertes.fr/hal-00411482

[17] J. Cao, N. Schofield, and A. Emadi, "Battery balancing methods: A comprehensive review," presented at the 2008 IEEE Vehicle Power and Propulsion Conference (VPPC), Harbin, China, Sep. 2008, pp. 1–6. doi: 10.1109/VPPC.2008.4677669.

[18] M. M. Hoque, M. A. Hannan, A. Mohamed, and A. Ayob, "Battery charge equalization controller in electric vehicle applications: A review," *Renewable and Sustainable Energy Reviews*, vol. 75, pp. 1363–1385, Aug. 2017, doi: 10.1016/j.rser.2016.11.126.

[19] F. Altaf, L. Johannesson, and B. Egardt, "On Thermal and State-of-Charge Balancing using Cascaded Multi-level Converters," *Journal of Power Electronics*, vol. 13, no. 4, pp. 569–583, Jul. 2013, doi: 10.6113/JPE.2013.13.4.569.

[20] W. Huang and J. A. Abu Qahouq, "Energy Sharing Control Scheme for State-of-Charge Balancing of Distributed Battery Energy Storage System," *IEEE Transactions on Industrial Electronics*, vol. 62, no. 5, pp. 2764–2776, May 2015, doi: 10.1109/TIE.2014.2363817.

[21] N. Mukherjee, D. Strickland, and M. Abedi Varnosfaderani, "Adaptive Control of Hybrid Battery Energy Storage Systems under Capacity Fade," *EPE Journal*, vol. 25, no. 4, pp. 25–33, Oct. 2015, doi: 10.1080/0939-8368.2015.11882293.

[22] N. Mukherjee and D. Strickland, "Control of Cascaded DC–DC Converter-Based Hybrid Battery Energy Storage Systems—Part I: Stability Issue," *IEEE Transactions on Industrial Electronics*, vol. 63, no. 4, pp. 2340–2349, 2016.

[23] N. Mukherjee and D. Strickland, "Control of Cascaded DC–DC Converter-Based Hybrid Battery Energy Storage Systems—Part II: Lyapunov Approach," *IEEE Transactions on Industrial Electronics*, vol. 63, no. 5, pp. 3050–3059, 2016.

[24] M. Evzelman, M. M. U. Rehman, K. Hathaway, R. Zane, D. Costinett, and D. Maksimovic, "Active Balancing System for Electric Vehicles With Incorporated Low-Voltage Bus," *IEEE Transactions on Power Electronics*, vol. 31, no. 11, pp. 7887–7895, Nov. 2016, doi: 10.1109/TPEL.2015.2513432.

[25] F. Altaf, B. Egardt, and L. Johannesson Mardh, "Load Management of Modular Battery Using Model Predictive Control: Thermal and State-of-Charge Balancing," *IEEE Transactions on*

Control Systems Technology, vol. 25, no. 1, pp. 47–62, Jan. 2017, doi: 10.1109/TCST.2016.2547980.

[26] F. Altaf and B. Egardt, "Comparative Analysis of Unipolar and Bipolar Control of Modular Battery for Thermal and State-of-Charge Balancing," *IEEE Transactions on Vehicular Technology*, vol. 66, no. 4, pp. 2927–2941, Apr. 2017, doi: 10.1109/TVT.2016.2587720.

[27] A. Hijazi *et al.*, "Sizing of supercapacitors stack: Application to the braking energy recovery of electrical bus," in *Proc. 4th European Symposium on Super Capacitors and Applications (ESSCAP'10)*, Bordeaux, France, Oct. 2010, pp. ES10-37.

[28] F. Errigo *et al.*, "Assessment of Aging and Performance Degradation of Supercapacitors Integrated into a Modular Multilevel Converter," presented at the 2020 22nd European Conference on Power Electronics and Applications (EPE'20 ECCE Europe), Lyon, France, Sep. 2020.

[29] F. Errigo, T. Lagier, L. Chédot, A. Sari, and P. Venet, "Multi-Level Voltage Converter with Optimised Additional Energy Storage," WO2020225332A1, Nov. 12, 2020

[30] D. Montesinos-Miracle, M. Massot-Campos, J. Bergas-Jane, S. Galceran-Arellano, and A. Rufer, "Design and Control of a Modular Multilevel DC/DC Converter for Regenerative Applications," *IEEE Transactions on Power Electronics*, vol. 28, no. 8, pp. 3970–3979, Aug. 2013, doi: 10.1109/TPEL.2012.2231702.

[31] A. Hijazi, P. Kreczanik, E. Bideaux, P. Venet, G. Clerc, and M. Di Loreto, "Thermal Network Model of Supercapacitors Stack," *IEEE Transactions on Industrial Electronics*, vol. 59, no. 2, pp. 979–987, Feb. 2012, doi: 10.1109/TIE.2011.2158769.

[32] F. Errigo, "Convertisseurs de puissance avec stockage d'énergie intégré pour réseaux haute tension à courant continu," PhD thesis, Université Claude Bernard Lyon 1, Université de Lyon, Villeurbanne, France, 2020.

[33] R. Kötz, P. W. Ruch, and D. Cericola, "Aging and failure mode of electrochemical double layer capacitors during accelerated constant load tests," *Journal of Power Sources*, vol. 195, no. 3, pp. 923–928, Feb. 2010, doi: 10.1016/j.jpowsour.2009.08.045.

[34] T. Kovaltchouk, B. Multon, H. Ben Ahmed, J. Aubry, and P. Venet, "Enhanced Aging Model for Supercapacitors Taking Into Account Power Cycling: Application to the Sizing of an Energy Storage System in a Direct Wave Energy Converter," *IEEE Trans. on Ind. Applicat.*, vol. 51, no. 3, pp. 2405–2414, May 2015, doi: 10.1109/TIA.2014.2369817.

[35] S. Liu, L. Wei, and H. Wang, "Review on reliability of supercapacitors in energy storage applications," *Applied Energy*, vol. 278, p. 115436, Nov. 2020, doi: 10.1016/j.apenergy.2020.115436.

[36] "Maxwell Technologies BOOSTCAP Energy Storage Module Life Duration Estimation," Maxwell Technologies, Inc., Application Note, 2007. Accessed: Apr. 13, 2018. [Online]. Available: http://www.maxwell.com/images/documents/applicationnote_1012839_1.pdf

[37] S. Zhang and N. Pan, "Supercapacitors Performance Evaluation," *Advanced Energy Materials*, vol. 5, no. 6, p. 1401401, Mar. 2015, doi: 10.1002/aenm.201401401.

[38] B. E. Conway, *Electrochemical supercapacitors: scientific fundamentals and technological applications*. New York: Springer Science+Business Media, 1999.

[39] G. Ellis, *Observers in Control Systems: A Practical Guide*. Elsevier, 2002.

[40] S. Shili, A. Hijazi, A. Sari, P. Bevilacqua, and P. Venet, "Online supercapacitor health monitoring using a balancing circuit," *Journal of Energy Storage*, vol. 7, pp. 159–166, Aug. 2016, doi: 10.1016/j.est.2016.06.004.

[41] W. Huang and J. A. Qahouq, "An Online Battery Impedance Measurement Method Using DC–DC Power Converter Control," *IEEE Transactions on Industrial Electronics*, vol. 61, no. 11, pp. 5987–5995, Nov. 2014, doi: 10.1109/TIE.2014.2311389.

[42] J. A. A. Qahouq and Z. Xia, "Single-Perturbation-Cycle Online Battery Impedance Spectrum Measurement Method With Closed-Loop Control of Power Converter," *IEEE Transactions on Industrial Electronics*, vol. 64, no. 9, pp. 7019–7029, Sep. 2017, doi: 10.1109/TIE.2017.2686324.

[43] P. Kreczanik, "Étude de la fiabilité et du vieillissement d'un système de stockage par supercondensateurs pour l'alimentation partielle et ponctuelle d'un trolleybus grâce à la récupération de l'énergie de freinage: approche du composant au système de stockage," PhD thesis, Université Claude Bernard Lyon 1, Université de Lyon, Villeurbanne, France, 2011.

[44] A. Hijazi, "Modélisation électrothermique, commande et dimensionnement d'un système de stockage d'énergie par supercondensateurs avec prise en compte de son vieillissement: application à la récupération de l'énergie de freinage d'un trolleybus," PhD thesis, Université Claude Bernard Lyon 1, Université de Lyon, Villeurbanne, France, 2010.

[45] A. Khelassi, D. Theilliol, and P. Weber, "Control design for over-actuated systems based on reliability indicators," presented at the UKACC International Conference on CONTROL 2010, 2010, pp. 536–541. doi: 10.1049/ic.2010.0339.

[46] A. Khelassi, J. Jiang, D. Theilliol, P. Weber, and Y. M. Zhang, "Reconfiguration of Control Inputs for overactuated Systems based on Actuators health," in *IFAC Proceedings Volumes*, Jan. 2011, vol. 44, pp. 13729–13734. doi: 10.3182/20110828-6-IT-1002.02174.

[47] S. Shili, A. Hijazi, A. Sari, X. Lin-Shi, and P. Venet, "Balancing Circuit New Control for Supercapacitor Storage System Lifetime Maximization," *IEEE Transactions on Power Electronics*, vol. 32, no. 6, pp. 4939–4948, Jun. 2017, doi: 10.1109/TPEL.2016.2602393.

[48] J. Jorgenson, A. W. Frazier, P. Denholm, and N. Blair, "Storage Futures Study: Grid Operational Impacts of Widespread Storage Deployment," NREL/TP-6A40-80688, 1840718, MainId:77472, Jan. 2022. doi: 10.2172/1840718.

[49] K. Sharifabadi, L. Harnefors, H.-P. Nee, S. Norrga, and R. Teodorescu, *Design, Control and Application of Modular Multilevel Converters for HVDC Transmission Systems*. Chichester, UK: John Wiley & Sons, Ltd, 2016. doi: 10.1002/9781118851555.

[50] F. Errigo, F. Morel, C. Mathieu de Vienne, L. Chedot, A. Sari, and P. Venet, "A Submodule with Integrated Supercapacitors for HVDC-MMC providing Fast Frequency Response," *IEEE Trans. Power Delivery*, pp. 1–1, 2022, doi: 10.1109/TPWRD.2021.3086864.

[51] "Climate Change 2022: Mitigation of Climate Change," Intergovernmental Panel on Climate Change, Apr. 2022. Accessed: Apr. 15, 2022. [Online]. Available: https://www.ipcc.ch/report/sixth-assessment-report-working-group-3/

[52] "France 2030," *elysee.fr*, Mar. 20, 2022. https://www.elysee.fr/emmanuel-macron/france2030 (accessed Apr. 04, 2022).

[53] "Découvrez les aides pour votre voiture électrique | Je-roule-en-electrique.fr." https://www.je-roule-en-electrique.fr/decouvrez-les-aides-pour-votre-voiture-electrique-13 (accessed Apr. 04, 2022).

[54] "Incentives for buying an electric car in France: how do they work? - Renault Group." https://www.renaultgroup.com/en/news-on-air/news/incentives-for-buying-an-electric-car-in-france-how-do-they-work/ (accessed Apr. 04, 2022).

[55] E. Kohn, Huang, N. Kong, and S. Hardman, "Electric Vehicle Incentives in 15 Leading Electric Vehicle Markets," University of California, Davis, Jan. 2022. [Online]. Available: https://escholarship.org/uc/item/0tn2p4x6

[56] "Energy Storage Grand Challenge Energy Storage Market Report," U.S. Department of Energy, Dec. 2020.

[57] "Lithium Ion Battery Market Size & Share, Forecast Report 2020–2026," *Global Market Insights Inc.* https://www.gminsights.com/industry-analysis/lithium-ion-battery-market (accessed Apr. 16, 2022).

[58] "Supercapacitor Market Size & Share, Forecast Report 2027," *Global Market Insights Inc.* https://www.gminsights.com/industry-analysis/supercapacitor-market (accessed Apr. 16, 2022).

[59] S. Koohi-Fayegh and M. A. Rosen, "A review of energy storage types, applications and recent developments," *Journal of Energy Storage*, vol. 27, p. 101047, Feb. 2020, doi: 10.1016/j.est.2019.101047.

[60] M. Şahin, F. Blaabjerg, and A. Sangwongwanich, "A Comprehensive Review on Supercapacitor Applications and Developments," *Energies*, vol. 15, no. 3, p. 674, Jan. 2022, doi: 10.3390/en15030674.

[61] J. Leuchter, P. Bauer, P. Bojda, and V. Rerucha, "Bi-directional DC-DC converters for supercapacitor based energy buffer for electrical gen-sets," in *2007 European Conference on*

Power Electronics and Applications, Aalborg, Denmark, 2007, pp. 1–10. doi: 10.1109/EPE.2007.4417437.

[62] M. B. Camara, H. Gualous, F. Gustin, A. Berthon, and B. Dakyo, "DC/DC Converter Design for Supercapacitor and Battery Power Management in Hybrid Vehicle Applications—Polynomial Control Strategy," *IEEE Transactions on Industrial Electronics*, vol. 57, no. 2, pp. 587–597, Feb. 2010, doi: 10.1109/TIE.2009.2025283.

[63] A. S. Samosir and A. H. M. Yatim, "Implementation of Dynamic Evolution Control of Bidirectional DC–DC Converter for Interfacing Ultracapacitor Energy Storage to Fuel-Cell System," *IEEE Transactions on Industrial Electronics*, vol. 57, no. 10, pp. 3468–3473, Oct. 2010, doi: 10.1109/TIE.2009.2039458.

[64] P. J. Grbović, *Ultra-capacitors in power conversion systems: applications, analysis and design from theory and practice*. Chichester, West Sussex, United Kingdom: IEEE Press/ Wiley, 2014.

[65] N. Mukherjee and D. Strickland, "Analysis and Comparative Study of Different Converter Modes in Modular Second-Life Hybrid Battery Energy Storage Systems," *IEEE J. Emerg. Sel. Topics Power Electron.*, vol. 4, no. 2, pp. 547–563, Jun. 2016, doi: 10.1109/JESTPE.2015.2460334.

[66] H. R. Karshenas, H. Daneshpajooh, A. Safaee, P. Jain, and A. Bakhshai, "Bidirectional DC - DC Converters for Energy Storage Systems," in *Energy Storage in the Emerging Era of Smart Grids*, R. Carbone, Ed. InTech, 2011. doi: 10.5772/23494.

[67] R. Kötz *et al.*, "Voltage balancing: Long-term experience with the 250V supercapacitor module of the hybrid fuel cell vehicle HY-LIGHT," *Journal of Power Sources*, vol. 174, no. 1, pp. 264–271, Nov. 2007, doi: 10.1016/j.jpowsour.2007.08.078.

[68] R. A. S. Peña, A. Hijazi, P. Venet, and F. Errigo, "Balancing Supercapacitor Voltages in Modular Bidirectional DC–DC Converter Circuits," *IEEE Trans. Power Electron.*, vol. 37, no. 1, pp. 137–149, Jan. 2022, doi: 10.1109/TPEL.2021.3093767.

[69] N. Devillers, S. Jemei, M.-C. Péra, D. Bienaimé, and F. Gustin, "Review of characterization methods for supercapacitor modelling," *Journal of Power Sources*, vol. 246, pp. 596–608, Jan. 2014, doi: 10.1016/j.jpowsour.2013.07.116.

[70] M. Mellincovsky *et al.*, "Performance assessment of a power loaded supercapacitor based on manufacturer data," *Energy Conversion and Management*, vol. 76, pp. 137–144, Dec. 2013, doi: 10.1016/j.enconman.2013.07.042.

[71] M. Mellincovsky *et al.*, "Performance and Limitations of a Constant Power-Fed Supercapacitor," *IEEE Transactions on Energy Conversion*, vol. 29, no. 2, pp. 445–452, Jun. 2014, doi: 10.1109/TEC.2013.2296792.

[72] F. Odeim, J. Roes, and A. Heinzel, "Power Management Optimization of an Experimental Fuel Cell/Battery/Supercapacitor Hybrid System," *Energies*, vol. 8, no. 7, pp. 6302–6327, Jun. 2015, doi: 10.3390/en8076302.

[73] M. Ceraolo, G. Lutzemberger, and D. Poli, "State-Of-Charge Evaluation Of Supercapacitors," *Journal of Energy Storage*, vol. 11, pp. 211–218, Jun. 2017, doi: 10.1016/j.est.2017.03.001.

[74] "Product Guide: Maxwell Technologies BOOTSCAP Ultracapacitors," Maxwell Technologies, Inc., Product Guide, 2009.

[75] R. W. Erickson and D. Maksimović, *Fundamentals of Power Electronics*, 3rd ed. Cham, Switzerland: Springer International Publishing, 2020. doi: 10.1007/978-3-030-43881-4.

[76] M. Bhardwaj, "Modeling Bi-Directional Buck/Boost Converter for Digital Control Using C2000 Microcontrollers," Texas Instruments Inc., Application Report, Jan. 2015. Accessed: Nov. 24, 2017. [Online]. Available: http://www.ti.com/lit/an/sprabx5/sprabx5.pdf

[77] Y. Diab, P. Venet, H. Gualous, and G. Rojat, "Self-Discharge Characterization and Modeling of Electrochemical Capacitor Used for Power Electronics Applications," *IEEE Transactions on Power Electronics*, vol. 24, no. 2, pp. 510–517, Feb. 2009, doi: 10.1109/TPEL.2008.2007116.

[78] "Murata Supercapacitor Technical Note," Murata Manufacturing Co., Ltd., Technical Note, 2014. Accessed: Apr. 13, 2018. [Online]. Available: https://www.murata.com/~/media/webrenewal/products/capacitor/edlc/techguide/electrical/c2m1cxs-053.ashx?la=en

[79] "Test Procedures for Capacitance, ESR, Leakage Current and Self-Discharge Characterizations of Ultracapacitors," Maxwell Technologies, Inc., Application Note, Jun. 2015.

[80] S. Ratha and A. K. Samantara, *Supercapacitor: Instrumentation, Measurement and Performance Evaluation Techniques*. Singapore: Springer Singapore, 2018. doi: 10.1007/978-981-13-3086-5.

[81] B.-A. Mei, O. Munteshari, J. Lau, B. Dunn, and L. Pilon, "Physical Interpretations of Nyquist Plots for EDLC Electrodes and Devices," *J. Phys. Chem. C*, vol. 122, no. 1, pp. 194–206, Jan. 2018, doi: 10.1021/acs.jpcc.7b10582.

[82] R. German, P. Venet, A. Sari, O. Briat, and J. M. Vinassa, "Comparison of EDLC impedance models used for ageing monitoring," in *2012 First International Conference on Renewable Energies and Vehicular Technology*, Hammamet, Mar. 2012, pp. 224–229. doi: 10.1109/REVET.2012.6195275.

[83] R. German, "Étude du vieillissement calendaire des supercondensateurs et impact des ondulations de courant haute fréquence," PhD thesis, Université Claude Bernard Lyon 1, Université de Lyon, Villeurbanne, France, 2013.

[84] F. Rafik, H. Gualous, R. Gallay, A. Crausaz, and A. Berthon, "Frequency, thermal and voltage supercapacitor characterization and modeling," *Journal of Power Sources*, vol. 165, no. 2, pp. 928–934, Mar. 2007, doi: 10.1016/j.jpowsour.2006.12.021.

[85] S. Buller, M. Thele, R. W. A. A. DeDoncker, and E. Karden, "Impedance-Based Simulation Models of Supercapacitors and Li-Ion Batteries for Power Electronic Applications," *IEEE Trans. on Ind. Applicat.*, vol. 41, no. 3, pp. 742–747, May 2005, doi: 10.1109/TIA.2005.847280.

[86] R. Srinivasan and F. Fasmin, *An Introduction to Electrochemical Impedance Spectroscopy*. CRC Press, 2021.

[87] A. Lasia, *Electrochemical Impedance Spectroscopy and its Applications*. Springer, 2014.

[88] A. El Mejdoubi, A. Oukaour, H. Chaoui, Y. Slamani, J. Sabor, and H. Gualous, "Online Supercapacitor Diagnosis for Electric Vehicle Applications," *IEEE Trans. Veh. Technol.*, vol. 65, no. 6, pp. 4241–4252, Jun. 2016, doi: 10.1109/TVT.2015.2454520.

[89] A. El Mejdoubi, H. Chaoui, H. Gualous, and J. Sabor, "Online Parameter Identification for Supercapacitor State-of-Health Diagnosis for Vehicular Applications," *IEEE Trans. Power Electron.*, vol. 32, no. 12, pp. 9355–9363, Dec. 2017, doi: 10.1109/TPEL.2017.2655578.

[90] B. Yang *et al.*, "Applications of battery/supercapacitor hybrid energy storage systems for electric vehicles using perturbation observer based robust control," *Journal of Power Sources*, vol. 448, p. 227444, Feb. 2020, doi: 10.1016/j.jpowsour.2019.227444.

[91] F. Altaf, "On modeling and optimal control of modular batteries: thermal and state-of-charge balancing," PhD thesis, Chalmers University of Technology, Göteborg, Sweden, 2016.

[92] L. Solero, A. Lidozzi, and J. A. Pomilio, "Design of Multiple-Input Power Converter for Hybrid Vehicles," *IEEE Transactions on Power Electronics*, vol. 20, no. 5, pp. 1007–1016, Sep. 2005, doi: 10.1109/TPEL.2005.854020.

[93] S. Shili, "Contrôle des circuits d'équilibrage des systèmes de stockage d'énergie (supercondensateurs) en vue d'estimer et d'améliorer leur durée de vie," PhD thesis, Université Claude Bernard Lyon 1, Université de Lyon, Villeurbanne, France, 2016.

[94] S. J. Moura, "Techniques for battery health conscious power management via electrochemical modeling and optimal control," PhD dissertation, The University of Michigan, Ann Arbor, MI, USA, 2011.

[95] M. H. Rashid, Ed., *Power electronics handbook: devices, circuits, and applications handbook*, 3rd ed. Burlington, MA, USA: Elsevier, 2011.

[96] G. Karmiris and T. Tengnér, "PEAK SHAVING CONTROL METHOD FOR ENERGY STORAGE."

[97] "The Enhanced Frequency Control Capability (EFCC) project closing down report," National Grid ESO, Apr. 2019. [Online]. Available: https://www.nationalgrideso.com/document/144566/download

[98] "Historic frequency data | National Grid ESO." https://www.nationalgrideso.com/industry-information/balancing-services/frequency-response-services/historic-frequency-data (accessed Mar. 27, 2022).

Appendix A: Modeling the DC-DC Power Converter

A.1 State-Space Averaged Model

As discussed in Subsection 2.2.3, the state-space averaged model in (2.3)–(2.5) for a nonisolated bidirectional DC-DC power converter in a half-bridge architecture connected to a supercapacitor (as shown in Fig. A.1(a)) was obtained by considering the individual states of the converter. For easy reference, the model is reproduced below. With an initial conditions vector $\mathbf{x}_0$, the converter state-space averaged model for $t \geq t_0$ is given by:

$$\begin{aligned} \dot{\mathbf{x}} &= \mathbf{A}\mathbf{x} + \mathbf{B}\mathbf{u} \\ \mathbf{y} &= \mathbf{C}\mathbf{x} + \mathbf{E}\mathbf{u} \end{aligned} \tag{A.1}$$

where

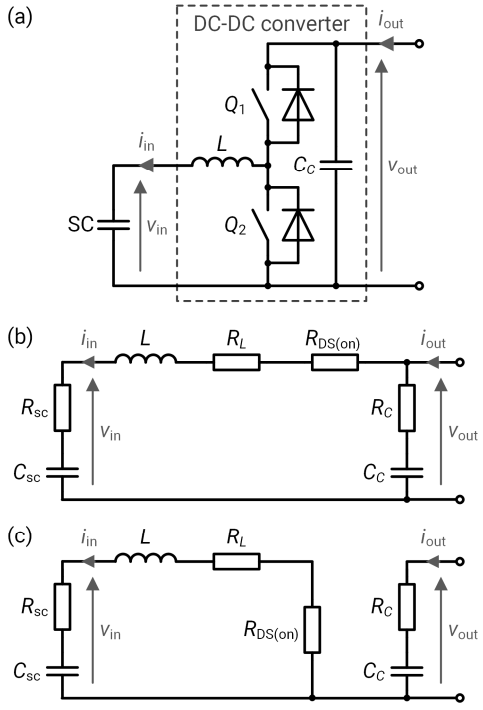

Fig. A.1. (a) A nonisolated bidirectional DC-DC power converter ($v_{out} \geq v_{in}$) in a half-bridge architecture; (b) The converter's first state ($Q_1 = 1$ and $Q_2 = 0$), which is on during the first Dt_s interval within the switching period t_s ; and (c) The second state ($Q_1 = 0$ and $Q_2 = 1$), which is on for the remaining $(1 - D)t_s$ interval

$$\mathbf{x} = \begin{bmatrix} i_{\text{in}} \\ v_{Cc} \end{bmatrix}, \quad \dot{\mathbf{x}} = \begin{bmatrix} \frac{\mathrm{d}i_{\text{in}}}{\mathrm{d}t} \\ \frac{\mathrm{d}v_{Cc}}{\mathrm{d}t} \end{bmatrix}$$
$$\mathbf{y} = \begin{bmatrix} i_{\text{in}} \\ v_{\text{in}} \\ v_{\text{out}} \end{bmatrix}, \quad \mathbf{u} = \begin{bmatrix} v_{C\text{sc}} \\ i_{\text{out}} \end{bmatrix} \tag{A.2}$$

and

$$\mathbf{A} = \begin{bmatrix} -\frac{R_{\text{sc}} + R_L + R_{\text{DS(on)}} + R_C D}{L} & \frac{D}{L} \\ -\frac{D}{C_C} & 0 \end{bmatrix}$$
$$\mathbf{B} = \begin{bmatrix} -\frac{1}{L} & \frac{R_C D}{L} \\ 0 & \frac{1}{C_C} \end{bmatrix}$$
$$\mathbf{C} = \begin{bmatrix} 1 & 0 \\ R_{\text{sc}} & 0 \\ R_C D & 1 \end{bmatrix} \tag{A.3}$$
$$\mathbf{E} = \begin{bmatrix} 0 & 0 \\ 1 & 0 \\ 0 & -R_C \end{bmatrix}$$

The vectors $\mathbf{x}$, $\dot{\mathbf{x}}$, $\mathbf{y}$, and $\mathbf{u}$ are the state, derivative of the state, output, and input vectors, respectively, and the matrices $\mathbf{A}$, $\mathbf{B}$, $\mathbf{C}$, and $\mathbf{E}$ are the system, input, output, and feedforward matrices, respectively. System and component parameter values relevant in the model are in Table 2.1.

The model as presented in (A.1)–(A.3) is the result of taking account of the synchronous or complementary control of switches Q_1 and Q_2 in Fig. A.1(a). This means that if one switch is on, the other is off. This switching behavior results in two converter states. A switching period t_s is thus divided into a period for the first state and the remaining period for the second state. If D is the duty ratio of the pulse-width modulated (PWM) signal controlling the converter, then the first state (say $Q_1 = 1$ and $Q_2 = 0$) is on for the first Dt_s interval and the second state ($Q_1 = 0$ and $Q_2 = 1$) is on for the remainder $(1 - D)t_s$ of the interval. These two states result in two distinct circuits resulting from the switching of the two switches.

The first state is shown in Fig. A.1(b) where the conduction losses of each component in the form of the equivalent series resistances (ESR) or parasitic resistances were considered. On the other hand, Fig. A.1(c) shows the circuit for the second state. The circuits for the two states can be solved for their own state-space model. For example, the first state circuit has its own model $\dot{\mathbf{x}} = \mathbf{A}_1\mathbf{x} + \mathbf{B}_1\mathbf{u}$ and $\mathbf{y} = \mathbf{C}_1\mathbf{x} + \mathbf{E}_1\mathbf{u}$. The same thing goes for the second state circuit where it is associated with its own

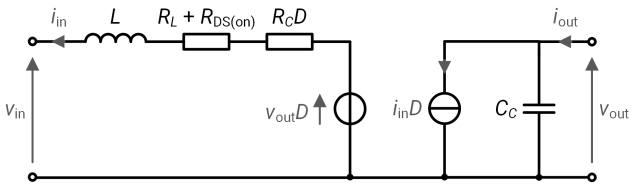

Fig. A.2. The power converter state-space averaged model in circuit diagram form

model $\dot{\mathbf{x}} = \mathbf{A}_2\mathbf{x} + \mathbf{B}_2\mathbf{u}$ and $\mathbf{y} = \mathbf{C}_2\mathbf{x} + \mathbf{E}_2\mathbf{u}$. The process of averaging entails that the two state-space models consider the time intervals associated with each state. This can be done for matrix **A**, for example, by taking $\mathbf{A} = \overline{\mathbf{A}} = D\mathbf{A}_1 + (1 - D)\mathbf{A}_2$. This step shows that, essentially, the first state takes the first interval of the switching period and the second state takes the second interval of the period. The same process was followed for matrices **B**, **C**, and **E**. The result of this averaging process are the matrix values shown in (A.3) and thus completing the state-space averaged model of the power converter. For the simulations of the converter required in the different parts of this thesis, the circuit form of the mathematical model was instead used. Fig. A.2 shows the circuit diagram based on the model in (A.1)–(A.3). It can be derived from the consideration of the first line of (A.1) and replacing the terms of the equations expanded from the matrix multiplications with the relevant circuit components.

Also discussed in Subsection 2.2.3 was the steady-state behavior of the power converter in the form of equations (2.9)–(2.11). In order to obtain the latter equations, it is important to recall that the state-space averaged model is a dynamic model. At steady state however, the state variables are unchanging. Thus, the derivative of the state vector must be a zero vector: $\dot{\mathbf{x}} = \mathbf{0}$. This means that the derivatives of the state variables, which are the elements of the vector, are unchanging or zero as well: $\frac{\mathrm{d}i_{\mathrm{in}}}{\mathrm{d}t} = 0$ and $\frac{\mathrm{d}v_{Cc}}{\mathrm{d}t} = 0$. From these conditions, we can derive the expressions in (2.9)–(2.11). Equation (2.9) is readily available from the steady-state form of the first row of the expanded equations from the matrix multiplications in (A.1). Meanwhile, (2.10) results from the algebraic manipulations of the second row and (2.11) readily follows from (2.10) when a lossless case is considered.

A.2 Small-Signal Model

We also showed in Subsection 2.2.3 the process of the derivation of the converter transfer functions. It starts with obtaining the small-signal model of the converter. It was explained that the **x**, $\dot{\mathbf{x}}$, **y**, and **u** needed to be perturbed such that the full variable has a nominal value and a small time-varying value. The nominal component represents a DC signal and the small time-varying component is a small AC signal perturbed about the DC value. For example, the derivative of the state vector becomes: $\dot{\mathbf{x}} = \dot{\mathbf{X}} + \dot{\hat{\mathbf{x}}}$. The term $\dot{\mathbf{X}}$ is the DC component and the other term $\dot{\hat{\mathbf{x}}}$ is the AC component. This whole process

has the aim of linearizing the otherwise nonlinear converter model. Since the duty ratio itself is perturbed, consideration of the small signals starts at the averaging step in the previous section, Section A.1. As an example, let us take the first line of (A.1). With $\mathbf{x} = \mathbf{X} + \hat{\mathbf{x}}$, $\dot{\mathbf{x}} = \dot{\mathbf{X}} + \dot{\hat{\mathbf{x}}}$, $\mathbf{y} = \mathbf{Y} + \hat{\mathbf{y}}$, $\mathbf{u} = \mathbf{U} + \hat{\mathbf{u}}$, and $d = D + \hat{d}$, the first line becomes: $\dot{\hat{\mathbf{x}}} = \left(\dot{\mathbf{X}} + \dot{\hat{\mathbf{x}}}\right) = \left[\mathbf{A}_1\left(D + \hat{d}\right) + \mathbf{A}_2\left(1 - D - \hat{d}\right)\right](\mathbf{X} + \hat{\mathbf{x}}) + \left[\mathbf{B}_1\left(D + \hat{d}\right) + \mathbf{B}_2\left(1 - D - \hat{d}\right)\right](\mathbf{U} + \hat{\mathbf{u}})$. Multiplications of small signals are ignored. In addition, it was assumed that the duty cycle perturbation is the only applied perturbation to the system. Simplification should then result in the first line of (2.6). Derivation of the second line of (2.6) follows a similar process.

Derivation of the transfer function vectors in (2.7) starts with the results in (2.6). Since the perturbed signals are AC in nature, it follows that they have a corresponding Laplace transform in the s domain. For example, the Laplace transformation of $\dot{\hat{\mathbf{x}}}$ is: $\mathscr{L}\{\dot{\hat{\mathbf{x}}}\} = s\hat{\mathbf{x}}(s)$, which follows the differentiation theorem given a zero initial condition. We can thus apply Laplace transformation to the first line of (2.6): $\mathscr{L}\{\dot{\hat{\mathbf{x}}}\} = \mathscr{L}\{[\mathbf{A}_1 D + \mathbf{A}_2(1 - D)]\hat{\mathbf{x}} + [\mathbf{B}_1 D + \mathbf{B}_2(1 - D)]\hat{\mathbf{u}} + [(\mathbf{A}_1 - \mathbf{A}_2)\mathbf{X} + (\mathbf{B}_1 - \mathbf{B}_2)\mathbf{U}]\hat{d}\}$. This results in: $s\hat{\mathbf{x}}(s) = \mathbf{A}\hat{\mathbf{x}}(s) + \mathbf{B}\hat{\mathbf{u}}(s) + [(\mathbf{A}_1 - \mathbf{A}_2)\mathbf{X} + (\mathbf{B}_1 - \mathbf{B}_2)\mathbf{U}]\hat{d}(s)$. From the latter we can easily derive the first line of (2.7) based on the assumption that $\hat{\mathbf{u}}(s) = \mathbf{0}$ using algebraic manipulation. We follow the same process for the second line of (2.7). The first transfer function in (2.8) is just the first element of the second line in (2.7). To obtain the second transfer function in (2.8), we just need to multiply the third element of the second line in (2.7) with the inverse of the first transfer function.